Title
Attosecond Transient Absorption of Solid-State and Phase-Change Materials

Author
Jager, Marieke Faye

Publication Date
2017

Peer reviewed|Thesis/dissertation

Attosecond Transient Absorption of Solid-State and Phase-Change Materials

By

Marieke Faye Jager

A dissertation submitted in partial satisfaction of the

requirements for the degree of

Doctor of Philosophy

in

Chemistry

in the

Graduate Division

of the

University of California, Berkeley

Committee in charge:

Professor Stephen R. Leone, Co-Chair
Professor Daniel M. Neumark, Co-Chair
Professor Eric Neuscamman
Professor David Attwood

Fall 2017

Attosecond Transient Absorption of Solid-State and Phase-Change Materials

by

Marieke Faye Jager

Abstract

Attosecond Transient Absorption of Solid-State and Phase-Change Materials

by

Marieke Faye Jager

Doctor of Philosophy in Chemistry

University of California, Berkeley

Professor Stephen R. Leone, Co-Chair

Professor Daniel M. Neumark, Co-Chair

Attosecond science, utilizing short bursts of extreme ultraviolet light, has opened up a fascinating new field of ultafast light-matter interactions, where dynamics in atomic, molecular, and solid state systems can now be followed on the timescale of electron motion. In this dissertation, applications of attosecond pulses toward performing transient absorption spectroscopy experiments on complex electron-correlation-driven processes in material systems are described. In the first chapter, a brief overview of ultrafast spectroscopy, attosecond pulse production, and light-matter interaction in the extreme ultraviolet is provided, which offers the necessary breadth and background for the detailed case study that follows, on the insulator-to-metal phase transition in vanadium dioxide.

The origin of the bandgap in vanadium dioxide, which is not predicted to exist under conventional single-particle band theories, has been explained as the result of either electron correlation or structural distortion. The goal of the experiments presented herein is to use transient absorption spectroscopy with attosecond pulses to characterize the timescale of this process and gain a mechanistic understanding of how it occurs. Because vanadium dioxide is heat sensitive, an apparatus had to be specifically tailored to this type of experiments, and it is described in the second chapter. The results and analysis, including extreme ultraviolet static and time-resolved measurements on both the insulating and metallic phases, are described in the third chapter.

The second half of this dissertation describes the design and construction of a new vacuum endstation to perform attosecond-pump attosecond-probe measurements, which was constructed and tested at Berkeley and installed at a high power attosecond beamline at the University of Central Florida. Ray tracing simulation and design considerations for the optical layout are described in the fourth chapter, and design of the vacuum endstation, diagnostics, and preliminary experiments and testing can be found in the fifth chapter.

To my family

Contents

List of Figures

List of Tables

Table of Acronyms

ATAS	Attosecond transient absorption spectroscopy
BS	Beam splitter
CEP	Carrier-envelope phase
CPA	Chirped pulse amplifier
FEL	Free electron laser
FOPA	Frequency domain optical parametric amplifier
FROG	Frequency resolved optical gating
FWHM	Full width at half-maximum
FXTAS	Few-femtosecond extreme ultraviolet transient absorption spectroscopy
GDOG	Generalized double optical gating
HHG	High harmonic generation
IMT	Insulator to metal phase transition
MCP	Microchannel plates
NIR	Near infrared
PM	Plane mirror
SI	Supporting information
SXR	Soft x-ray
TOF	Time-of-flight
UCF	University of Central Florida
XUV	Extreme ultraviolet

Acknowledgements

Any of the accomplishments I have achieved during my time at UC Berkeley would not have been possible without the many supportive and influential people in my life. First and foremost, I have to thank my advisors Stephen Leone and Daniel Neumark, without whom none of this would have been possible. Steve has been a strong source of guidance, and I greatly appreciate the opportunity to work on such a challenging project, as well as the confidence he always had that I would find a way to succeed. Dan has been a great source of direction and helped me break through many a roadblock. I appreciate the high standard he always maintained, and for pushing me to rise to meet it.

During my time in the Leone and Neumark groups I had the opportunity to work with some amazing colleagues. I am grateful to Andrey Gandman, my first mentor in the group, for being a patient teacher. Jim Prell has been both an incredible mentor and a wonderful friend to me, and he is a constant source of inspiration. In my time in the group I worked most closely with Christian Ott, and I am so grateful for his mentorship and friendship. I will always think of our time working together in the lab as my golden era of learning and experimental productivity. Lauren Borja helped me through many a tough time - we shared many of the same challenges, helping build a new project and instrument from the ground up, and I couldn't have done it without her friendship and solidarity. Erika Warrick and I went through our qualifying exams and GRCs together, and our lunch dates were a wonderful part of my graduate school experience. Martin Schultze, Desiré Whitmore, Andrew Attar, Chang-Ming Jiang, Natalie Gibson, and many others defined the early Leone group days for me, and I couldn't have asked for a more fun group to be a part of. To the current group members I wish every success. I am blown away by the talent of all that I have had a chance to work with, most closely Christopher Kaplan and Peter Kraus, who are doing amazing things.

Above all I am indebted to my family, who have loved and supported me not only through grad school, but every step of the way. My love of physics in a large part due to my dad – his contagious enthusiasm and excitement when talking about it helped spark my initial interest in the subject. My mom is the best role model I could have ever asked for, and the strongest woman I know. Her example and belief in me gave me the drive and determination to pursue all of the challenges that have led me here today. My twin brother Willem has been my best friend, and his support through everything and strong example have inspired me to be my best. And my older brother TJ has always encouraged me, and set an amazing example of not only being smart and hardworking, but also kind, and he is one of the best human beings I know.

Finally, to my boyfriend Robert, who for the last three years has supported me and encouraged me every day, I am so grateful. During the hardest times, when I felt like giving up, thank you for always helping me to see the light.

Chapter 1.

Introduction

1.1 Ultrafast and attosecond spectroscopy

In the physical sciences, the importance of understanding a process in real time cannot be understated. Chemical equilibrium is a dynamic balance of competing reactions, and even at absolute zero atoms and molecules retain kinetic energy, as a consequence of quantum mechanics. Dynamics are ubiquitous, and time-resolved spectroscopy, utilizing short bursts of light to take snapshots of a process in time, is a powerful tool to study them.

Early time-resolved experiments utilized fast optical shutters or rotating mirrors as in streak cameras, where the time resolution that can be achieved with such mechanical processes is generally limited to nanoseconds. Photoelectronic streak cameras brought the time resolution into the picosecond regime (*1*), however, it was only through the development of pulsed lasers that time resolution in the femtosecond and attosecond (1 fs = 10^{-15} s, 1 as = 10^{-18} s) regime has become possible. Femtosecond studies have allowed scientists to follow chemical reactions in real time, tracking the rearrangement of atoms within a molecule as they occur, and even allowing for the direct observation of transition states. This work, and the field of femtochemistry, was ushered in by Ahmed Zewail (and others), for which a Nobel Prize in Chemistry was awarded in 1999. Shortly thereafter, in 2001, the first sub-femtosecond pulses were produced (*2*, *3*). And while commercial laser systems producing such short pulses still do not exist, pulses as short as 53 as (*4*) have now been generated in tabletop laboratory settings and opened up the field of attosecond science.

Attosecond temporal resolution is of interest because it is the timescale on which electron dynamics occur. The motion of ions and chemical reactions occurs on the timescale of molecular vibrations, typically 10-100 fs, where the fastest molecular vibration occurs in diatomic hydrogen with a period of 8 fs, corresponding to the splitting between the υ=0 and υ=1 vibrational levels (*5*). However, as electrons are thousands of times lighter than nuclei, the timescales of electron motion can be significantly faster. The first Bohr orbit in hydrogen, for instance, has a period of 152 as. Thus the study of electronic processes and excitations inherently requires temporal resolution in the attosecond regime.

1.1.1 The Pump-Probe Technique

To access these temporal regimes and utilize short laser pulses, a controlled experimental technique is needed. In the simplest case, two pulses are used, where one intense pulse is used to initiate or kick-off the process of interest, and a second weaker pulse is used to probe the response of the system at variable time delays. The technique relies on an interferometer to introduce a time

delay between two different pulses, and the method is known as a pump-probe experiment. A variation where the transmission spectrum of the probe pulse it detected is illustrated in Figure 1.1, below. However, many variations are possible, where photoelectrons, ions, and reflected or scattered photons are just some of the signals that may be detected. In more complex experiments three or more pulses may be used.

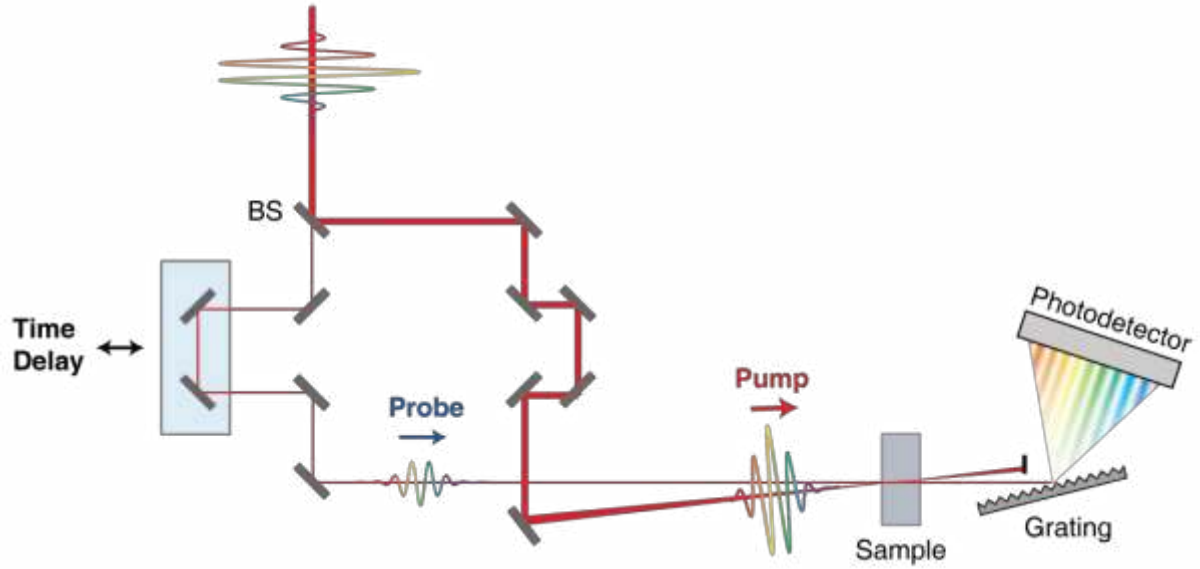

Figure 1.1. A pump-probe scheme utilizing a broad-spectrum white light pulse. A beam splitter (BS) is used to separate the beam into a pump and probe pulse, where a relative time delay is introduced by increasing the path length of one pulse with respect to the other. Both beams are then focused through the sample, the pump beam is blocked, and the probe beam transmission spectrum is resolved using a diffraction grating and photodetector.

A particular complication when working with short pulses, on the attosecond and few-femtosecond timescale, is that the pulses must focus through the sample nearly co-linearly. This is because if there is a relative angle between them, the two wavefronts will still cross at time delays longer than the pulse duration. The idea is schematically illustrated in Figure 1.2, where it is clear that in the non-co-linear case the two pulses are overlapped at all of the times shown, whereas in the co-linear case they overlap for only one frame. Typically how significant this effect is depends on the relative angle and also the size of the probe pulse. In most pump-probe experiments the pump beam focal volume is significantly larger than that of the probe, such that the probe sees a constant intensity rather than sampling over all of e.g. a Gaussian beam profile. If this condition is met it can be shown trigonomically that, in the limit of infinitely short pulses, the wavefronts are overlapped for a time $t_{overlap} = (\omega/c)\tan(\theta)$, where ω is the focal diameter of the probe beam and θ is the relative angle between the beams. For example, for a ω = 100 µm probe beam with a five degree relative incidence angle to the pump beam, the beams will overlap for a time $t_{overlap}$ = 29 fs, which is certainly unacceptable if few-femtosecond resolution is desired.

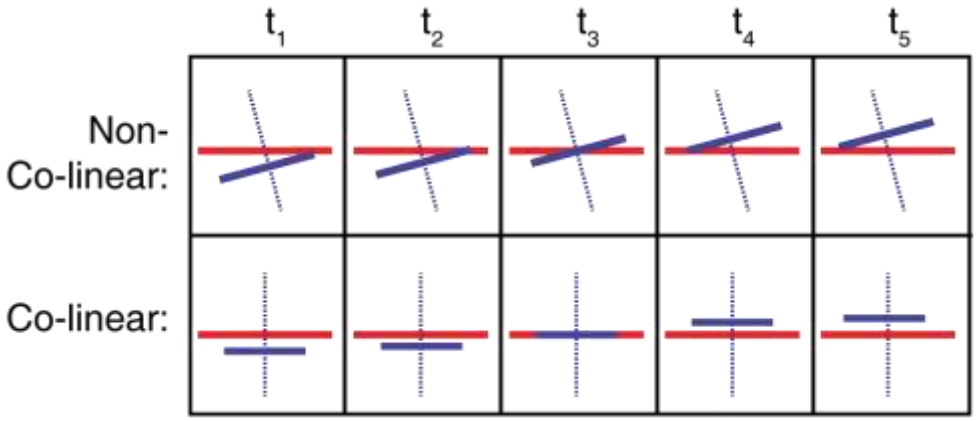

Figure 1.2. Comparison of the wavefronts at the focus at different time delays for a co-linear and non-co-linear geometry. The red line corresponds to the wave front of the pump pulse and the blue line to the wave front of the probe pulse. The dotted line is direction of propagation.

Thus for experiments seeking few-femtosecond temporal resolution or below, the angles must be either kept very shallow, and the beams can be separated in the far field, or the beams can propagate co-linearly and be distinguished based on having e.g. a different frequency or polarization. This energetic separation actually works quite well for attosecond experiments. Attosecond pulses are inherently generated in the extreme ultraviolet (XUV) or soft x-ray regions of the electromagnetic spectrum, and they are often not strong enough to serve as pump pulses[1]. Thus they are most often combined with few-femtosecond near-infrared (NIR), visible, or ultraviolet pump pulses.

1.1.2 High harmonic generation

Attosecond pulses are naturally produced via the process of high harmonic generation (HHG), which can be understood via a simple classical three step model (*6*, *7*). The process is induced via a strong-field, typically NIR laser pulse, which is focused to high intensity in a gas phase target. The gaseous atoms are then (1) tunnel ionized near the peaks of the electric field. The free electron is then (2) accelerated in the laser field, initially away from the atom in the first half cycle, and in the reverse direction on the next half cycle. And finally, under certain conditions the free electron then (3) collides with and is recombined with its parent atom, releasing a burst of energy equal to the ionization energy of the target gas plus the kinetic energy the electron gained in the field. An illustration of the process is provided in Figure 1.3.The kinetic energy gained in the laser field can be calculated as a function of the ionization time, and a maximum is found that corresponds to the cutoff energy of the high harmonic spectrum, given in Equation 1.1.

$$E_{cutoff} = I_P + 3.17U_P, \qquad \text{Equation 1.1}$$

Here I_P is the ionization potential of the gas target and U_P is the ponderomotive energy or "quiver" energy of the electron in the field, given by Equation 1.2,

[1] Work that attempts to achieve attosecond pump pulses for attosecond-pump attosecond-probe experiments will be described in Chapters 4 and 5.

$$U_P = \frac{e^2 E_0^2}{4 m_e \omega_0^2}, \qquad \text{Equation 1.2}$$

Here e is the electron charge, E_0 is the electric field amplitude, m_e is the electron mass, and ω_0 is the frequency of the incident radiation (*8*).

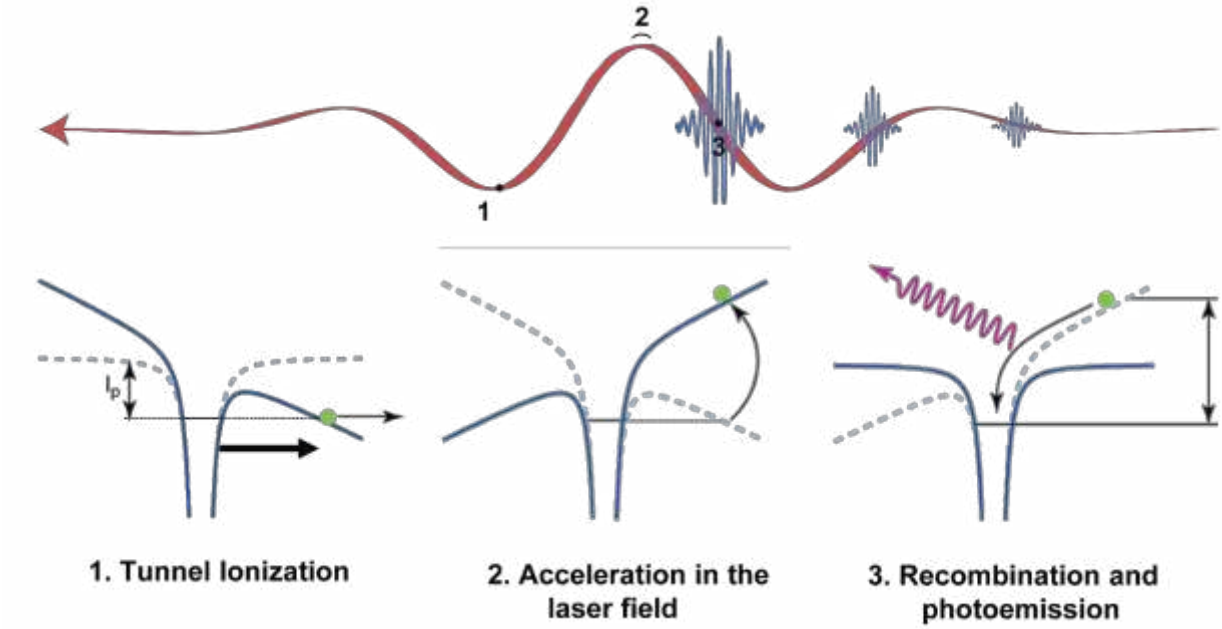

Figure 1.3. Schematic illustration of the three step model of high harmonic generation. The incident laser field is shown at the top in red, and the steps in the process occurring at positions 1, 2, and 3 are illustrated in the lower portion. The blue lines illustrate the nuclear potential and how it is distorted in the strong laser field.

Because tunnel ionization can only occur near the peaks of the electric field, the bursts of XUV radiation are emitted periodically every half cycle of the driving laser electric field, forming a train of attosecond pulses. If phase matching conditions are met, meaning that the driving laser and emitted XUV radiation travel at the same velocity in the medium, the emission of many atoms adds coherently for each pulse, resulting in brighter and temporally shorter pulse durations. While each single burst of XUV radiation would ordinarily have a continuous spectrum, the periodicity in time results in interference in the frequency domain. Constructive interference of the odd harmonics (of the fundamental driving frequency) and destructive interference of the even harmonics occurs, and thus only the odd harmonics will be observed in a typical high harmonic spectrum. The conversion efficiency of the HHG process is typically quite low, on the order of 10^{-6} to 10^{-5} (*9*).

1.1.3 Isolating Attosecond Pulses: Gating Techniques

For many experiments, working with a train of attosecond pulses can be sufficient to study the dynamics of interest. However to achieve the best possible temporal resolution and continuous

coverage of the XUV spectrum it is sometimes desirable to isolate a single attosecond pulse from the pulse train. The simplest way to reduce the number of pulses in an attosecond pulse train is to shorten the duration of the driving laser field. Bringing the NIR pulse duration to the few-cycle limit requires a very broad spectrum and careful dispersion compensation, but it can certainly be done. In addition, the following gating techniques can further cut down the number of pulses.

Amplitude gating, one of the simplest and earliest gating techniques, works by spectrally filtering the high harmonic spectrum such that only the highest photon energies (which came from the highest amplitude electric field cycle) are selected (*10*). This of course relies on short pulses to achieve good contrast, and the resulting bandwidth will be limited to the region just before the HHG cutoff energy. Alternatively, in ionization gating, the driving pulse is focused to such high intensity in the target medium that a large fraction of the gas is ionized on the leading edge of the pulse. This changes the dispersion relationship between the NIR and XUV radiation and results in a phase mismatch for any subsequent ionization events, suppressing the HHG process (*11*).

When the pulses are not short enough to achieve the contrast needed for amplitude or ionization gating, polarization gating is a versatile technique. In this scheme, two orthogonal polarization components of the generation pulse are produced and delayed with respect to each other using a quartz plate and a quarter waveplate to introduce circular polarization to each component: one right- and one left-circularly polarized. Where the two counter-rotating circularly polarized pulses overlap, a short linear polarization gate is formed, where the HHG process occurs. This relies on careful calculation of the required thickness of each optic, and it significantly reduces the conversion efficiency, but it can be very effective (*12–14*). In two-color gating, a small amount of the second harmonic of the generation beam is introduced such that the symmetry of the field is broken and attosecond pulses are only generated every cycle, as opposed to every half-cycle (*15*). When combined with polarization gating, this technique is known as double optical gating (*16*). A more recently invented technique, known as the attosecond lighthouse, uses a rotated wavefront in the generation beam such that each subsequent attosecond pulse propagates at a slightly different angle, allowing for spatial separation (*17*, *18*).

1.1.4 Applications of attosecond pulses and pulse trains

The flagship goal of attosecond science is to be able to observe and learn more about electron dynamics in real time. Several important experiments in this regard have been performed with both isolated attosecond pulses and attosecond pulse trains, in atomic and molecular systems, and more recently in the solid state. Many experiments utilize the NIR pulse as the pump pulse and the XUV pulse as the probe. For instance, in one key experiment it was revealed that strong-field ionization of krypton atoms results in a coherent superposition of electronic states, and a valence electron wavepacket could be observed as a 6.2 fs quantum beating in the XUV absorption spectrum (*19*). A similar NIR-pump XUV-probe transient absorption scheme in silicon revealed a tunneling excitation mechanism for population transfer that was synchronized to the electric field cycles of the driving pulse (*20*)

Other schemes exist where the XUV pulse performs the initial excitation and the NIR pulse perturbs it, for instance in attosecond photoelectron momentum streaking, where a photoelectron

replica of the XUV pulse is produced via ionization, and additional momentum is imparted via the strong-field NIR pulse. Using this technique, interesting phenomena such as time delays in photoemission from core orbitals have been observed (*21*). High harmonic spectroscopy, on the other hand, extracts information on attosecond dynamics by analyzing the spectrum of the HHG process itself under different molecular alignment and generation conditions. This method has also allowed for precise measurements of ionization time delays (*22*), as well as tomographic imaging of molecular orbitals (*23*). Multi-pulse four-wave mixing schemes are now also beginning to be explored (*24*, *25*), and sophisticated coincidence detection methods (*26*) enable even richer information to be drawn from attosecond measurements. This dissertation will focus specifically on NIR-pump XUV-probe transient absorption experiments of solid-state materials, and it will describe outlook and groundwork toward future work on XUV-pump XUV-probe attosecond measurements.

1.2 Core-level Spectroscopy and Electron Correlation in Solids

To use attosecond pulses as a probe of electron dynamics, it is critical to understand how XUV radiation interacts with matter, and how this might differ for solid-state systems. In general, XUV pulses have high enough photon energy that transitions from core-orbitals become possible, where an electron may be excited from a localized and deeply-bound core level to a more extended valence state, a process that competes and interferes with ionization directly from the valence states to the continuum. This section will provide a brief overview of the electronic structure and core level spectroscopy of solids, followed by relevant ultrafast phenomena in materials.

1.2.1 Electronic structure of solids

A solid-state system differs from atoms and molecules in that the valence energy levels become so closely spaced as to become continua, or bands. This can be simply understood from a chemist's perspective as an extension of molecular orbital theory. Assuming a linear combination of atomic orbitals, the width of a band corresponds approximately to the energy difference between having all atomic orbitals in phase and out of phase, and the number of states in the band is equal to the number of contributing orbitals (*27*). In the case of a crystalline solid, this is more rigorously described mathematically by solving the Schrödinger equation for a periodic potential, according to Equation 1.3,

$$\left[-\frac{\hbar^2}{2m_e}\nabla^2 + U(\vec{r})\right]\psi(\vec{r}) = E\,\psi(\vec{r}), \qquad \text{Equation 1.3}$$

where $U(\vec{r}) = U(\vec{R}+\vec{r})$ describes a system that is periodic with lattice vector $\vec{R}$. It was shown by Felix Bloch in 1928 that electronic wavefunctions of such a system can be described in a basis of what are now known as Bloch waves, having the form $\psi_{\vec{k}}(\vec{r}) = u_{\vec{k}}(\vec{r})\,e^{i\vec{k}\cdot\vec{r}}$. Here the function $u(\vec{r})$ must have the same periodicity as the crystal, and the parameter $\vec{k}$ describes the lattice wave vector (*28*). The allowed states are equally spaced in $\vec{k}$ between 0 and $\vec{K} = 2\pi/\vec{R}$ (the Brillouin zone boundary) with a spacing of $2\pi/L$, where L is the length of the crystal in $\vec{r}$. The energy spacing between adjacent $\vec{k}$ states is typically << k_BT, and the filling of states can be

described by a Fermi-Dirac distribution, where the center of the distribution is known as the Fermi energy (*29*).

Depending on the system, the resulting electronic structure can fall into several different categories, where the Schrodinger equation is typically solved using different approximations in each case, e.g. tight-binding, nearly free electrons, etc. (*29*). A crystal with a partially filled band results in metallic behavior, and this band is known as the conduction band. If on the other hand, there is an energy gap (*band gap*) between a fully filled band and unfilled band, the system is characterized as a semiconductor or an insulator, depending on the size of the gap. The highest energy fully-filled band is known as the valence band and is akin to a highest occupied molecular orbital. The next-highest energy fully-unoccupied band is known as the conduction band, and is akin to the lowest unoccupied molecular orbital. The electronic structure of each of the described cases is illustrated in Figure 1.4, below.

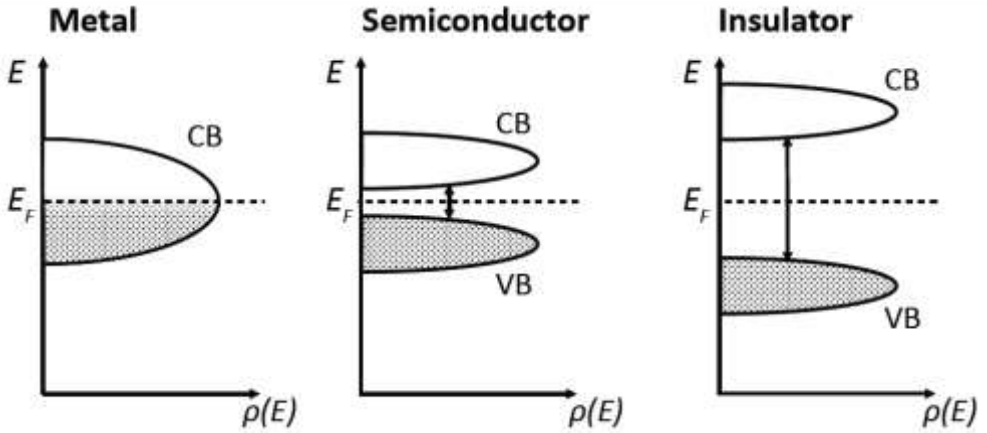

Figure 1.4. Electronic structure of solids. CB = conduction band, VB = valence band, E = energy, $\rho(E)$ = density of states. A system with a band gap greater than ~1 eV is generally characterized as an insulator (*29*).

1.2.2 Core-level transitions in solids: X-Ray Absorption

The quantum mechanical transition probability from a discrete state into a continuum of states is described by Fermi's Golden Rule, which is well-suited to the case of a core-level to conduction band type excitation. The formula, given in Equation 1.4, is derived from perturbation theory, and states that the transition probability from the initial state to final state, $\Gamma_{i\to f}$, is equal the transition matrix element of the perturbation V' multiplied by the density of states at the transition energy, $\rho(E_{i\to f})$. The dipole approximation can typically be used to simplify the perturbation operator, and dipole selection rules between the initial and final states can be applied.

$$\Gamma_{i\to f} = \frac{2\pi}{\hbar}\left|\langle\psi_i|V'|\psi_f\rangle\right|^2\rho(E_{i\to f}), \qquad \text{Equation 1.4}$$

If only a single electron is active in the transition, a core-state and empty-state wave function, ξ and *c,* can be substituted for ψ_i and ψ_f, respectively. The transition probability can then be approximated to $\Gamma_{i\to f} \propto M^2\rho$, where the matrix element, $M = |\langle c|V'|\xi\rangle|$, frequently does not vary

much as function of energy. Thus, in this approximation, the absorption spectrum reflects the symmetry projected density of empty states. For systems where overlap between the core-level and valence orbitals is small, this is often a decent approximation. However, when dealing with more localized valence states, such as the 3d orbitals in transition metal oxides, the overlap between e.g. a 2p or 3d core orbital and the valence states can be quite significant, and the final state multi-electron wave function as well as the density of states in the presence of the core-hole are significantly perturbed. In this case, the absorption spectrum cannot be directly related to the density of unoccupied states, and the result is dominated by atomic multiplet effects such as the energetic reordering of different d-electron configurations in the presence of the core-hole (*30*).

The core-holes created by this process have lifetimes on the order of one femtosecond, which results in additional lifetime broadening imparted on the transition energies in the spectrum in the form of a Lorentzian lineshape. There are two different mechanisms through which the core-hole can decay. In fluorescence a higher lying electron drops down to fill the core-hole, and the energy difference is emitted in the form of radiation. In Auger decay, on the other hand, when an electron drops down to fill the core vacancy its energy is transferred to another electron, which is ejected (*30*). In the Auger case, the final state is the same as if the electron ejected had been directly ionized with the same photon energy. Coupling between these states in the continuum can result in an asymmetric Fano-type character to the lineshape (*31*, *32*).

1.3 Ultrafast processes in semiconductors and strongly correlated materials

Once the basic XUV absorption process in solids is understood, attosecond pulses can be applied to study a variety of processes that occur on the ultrafast timescale. This section will briefly describe some of the basic processes that occur following photoexcitation in a solid and their characteristic timescales. The experimental work in the subsequent chapters of this dissertation will focus specifically on one example that can occur in strongly correlated solids: an ultrafast insulator-to-metal phase transition. Thus some more specific background on this process will also be provided.

1.3.1 General ultrafast processes in semiconductors

Following the absorption process, which occurs on sub-femtosecond timescales, a complex sequence of events is initiated. Electron screening and correlation effects will occur with a timescale that depends on the materials plasma frequency, a function of the excited carrier density (*33*). Highly excited electrons in the conduction band can lose energy by exciting a new electron-hole pair, a process known as impact ionization, which occurs on few-femtosecond timescales and increases the number of free carriers. Carrier-carrier scattering occurs on similar timescales, and is the first step in the carrier thermalization process, followed by carrier-phonon scattering, which transfers energy to the lattice. Carrier-phonon scattering occurs with a timescale of tens-to-hundreds of femtoseconds for optical phonons and picoseconds and beyond for acoustic phonons. Coherent phonons with timescales on this same order of magnitude may also be initiated, depending on the excitation conditions and the system. And on longer timescales, tens of picoseconds and beyond, carrier recombination across the bandgap will occur via either Auger

recombination or fluorescence (*34*). The timescales of these processes are highlighted in Figure 1.5, below.

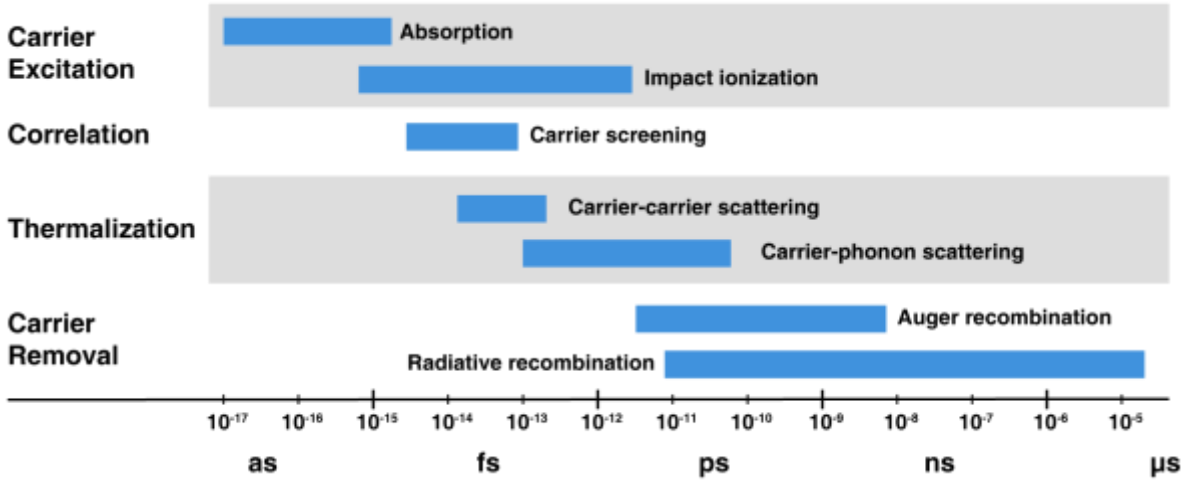

Figure 1.5. Comparative timescales of different ultrafast processes in semiconductors. The range of timescales for each process is approximate and not absolute. Adapted from reference (*34*).

1.3.2 Ultrafast processes in strongly correlated materials: the insulator-to-metal phase transition

An ultrafast process that is of particular interest for device applications is the insulator-to-metal phase transition (IMT), which has been observed in many transition metal oxide systems. The transitions can occur over a broad range of temperatures and result in a several order of magnitude change in resistivity (*35*, *36*). Vanadium dioxide, VO_2, is of particular device interest because the phase transition occurs at the convenient temperature of 340 K and the IMT has been measured to occur in less than 100 fs (*37–39*). It is of particular scientific interest because the driving force of the phase transition and the origin of the bandgap in the insulating state have not been definitively determined – two competing mechanisms have been debated, and a consensus has not yet been reached.

While there are many different IMT mechanisms that occur in different oxides, the discussion in this section will focus on the Peierls and Mott transitions, which are most relevant to VO_2. More background on the crystallographic and electronic structure and time-resolved work on VO_2 to date can be found in Chapter 3. Briefly, the controversy in VO_2 is related to whether the IMT is structurally driven or purely electronically driven, which has implications for how quickly the process can occur. Across the phase transition boundary, in addition to the dramatic changes in resistivity the crystallographic structure also changes, from a phase that has dimerized pairs of vanadium atoms in the insulating state to a phase that has equally spaced vanadium atoms in the metallic state. It is not yet clear whether the structural distortion is required for the IMT to take place (*39*, *40*).

In a Peierls interpretation, the bandgap originates from structural displacement. Peierl's theorem states that a one-dimensional chain of atoms, each contributing one electron, can achieve a lower energy state upon dimerization (*41*). When the atoms dimerize the unit cell is doubled, and the Brillouin zone is halved. A previously half-filled band, which would display metallic behavior, is split into a fully-occupied valence band and a fully-unoccupied conduction band, where a band gap is opened up between them. These can be described as the solid-state equivalent of a bonding and antibonding orbital. If the lower energy of the electrons in this configuration outweighs the elastic energy required for the distortion, then the dimerization will occur. This band structure change as a result of a Peierls transition is illustrated in Figure 1.6.

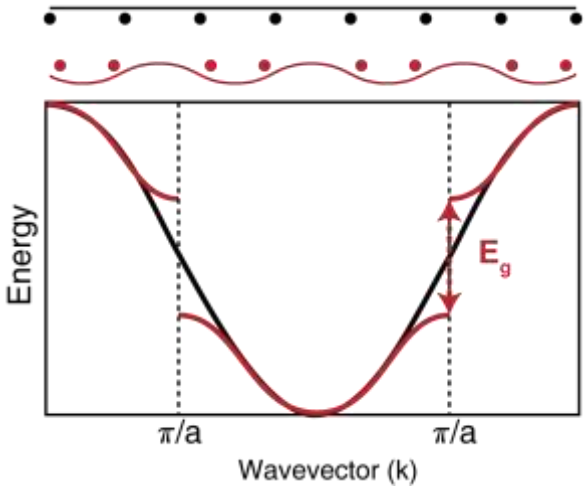

Figure 1.6. Band structure of a one dimensional chain of atoms equally spaced (black) and with dimerization (red). When each atom contributes one electron the dimerization can result in a lower energy state, with the opening of a band gap, E_g.

In a Mott system, on the other hand, the bandgap originates from electron correlation – electron-electron interactions that are not captured in a single-particle band structure calculation. This can be understood to play a significant role in systems where the valence electrons are relatively localized on their atomic sites, and the local Coulomb repulsion is strong. The Coulombic penalty of having more than one electron per atom (U) causes the doubly-occupied states to be higher in energy than the singly-occupied states[2]. Whether a Mott band gap is present depends on the magnitude of U and the bandwidth of the singly- and doubly-occupied bands. The bandwidth is determined by the degree of orbital overlap, and the resulting electron transfer or hopping integral (T). This competition between U and T is illustrated in Figure 1.7, below. A transition between the insulating and non-insulating states can be induced in a number of ways that involve either changing the bandwidth or local Coulomb repulsion. When induced thermally (or via radiation), the transition typically occurs as a result of screening.

[2] This effect is well described by the Hubbard model, and hence these bands are often referred to as the upper and lower Hubbard bands, respectively.

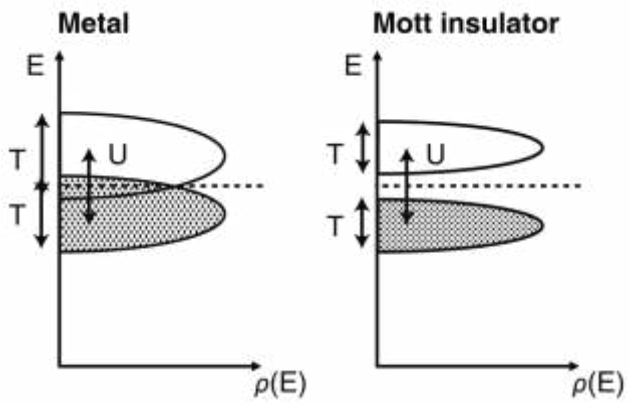

Figure 1.7. Competition between the bandwidth (proportional to the transfer integral, *T*) and the on-site Coulomb repulsion, *U*, which may result in a band gap and Mott insulator for cases where $U > T$.

The number of carriers that must be excited to induce the phase transition in this type of mechanism can be estimated using the Mott criterion (*36*), given by Equation 1.5.

$$a_H \left(\frac{N_e}{d}\right)^{\frac{1}{3}} \cong 0.2, \qquad \text{Equation 1.5}$$

Here a_H is the effective Bohr radius of the ion, N_e is the excited carrier density, and d is the degeneracy of the valence orbital. The effective Bohr radius is based on the effective mass of the carriers in the material of interest, which is typically given by $a_H = (\varepsilon\hbar^2)/(m^* e^2)$, where ε is the material's permittivity and m^* is the effective mass. Using the values for VO_2 of $\varepsilon = 100\varepsilon_0$ (*42*) and $m^* = 3m_e$ (*43*) yields an unrealistically high value of 1.84 x 10^{23} carriers per cm^3. It was later posited (*44*) that for Mott insulators, a coherence length should be used in place of the Bohr radius to account for the longer range interactions that result from electron correlation, given by $\xi = (2\hbar v_F)/\pi\Delta$. Here $v_F = (\hbar/m^*)(3\pi^2 N_e)^{1/3}$ is the Fermi velocity and $\Delta = k_B T_C$ is the thermal energy of the phase transition, where T_C is the critical temperature (29). This condition yields a much more reasonable value for VO_2 of N_e = 1.27 x 10^{20} carriers per cm^3, which corresponds to ~0.4% of vanadium atoms being excited.

The next chapter will describe the apparatus and methodology required to perform an XUV transient absorption experiment on VO_2 utilizing attosecond pulses. Because of the high absorption of XUV light in materials, samples must be on the order of a few tens of nanometers thick in order to measure transmission. This leads to challenges in heat dissipation that must be countered, which will be described, and a solution is presented. The third chapter discusses the results of the transient absorption measurements, and presents analysis of the IMT timescale and XUV absorption spectrum that give some insight into the Mott versus Peierls nature of the transition. The final two chapters present work toward building a new apparatus to perform attosecond-pump attosecond-probe experiments, in collaboration with the group of Zenghu Chang at the University of Central Florida. The fourth chapter describes ray tracing simulations and the optical path design. The fifth and final chapter covers the vacuum endstation design, diagnostics, and preliminary testing and experimental plans using this apparatus.

Chapter 2.

Experimental apparatus for attosecond transient absorption of solids

The content and figures of this chapter are reprinted or adapted with permission from M. F. Jager, C. Ott, C. J. Kaplan, P. M. Kraus, D. M. Neumark, and S. R. Leone.

"Attosecond transient absorption instrumentation for thin film materials: phase transitions, heat dissipation, signal stabilization, timing correction, and rapid sample rotation," Rev. Sci. Instrum., [Under Review], (2017).

2.1 Introduction to the Apparatus

In this work, an extreme ultraviolet (XUV) transient absorption apparatus was developed, tailored to attosecond and femtosecond measurements on solid-state thin-film samples, specifically for sample dynamics that are sensitive to heating effects. The setup combines methodology for stabilizing sub-femtosecond time-resolution measurements over 48-hours and techniques for mitigating heat buildup in temperature-dependent samples. Single-point beam stabilization in pump and probe arms and periodic time-zero reference measurements are described for accurate timing and stabilization. A hollow-shaft motor configuration for rapid sample rotation, raster scanning capability, and additional diagnostics are described for heat mitigation. Heat transfer simulations performed using a finite element analysis allow comparison of sample rotation and traditional raster scanning techniques for 100 Hz pulsed laser measurements on vanadium dioxide, a material that undergoes an insulator-to-metal transition at a modest temperature of 340 K. Experimental results are presented confirming that the vanadium dioxide (VO_2) sample cannot cool below its phase transition temperature between laser pulses without rapid rotation, in agreement with the simulations. The findings indicate the stringent conditions required to perform rigorous time-resolved absorption measurements on solid-state samples, particularly those with temperature sensitivity, and elucidate a clear methodology to perform them.

2.1.1 Purpose and Motivation

Many solid-state materials have properties that are strongly temperature dependent. In the most dramatic cases, solid-state phase transitions can result in sudden change of electronic, optical, or magnetic properties, which can be highly applicable for next-generation electronics (*45–47*). Colossal magneto-resistance (*48*), superconductivity (*49*), and insulator-to-metal phase transitions (*50*, *51*) are examples that have already been integrated into prototype photonic switches and other devices (*35*, *52*, *53*). As the engineering of these systems becomes more feasible, questions arise about the ultimate limits of such devices. Namely, it is important to understand how small they can be made and how quickly they can operate. To investigate the ultimate speed of these materials properties, pulsed laser experiments are performed in various pump-probe geometries. Data are

typically acquired by averaging over many laser pulses, where the measurement is repeated many times per second. However, heat buildup between laser pulses can be a significant impediment to measuring intrinsic material properties, especially if the material exhibits a phase transition driven by temperature. Heat mitigation problems are particularly enhanced under vacuum conditions where convective cooling is suppressed, which can be the case for example in experiments based on photoemission, soft x-ray, and extreme ultraviolet (XUV) measurements.

This work focuses on the emerging field of attosecond extreme ultraviolet measurements (*54*) and presents an apparatus for performing visible-pump XUV-probe transient absorption measurements on thin film solid-state samples, with emphasis on materials for which the response is strongly temperature dependent, such as those that exhibit thermally induced phase transitions. Pulsed XUV sources are produced in a tabletop setting via high-harmonic generation (*55*, *56*), a process that inherently creates attosecond pulse trains from which a single pulse can be isolated (*57*). In addition to the unprecedented time resolution enabled by such sources, the XUV absorption spectra of molecules and materials possess element and oxidation state specificity provided by the core-to-valence transitions probed. Measurements in the gas phase have provided new insights into fundamental processes, such as the behavior of electronic (*58*) and vibrational (*59*) wave packets, bond dissociation (*60*), and charge migration (*22*). However, some of the most technologically relevant ultrafast phenomena occur in the solid-state, where the application of time-resolved XUV measurements is relatively recent. Attosecond transient absorption spectroscopy (ATAS) is a powerful technique for such studies that provides a probe of the bulk response. In comparison with photoemission, ATAS has the strong advantage that the large bandwidth of the XUV pulses does not limit the energy resolution of the experiment. When transitioning ATAS from the gas phase to the bulk solid, new complications arise. In particular, due to the high attenuation of XUV light in materials, samples must generally be on the order of a few tens of nanometers thick, and for the same reason, materials need to be deposited on freestanding ultra-thin membrane substrates such as silicon nitride or diamond. The sample thickness and vacuum conditions required for XUV transmission mean that heat dissipation is poor and predominantly based on 2D transport. As the sample is not constantly refreshed, low damage thresholds and heat buildup mean that the repetition rate of the experiment must also be decreased, the sample has to be rapidly translated, or both of these steps must be taken.

An instrumental case study is presented for dealing with these complications in vanadium dioxide (VO_2), a technologically important material that exhibits a sub-100 fs insulator-to-metal phase transition (IMT) (*37–39*). When performing time-domain measurements on VO_2, it is imperative that the sample temperature cools back to a value below its IMT temperature (T_c) of 340 K (Ref. 6) between successive pump pulses. Experimentally it is shown that this condition is not met by raster scanning the sample, where the measured response is that of the higher temperature metallic phase. This is due to the relatively slow motion of even fast vacuum translation stages (typical speed few mm/s), compared to the typically millisecond inter-pulse time of 100 Hz to kHz repetition rate laser systems. While faster stages are available they generally have limited translation range and a high price point. In this work a custom sample mount consisting of a rapidly rotating hollow-shaft motor is introduced to provide more rapid sample movement through the laser beam focal volume. This introduces cooled sample sites to each pulse of the laser to overcome the heat dissipation problem. The rapidly rotating hollow-shaft motor design provides a qualitatively different XUV transient absorption response compared to raster scanning

measurements; the thermal heat load in the thin film sample can be dissipated, and the ultrafast response of the insulating phase and the phase transition are captured without artifacts. The detailed physics and timescales measured in VO_2 are described in reference (*61*) [Chapter 3], whereas this work focuses rather on the technical aspects. Heat transfer simulations are performed using a finite element method in COMSOL 5.2a, verifying that for the given experimental conditions, raster scanning at 1.6 mm/s translational speed is insufficient to counteract the accumulative buildup of heat between subsequent laser pulses, even at a reduced 100 Hz repetition rate of the experiment. Heating issues can be overcome, however, by implementing rapid sample rotation, effectively realizing >170 mm/s translational speed.

2.1.2 Experimental overview

The experimental apparatus designed for this work is illustrated in Figure 2.1. A carrier-envelope phase stable titanium-sapphire laser system (Femtolasers, 1.6 mJ, 1 kHz) is used to seed a neon-filled (2 bar static filling) hollow-core fiber with near-infrared (NIR) pulses, where self-phase modulation broadens the pulse spectrum from approximately 400 to 1000 nm. The pulses are temporally compressed using a chirped mirror compressor consisting of four mirror pairs (Ultrafast Innovations GmbH) and a pair of thin fused-silica glass wedges for finely tuned dispersion control. Pulses can be compressed to sub-5 fs in duration, as characterized via dispersion scan (*62*). The repetition rate is reduced to 100 Hz when required with an in-line optical chopper.

A majority (80%) of the pulse energy is used to generate high-order harmonics in the probe arm. For the VO_2 experiments described in this work, krypton was used as the harmonic generation medium at a backing pressure of ~30 Torr to produce attosecond pulses, optimized for maximum photon flux in the 40-50 eV region and yielding close-to-continuous harmonic spectra. Residual NIR light is filtered out using a 200 nm thick aluminum filter, and the remaining XUV light is focused through the sample using a toroidal mirror in a 1:2 geometry to achieve a spot size of approximately 70 μm full-width at half maximum (FWHM) at the sample. After transmission through the VO_2 sample, the XUV probe beam enters the spectrometer through a 200 μm pinhole and an additional 200 nm thick aluminum filter, and the XUV is spectrally dispersed with a gold coated flat-field variable-line-spacing reflection grating onto an XUV-sensitive CCD camera. The remaining 20% of the pulse energy is used for the pump arm to induce the insulator-to-metal transition, and this pulse undergoes a variable time-delay using a piezoelectric stage for fine delays and a motorized linear actuator stage for coarse delays. A broadband half-wave plate in combination with a wire-grid polarizer is used for the attenuation of the pump beam, which is focused and then recombined co-linearly with the probe beam on a 45° annular silver-coated mirror. The pump beam focuses through the sample to approximately 200 μm FWHM and is blocked with the aforementioned pinhole and aluminum filter combination. Measurements are performed in a pump-on pump-off scheme, using an optical shutter in the pump arm, to measure the spectrally resolved absorbance change (ΔOD) in the XUV as a function of time delay.

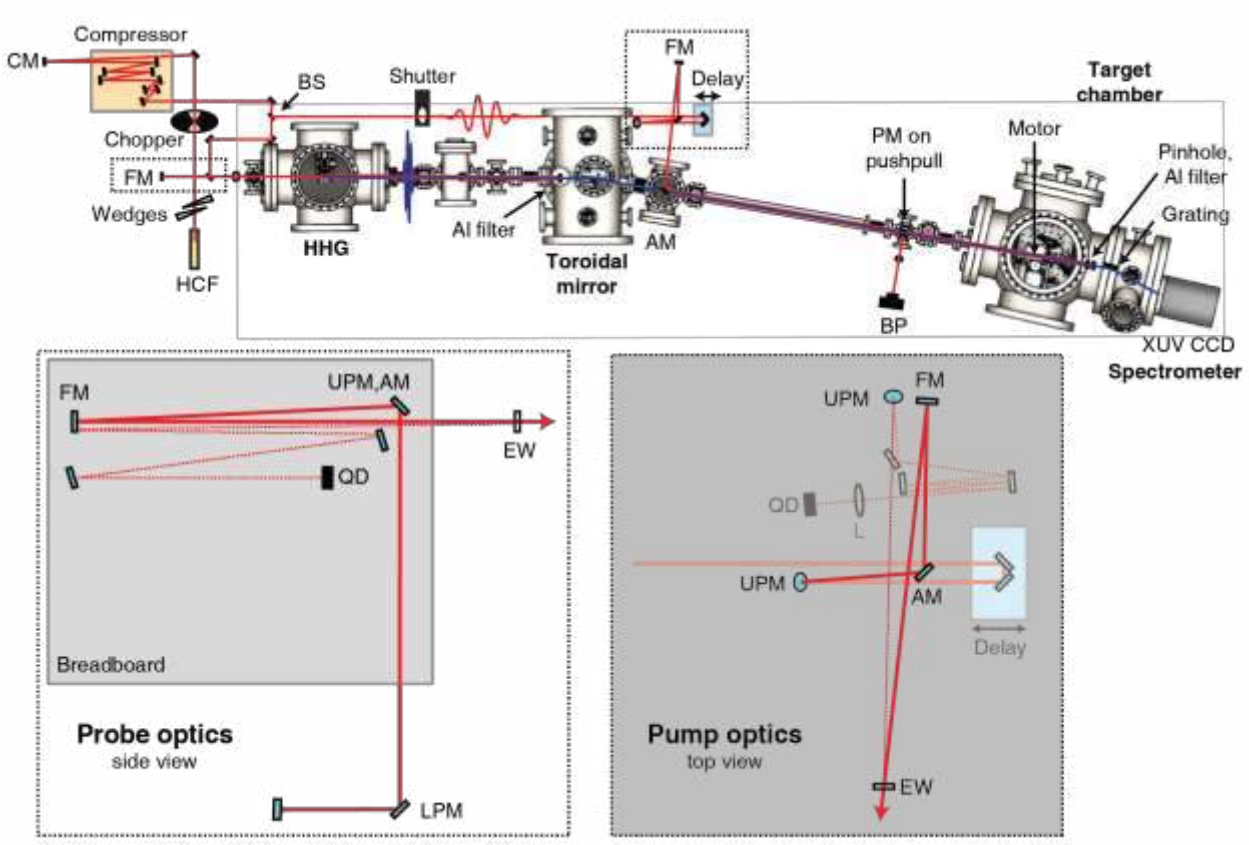

Figure 2.1. The beamline for solid-sate XUV transient absorption experiments. NIR light is shown in red, and XUV light in blue. HCF = hollow-core fiber, FM = focusing mirror, CM = collimating mirror, BS = beam splitter, AM = annular mirror, PM = pickoff mirror, and BP = beam profiler. Insets showing the probe and pump beam optics, including beam pointing stabilization, are shown. UPM = upper periscope mirror, LPM = lower periscope mirror, AM = actuated mirror, EW = entrance window, L = lens, and QD = quadrant diode. In the pump optics inset darker (lighter) colors denote beams and optics in the upper (lower) plane.

2.2 Custom Diagnostics and Capabilities Introduced

2.2.1 Optical Static Transmission Measurements

The target chamber is equipped to measure NIR transmission through the sample and characterize the foci of the pump and probe beams. The chamber geometry in the NIR measurement mode is illustrated in Figure 2.2a. A pickoff mirror on a motorized linear vacuum stage can be moved into the beam path, which sends the pump beam into a visible-NIR spectrometer or onto a power meter. The sample holder is mounted on motorized fast XY translation stages and can be moved to translate between multiple sample and reference slots. Losses along the beam path are calibrated such that absolute pump power at the sample focus can be measured. A pickoff mirror before entering the target chamber can be inserted (see Fig. 1) to send both the attenuated pump and HHG driver beam (aluminum filter removed) onto a beam profiler, with a distance matched precisely to

the position of the target sample. In combination with the measured pump beam power, this allows for the determination of absolute fluences, as well as setting and assuring spatial overlap of both beams.

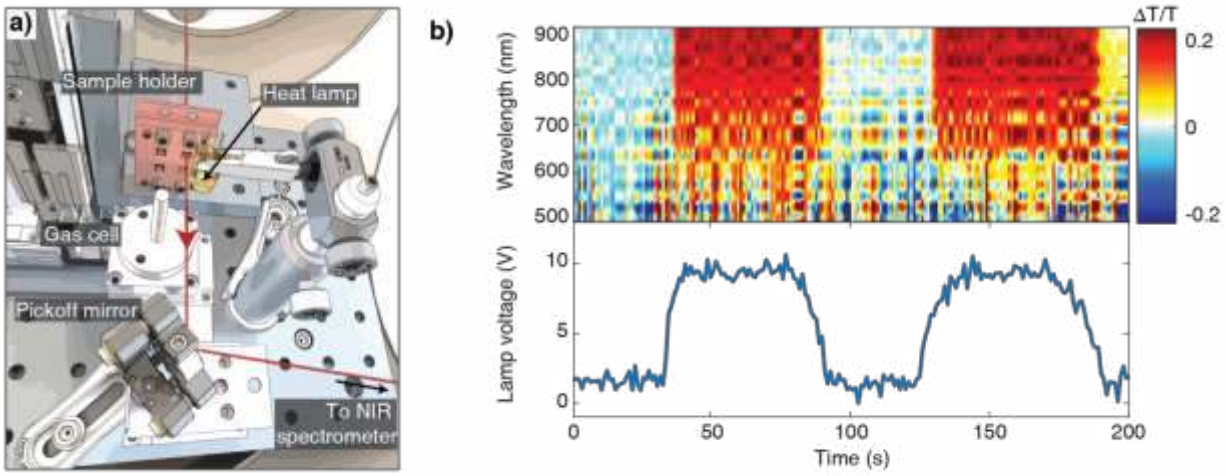

Figure 2.2. Target chamber configuration for NIR transmission measurements (**a**): the beam passes through a slot in the sample holder, and is sent out of the chamber by a pickoff mirror on a motorized stage. Four different positions (e.g. three samples and one reference) on the sample holder can be accessed using the XY stages. (**b**) Spectrally resolved NIR transmission measurement showing switching behavior of a VO_2 sample upon heating with a quartz heat lamp.

Additionally, a quartz halogen heat lamp (12 V, 10 W) is powered by a DC voltage supply and installed adjacent to the sample, at an approximately 1 cm distance, as shown in Figure 2.2. Heating the sample *in situ* is critical for characterizing heat sensitive samples. For phase transition materials, measuring the NIR transmission as a function of the lamp voltage provides a direct probe of the switching behavior, where a rapid increase or decrease in transmission can be observed when T_c is crossed. Thin film samples for absorption measurements are typically deposited on freestanding silicon nitride membranes, which are installed in the same sample holder as a reference. The thin film VO_2 samples are prepared at a thickness of 25 nm on 30 nm thick silicon nitride membranes by the method of pulsed laser deposition (*61*, *63*). Except as noted below, the underlying silicon nitride samples by themselves are not found to affect the static or transient spectra of these experiments. In the VO_2 experiments a 20% change in transmittance of these samples is observed when heating above 340 K, as shown in Figure 2.2b. The critical lamp flux required to induce the phase transition is also used to heat the sample *in situ* to measure the static XUV spectrum of the metallic phase as well as its transient response. Samples were also checked before and after time-resolved experiments to ensure that they still change phase and with the same magnitude.

2.2.2 XUV Static Absorption Measurements

With the heat lamp on or off, and retracting the NIR pickoff mirror, XUV static absorption spectra can be measured for both the insulating and metallic phases of VO_2, which can be found in

reference (*61*). In semiconductors, heating effects such as band-gap renormalization (*64*) can also be referenced. High quality static spectra are obtained by using the XY sample stages to alternate rapidly between sample and reference films at the full 1 kHz laser repetition rate, acquiring transmitted XUV spectra over 800 ms, and moving to a new position on the membrane surfaces thereafter. Sample thickness, homogeneity, local damage, and defects can be measured by plotting a transmission map of the integrated XUV signal as a function of the 2D position on the sample surface. Prolonged XUV exposure does lead to increased absorption over time in silicon nitride films, which creates a dark spot in the transmission map where the XUV light has been impinging. Taking optical spectra did not result in similar damage, so it is likely that ionizing radiation damage from the interaction with the XUV radiation is the source of this problem, possibly related to interaction with residual gas in the vacuum chamber environment. A full understanding of the damage mechanism is beyond the scope of this dissertation, however, based on its observation, samples are always raster scanned even when taking static XUV measurements, and in this way high quality and reproducible results are obtained.

2.2.3 Spatial and Temporal Stabilization for 48-Hour Measurements

The high attenuation of XUV light through solid-state samples and yet relatively smaller ΔOD signals compared to the gas phase, together with the decreased repetition rates that must be used, means that acquiring transient absorption spectrograms with sufficient signal-to-noise (i.e. requisite signal-to-noise level of 2-3 mΔOD for a typical 10-15 mΔOD transient absorption signal change) can take up to 48 hours. Since both long-term temporal and spatial drifts can be significant on these timescales, beam-pointing stabilization and time-delay correction are necessary.

Single-point beam pointing stabilization is used in both the pump and probe arms to compensate for spatial drifts. The beam pointing stabilization optics are shown in the insets of Figure 2.1. Active closed-loop control is implemented with an additional sample-and-hold circuit so that the beam positions do not drift between laser pulses for low-repetition-rate experiments, or when the pump beam is periodically blocked in pump-on / pump-off measurements. In the probe arm, the upper periscope mirror before the HHG focusing mirror is actuated. The beam is stabilized to the HHG focus using a back reflection from the chamber entrance window that is directed and focused onto a four-quadrant photodiode at a matched distance to the target. In the pump arm, the plane mirror before the focusing mirror is actuated and the back reflection from the entrance window is used to stabilize the beam to the sample focus, in the same manner. An output from the amplifier timing unit is used to trigger the beam-pointing stabilization system at repetition rates below 300 Hz, where a digital delay generator is used to shape the proper square-wave amplitude and duration for triggering.

Interferometric stabilization of the key points of the apparatus is a typical way to achieve timing stability, but active stabilization (*65*, *66*) by means of a co-propagating continuous wave blue laser could not be used in this case because of the challenges of the low repetition rate, the periodic blocking of the pump arm, and the possibility for residual blue light to be absorbed by and successive heating or damage occurring in the solid-state samples. Instead, periodic measurements are performed in neon gas, which has the advantage that (in addition to compensating for time-delay drifts over the course of the measurement) absolute time-zero can be measured and the pulse

can be characterized. Measurements in neon are performed between scans, approximately every eight minutes, by moving the solid state sample out of the beam path and inserting a gas cell into the focus using motorized stages (see Figure 2.2a for a design illustration of the target geometry). Using the gas cell, a transient absorption measurement can be performed in neon gas at a backing pressure of 100 Torr. The neon response allows an *in situ* determination of both time-zero and the instrument response function (*67*), which is then used to retroactively correct time-delay drifts and synchronize scans in the data analysis. A representative time delay drift trace is shown in Figure 2.3, where the experimental measurement is shown in panel A, zoomed in about the $2s^12p^64p$ line at 47.1 eV. A lineout is taken over the indicated region and fit to an error function, as shown in panel B, which can be done for each measurement to give the time delay drifts shown in panel C. The corrected scan has a variance corresponding to a timing uncertainty of 595 as. This uncertainty is not a fundamental limit, but depends on how frequently the time-zero measurements are performed and the time-delay sampling used (in this case 0.1 μm steps, which corresponds to 670 as delays). The instrument response function can be characterized by fitting the lineshape as a function of time delay, as in reference (*67*), and values on the order of 5-7 fs are typically obtained.

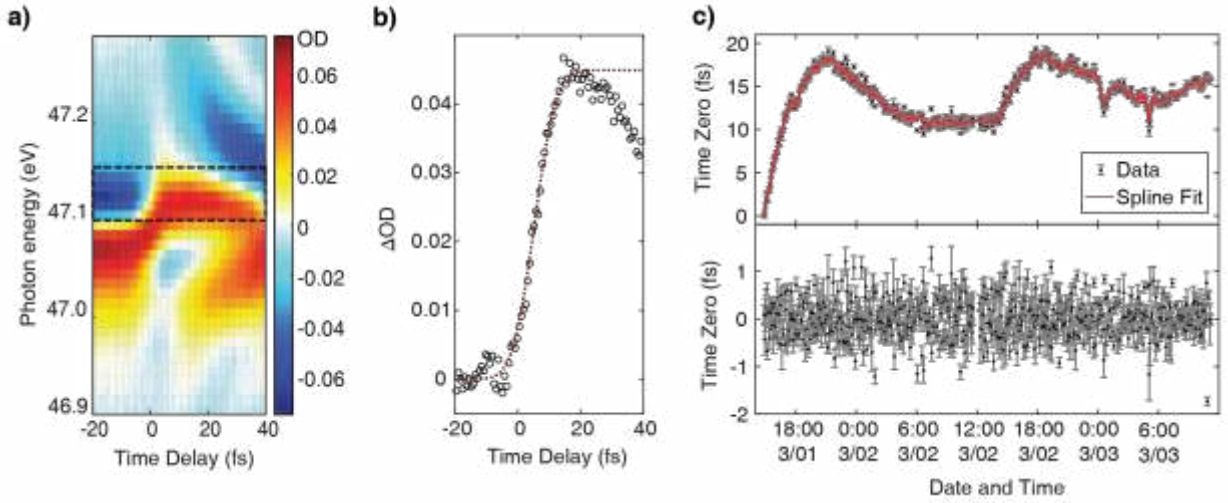

Figure 2.3. (**a**) A representative transient absorption measurement in neon about the $2s^12p^64p$ absorption line, showing a characteristic lineshape change. For time delay synchronization, a lineout is taken over the indicated region (black dashed box) as shown in panel (**b**). The initial rise is fit to an error function, the central position of which is used to quantify time delay drifts. (**c**) A representative time delay drift measurement over a 48 hour period, where the upper panel shows the drift in time-zero over the course of a measurement, and the lower panel shows the error in the time-zero determination following data correction, with a variance (corresponding to a timing jitter) of 595 as.

Faster dynamics can be observed for nonlinear processes that follow the electric field cycles of the pump pulse, as opposed to the intensity envelope. For example, if the conditions of the neon experiment are changed slightly, and residual NIR light from the HHG process is allowed to co-propagate with the attosecond beam, it alters the selection-rule-allowed transitions in neon and enables 2.6 fs quantum beats on the neon $2s^12p^63p$ line to be observed (*24*), as illustrated in Figure 2.4.

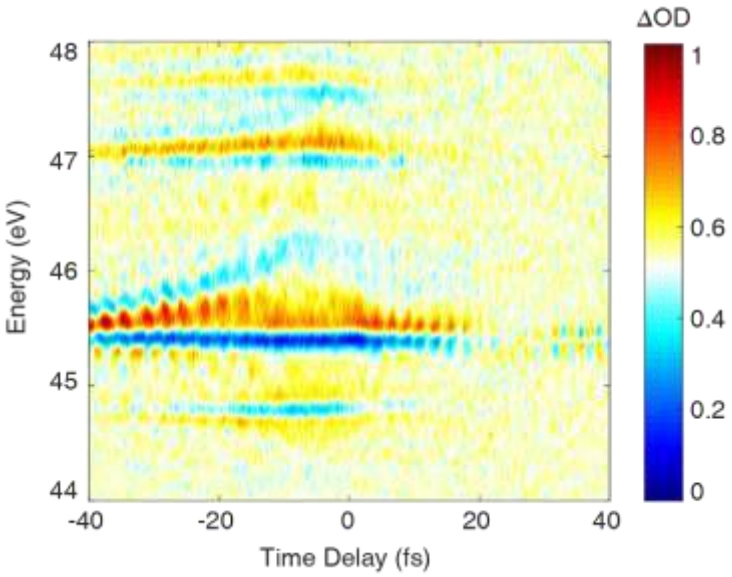

Figure 2.4. Transient absorption in neon in the vicinity of the $2s^1 2p^6 3p$ absorption line at 45.5 eV, demonstrating the ability to resolve dynamics shorter than the NIR pump pulse. Residual NIR light is allowed to co-propagate with the XUV pulse, allowing $2s^1 2p^6 3s$ and $2s^1 2p^6 3d$ excitations to take place, which can couple to the 3p final state via the NIR (pump) pulse.

2.2.4 Sample Raster Scanning and Rotation

Using the same sample holder as for static spectral measurements, NIR-pump XUV-probe transient absorption measurements can be performed. To mitigate heat buildup and sample damage, the XY stages are used to raster scan across the sample surface. However, as will be shown, this is not sufficient for particularly heat sensitive samples. The stages used (P.I. VT-80, high vacuum version) move at a maximum speed of 1.6 mm/s, or a maximum distance of 16 μm between each laser pulse when operating at 100 Hz, which is small compared to the 200 μm FWHM pump beam focal size, but is on the faster end of commercially available linear vacuum translation stages. The small sample sizes (typically few mm x few mm freestanding thin film apertures at most) make more rapid translation with linear stages nearly impossible, especially when considering acceleration/deceleration times. The experiment was programmed such that the stage moved over a 5 x 5 grid of positions across the sample surface, pausing at each location for pump off, shutter opening, and subsequent pump-on measurements. An exposure time of 1 s was used for the VO_2 experiments. Shorter exposures may lead to less heat buildup, but significantly reduces the duty cycle of the measurements and requires longer experimental run times. As will be shown below, in a scheme solely based on raster scanning, even when moving at maximum speed during each 1-s accumulation time, it is not feasible for the VO_2 sample to relax below T_C between each subsequent laser pulse. Thus a more sophisticated motion of the sample needs to be employed, since any further reduction of the repetition rate (e.g., 10 Hz requiring 480 hours of data acquisition time) is impractical.

With this in mind, an alternate sample holder was designed to make a measurement of the IMT dynamics possible, where samples are mounted centered on and normal to the axis of a vacuum-

compatible hollow-shaft motor (Koford Engineering), as illustrated in Figure 2.5. The motor is encased in an aluminum housing to dissipate heat and attaches to the XY translation stages. Rotation speeds up to 10,000 rpm or 167 Hz can be achieved. For the VO_2 experiments the stages were positioned such that the beams impinged at a radius of 0.75 mm from the central axis of the hollow shaft and the motor was operated at 37 Hz. This corresponds to a velocity of >170 mm/s, or slightly over one full rotation every three laser pulses when operating at 100 Hz, much greater than can be achieved with linear stages. The motor frequency is out of phase with the laser repetition rate such that the same areas on the sample are not irradiated repeatedly. Additionally, the motor housing was fabricated with a transmission hole to allow for measurements bypassing the sample. For example, measurements through a gas cell can be performed, as shown in Figure 2.5b, for the time zero reference measurements. A close-up of the sample mounting is shown in Figure 2.5c, where the long screws are used as handles for easily exchanging the sample without removing the entire housing from the chamber.

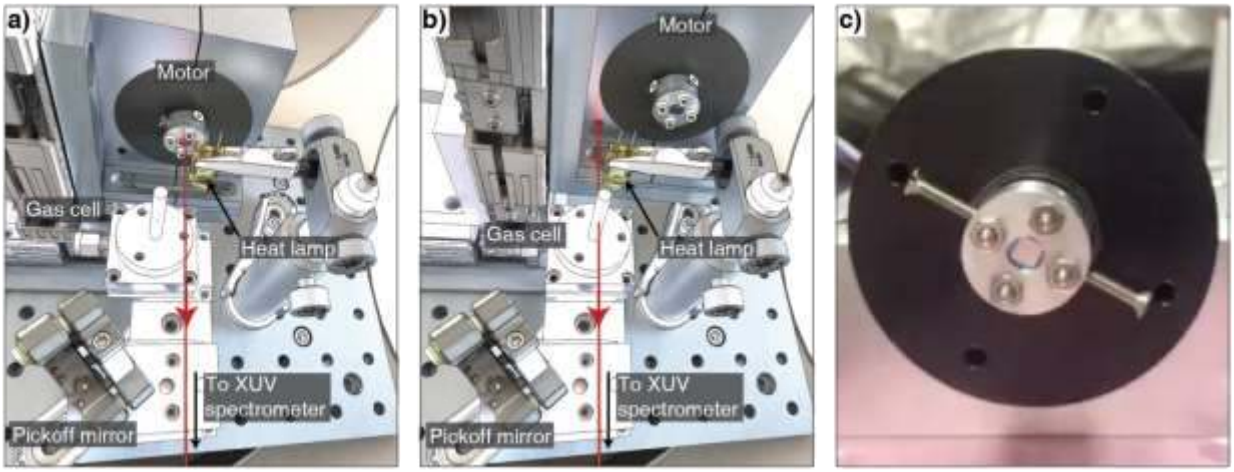

Figure 2.5. Target chamber setup for transient absorption measurements. (**a**) The beam transmits through the sample mounted on the hollow-shaft motor and goes straight to the XUV spectrometer. (**b**) The stages are moved such that the beam transmits through a hole in the motor housing and passes through the gas cell for time zero reference measurements. The cell can also be moved out of the beam path for optimizing the XUV harmonic flux. (**c**) A close up of the sample holder cap that is attached to the motor.

2.3 Heat Transfer in VO_2 Thin Films

2.3.1 Experimental Measurements

Transient NIR-pump XUV-probe absorption experiments were performed on VO_2 thin films at 100 Hz at a NIR pump fluence of 25 mJ/pulse, with a pump beam focal spot size of 200 µm FWHM. As noted, samples were 25 nm thin films of polycrystalline VO_2 (*68*) deposited on 30 nm freestanding silicon nitride membranes. The freestanding membrane area was 3 mm x 3 mm, and the membrane was supported on a silicon frame of 7.5 mm x 7.5 mm outer dimensions, 3 mm x 3 mm aperture, and 525 µm thickness. The experiment was performed with the hollow shaft motor installed, operating at a rotation speed of 37 Hz and with a radius of 0.75 mm between the beam

and motor axis. The experiment was performed first on the sample with no heating, and then with the heat lamp on to thermally induce the insulator-to-metal phase transition.

The resulting XUV transient absorption spectrograms (nominally 800 nm excitation with sufficient power density to induce the insulator to metal transition and XUV probing) with sample rotation are shown in Figure 2.6, depicting the qualitatively different behavior between the insulating phase (a) and the metallic phase (b) and providing evidence that the sample is able to cool below T_C between successive laser pulses. The measurements were also obtained using the raster scanning method described in section V. The resulting spectrogram (c) is identical to the measurement with the heat lamp on, indicating that it is the response of the metallic phase. Indeed, the raster scanning experiment showed the same result when performed with the heat lamp on and heat lamp off. A non-zero signal at negative time-delays was also observed in the latter case, showing that the preceding pulse 10 ms prior still had some effect on the XUV spectrum, additionally verifying the problems with laser-induced heating effects. Comparison with the heating lamp measurement confirmed that these changes were indeed a result of the phase transition, as opposed to alternative heating-induced semiconductor effects, such as phonon-induced renormalization of the band gap, which can sometimes be observed in laser-heated samples at negative time delays (*69*). All these observations make clear that raster scanning with linear translation stages is not sufficient to counteract accumulative heating: the sample does not cool below *Tc* between successive laser pulses, even at the reduced 100 Hz repetition rate. The rotating sample measurements, in contrast, allow for probing the true ultrafast response of the insulating phase. A detailed analysis of the physics of the insulating and metallic phase experiments, and the verification of the IMT via a fluence-dependent measurement can be found in reference (*61*). Measurements at 1 kHz, even with sample rotation, resulted in measuring the response of the metallic phase as well as permanent sample damage, where thermal switching could no longer be observed.

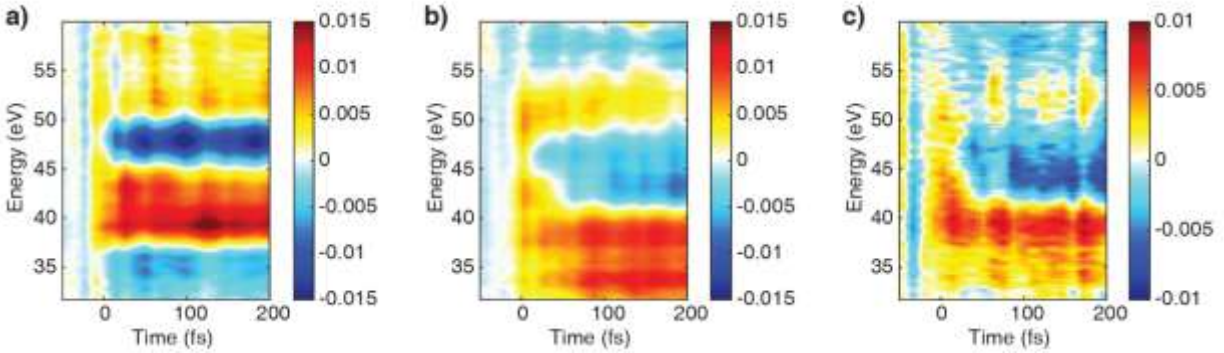

Figure 2.6. Transient absorption spectrograms for VO_2 with (**a**) rotating sample with no heat, (**b**) rotating sample with the heat lamp on, and (**c**) raster scanned sample with no heat. For (c), the negative time delay signal is subtracted for straightforward comparison.

2.3.2 Simulations

To validate the experimental results and estimate the rate of heat buildup for each case more quantitatively, time-dependent heating simulations were performed using finite-element analysis in COMSOL 5.2a. The sample geometry was defined as a VO_2 layer of 7.5 mm x 7.5 mm x 25 nm thick dimensions on a silicon nitride layer of 7.5 mm x 7.5 mm x 30 nm thick dimensions on a

silicon frame of 7.5 mm x 7.5 mm outer dimensions, with a 3 mm x 3 mm square aperture, and 525 μm thickness, in accordance with the sample geometry. For the simulation, the grid elements were generated using a triangular mesh swept through each layer, with a finer mesh used for the freestanding area and a coarser mesh used for the area over the frame. The silicon frame was treated with thermally insulating boundaries and acted as an effective heat sink. The exposed membrane surfaces (7.5 mm x 7.5 mm VO_2 area and 3 mm x 3 mm Si_3N_4 area were modeled with blackbody radiation described by the Stefan-Boltzmann law (COMSOL diffuse surface module). Convective heat dissipation is absent under the vacuum conditions employed here. The emissivity and other material properties used are listed in Table 2.1. The material properties of the *insulating* phase of VO_2 were used for the heat capacity, density, and NIR penetration depth (to reflect the initial absorption process), and the *metallic* phase value was used for the emissivity and thermal conductivity (to reflect the cooling process occurring predominantly in the final state). The enthalpy of the phase change is 4.23 kJ/mol (*70*), which corresponds to 0.58 mJ/cm^2 given the molar mass, density, and thickness of the VO_2 samples, and this factor could be neglected.

Table 2.1. VO_2, Si_3N_4, and Si material properties for heat transport

Parameter	VO_2 (ins.)	VO_2 (met.)	Si_3N_4	Si
Heat capacity, C_p [J/(g·K)]	0.66 (*43*, *71*)	0.78 (*43*, *71*)	0.7 (*72*)	0.705 (*73*)
Thermal conductivity, κ [W/(m·K)]	6.5 (*43*)	6.5 (*43*)	13 (*72*, *74*)	156 (*75*)
Emissivity, ε	0.09 (*76*) [b]	0.35 (*76*) [b]	0.005 (*77*) [b]	0.12 (*78*)
Penetration depth at 800 nm [nm]	120 (*79*)	90 (*79*)	-	-
Density, ρ [g/cm^3]	4.57 (*80*)	4.65 (*80*)	3.2 (*72*)	2.33 (*73*)

[b] Values for VO_2 and Si_3N_4 are specifically for thin films of 25 and 30 nm thickness, respectively

A periodic heat flux into the sample was implemented using a Gaussian beam profile with a 200 μm full-width at half-maximum and a fluence of 25 mJ/cm^2, matching the experimental conditions. In the beam propagation direction normal to the sample surface, an exponentially decaying thermal distribution was used for the Beer's law absorption into the VO_2 layer, using the penetration depth of the insulating phase at 800 nm. The Si_3N_4, a wide-bandgap material, was treated as non-absorbing with no incident heat flux. The temporal pulsed behavior was modeled with a rectangular waveform with a period of 10 ms and pulse duration of 0.1 ms. For the heating dynamics the femtosecond pulse duration is not important as long as the pulse energy is deposited in a time short compared to the limiting rate of cooling—in this case shorter pulse durations than specified above were shown to have no effect. For the raster scanning case the Gaussian heat source was defined at a starting position of 0.75 mm from the sample center, and the sample was translated linearly at 1.6 mm/s using a moving mesh. For the rotating motor case the Gaussian heat source was placed at an offset of 0.75 mm to the sample center, and a moving mesh was used to rotate the material relative to the spatial frame at 37 Hz. Time-dependent simulations were carried out from 0 to 30 ms with a step size of 1 ms, a solver convergence tolerance of 0.01, and using explicit events to sample across the laser pulse duration (τ) at $-\tau/5$, 0, $\tau/5$, $2\tau/5$, $3\tau/5$, $4\tau/5$, $5\tau/5$, and $6\tau/5$ relative to the pulse start time. Snapshots of the temperature profile on the sample surface are illustrated in Figure 2.7, which follow the heat dissipation of an incident pulse in the steady state limit.

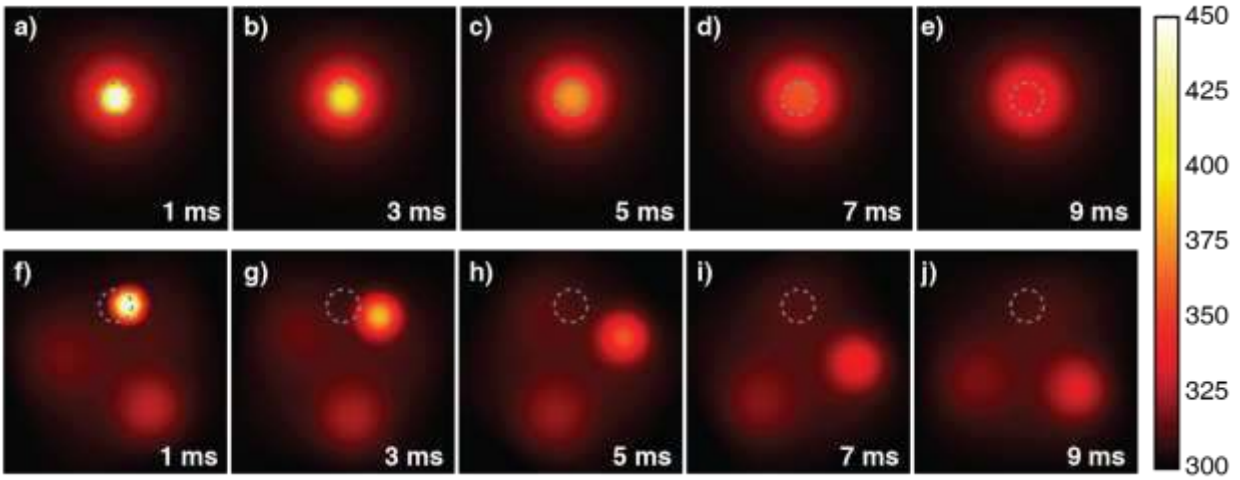

Figure 2.7. Snapshots of the temperature profile on the sample surface for sample raster scanning (a-e) and sample rotation (f-j) in the steady state limit, following the dissipation of heat in a 100 Hz experiment, over the 10 ms period between incident laser pulses. The focal volume of the laser where the next pulse will impinge is marked in dashed gray.

A global temperature probe was defined, which tracks the temperature in the focal volume for the raster scanning (in the sample center) and rotating sample geometries (at a radial offset of 0.75 mm). A plot of the temperature in the focal volume over the course of ten laser pulses is shown in Figure 2.8, comparing each case. As can be seen in the figure, in the no-rotation case the temperature in the focal volume just before each pulse climbs above T_C within six pulses, or 60 ms, even when the sample is translated continuously and at maximum speed with the linear stages. After the first six pulses, all subsequent pulses probe the response of metallic VO_2 as opposed to the insulating phase of VO_2, not sampling the IMT process. Thus, for a typical exposure time of 1 s, accumulating signal over 100 laser pulses, only 6% of the acquired XUV absorption signal would reflect the transient response of the insulating phase. In the rotating sample case on the other hand, the temperature in the focal volume reduces rapidly and in fact remains within 10 K of the starting room-temperature value preceding each laser pulse, thus providing an accurate probe of the response of the insulating phase.

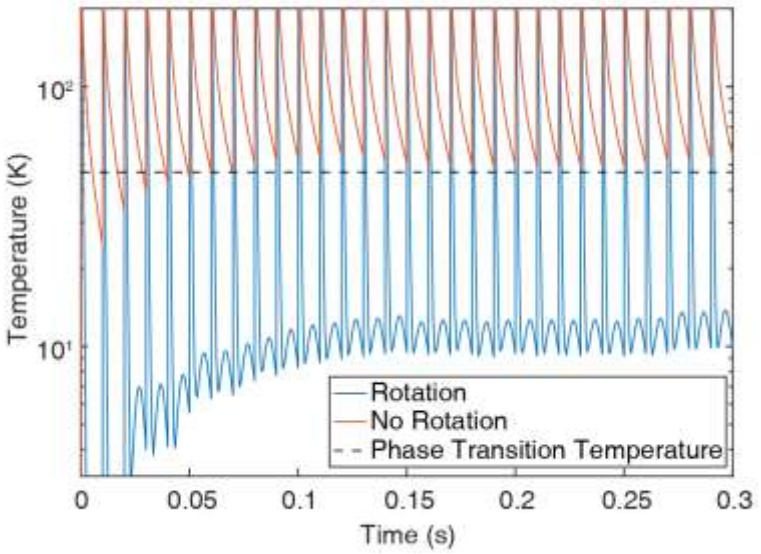

Figure 2.8. Temperature change in the focal volume of the laser is plotted on a logarithmic scale for the case of raster scanning with no sample rotation (blue) and for sample rotation (orange). Small local maxima in the rotating sample data correspond to a previously irradiated part of the sample passing through the focal volume.

The presented results show the optimal case of raster scanning, where the stage is continuously moving, which is still insufficient for thin film VO_2 samples in a 100 Hz experiment. In most experiments the stage is paused at each position on the sample for some time, leading to even higher temperature buildup. Some supplementary cooling can be provided by other methods, e.g. introducing a flow of inert and XUV transparent gas over the sample front and back surface for convective cooling, cooling the ambient surroundings to act as a blackbody heat sink, using a gridded substrate such as a TEM grid and sending the beam between the thermally conductive bars, or coating VO_2 on a thin layer of an inert, more thermally conductive material such as diamond. However, particularly for samples with pulse-to-pulse sensitivity, rapid sample rotation represents a clean way to get injected heat out of the focal volume, and it results in no loss in signal. The motor frequency used in this work is not a unique solution, and in general it should be based on a consideration of Equation 2.1, where f_{rot} and f_{rep} are the motor rotation frequency and laser repetition frequency, respectively, r is the radius of rotation, d_{beam} is the beam diameter, and n is the desired integer number of beam diameters between pulses.

$$2\pi \times r \times (f_{rot}/f_{rep}) \geq n \times d_{beam}, \qquad \text{Equation 2.1}$$

The motor frequency used in the presented experiment corresponds to 10 d_{beam} between subsequent pulses, although a lower frequency could certainly be used in this case. The motor frequency should also ideally be out of phase with the repetition rate, to maximize the time before the same sample area is irradiated again. For even more sensitive samples linear motion can be combined with rapid sample rotation, to spiral over the sample surface, and if possible sample size can be increased, which would allow for working at a larger radius and possibly even higher repetition rates. Whether such measures are necessary depends on the specific thickness-dependent thermal properties of the sample under investigation.

2.3.3 Conclusions

An attosecond transient absorption beamline is presented that is tailored to investigating thin film samples and nanostructures, utilizing a rotating sample mount to mitigate heat buildup. The system is capable of stabilizing measurements to sub-femtosecond resolution for up to 48-hour experiments. Sensitive diagnostics are included for measuring high quality static XUV and NIR transmission spectra, both at room temperature and for samples heated *in situ*, as well as characterizing fluences and pump beam power incident on the sample.

The presented experimental and simulated data on vanadium dioxide demonstrate the care that must be taken in such measurements, and the necessity of going beyond raster scanning when working with truly heat sensitive samples. While some of the elements of this apparatus are specific to XUV measurements, the conclusions regarding heat transport are general to thin film samples in vacuum. The hollow-shaft motor scheme presented demonstrates one way of mitigating these effects. While such measures may not be required for higher thermal conductivity samples such as silicon or generally thicker samples, it is critical to consider the thermal properties of the system being investigated and the reversibility or irreversibility of the process at hand.

Chapter 3. Few-Femtosecond Extreme Ultraviolet Transient Absorption of the Insulator-to-Metal Phase Transition in Vanadium Dioxide

The content and figures of this chapter are reprinted or adapted with permission from M. F. Jager, C. Ott, P. M. Kraus, C. J. Kaplan, W. Pouse, R. E. Marvel, R. F. Haglund, D. M. Neumark, and S. R. Leone.

"Tracking the Insulator-to-Metal Phase Transition in VO_2 with Few-Femtosecond Extreme UV Transient Absorption Spectroscopy," PNAS, [In Press], (2017).

Coulomb correlations can manifest in exotic properties in solids, but how these properties can be accessed and ultimately manipulated in real time is not well understood. The insulator-to-metal phase transition in vanadium dioxide (VO_2) is a canonical example of such correlations. Here, few-femtosecond extreme ultraviolet transient absorption spectroscopy (FXTAS) at the vanadium $M_{2,3}$ edge is used to track the insulator-to-metal phase transition in VO_2. This technique allows observation of the bulk material in real time, and follows the photo-excitation process in both the insulating and metallic phases, probes the subsequent relaxation in the metallic phase, and measures the phase transition dynamics in the insulating phase. An understanding of the VO_2 absorption spectrum in the extreme ultraviolet is developed using atomic cluster model calculations, revealing V^{3+}/d^2 character of the vanadium center. It is found that the insulator-to-metal phase transition occurs on a timescale of 26±6 fs and leaves the system in a long-lived excited state of the metallic phase, driven by a change in orbital occupation. Potential interpretations based on electronic screening effects and lattice dynamics are discussed. A Mott-Hubbard type mechanism is favored, as the observed timescales and d^2 nature of the vanadium metal centers are inconsistent with a Peierls driving force. The findings provide a combined experimental and theoretical roadmap for using time-resolved extreme ultraviolet spectroscopy to investigate non-equilibrium dynamics in strongly correlated materials.

3.1 Introduction

3.1.1 Motivation

The Coulomb interaction of charges in a solid depends sensitively on local screening, bonding structure, and orbital occupancy. These electronic correlation effects are known to manifest themselves in unusual properties, such as superconductivity, colossal magnetoresistance, and insulator-to-metal phase transitions (IMTs), which can be switched on or off via small perturbations. Understanding if and how these correlation-driven properties can be manipulated in

real time will open the door to using these materials as ultrafast photonic switches and will establish the electronic speed limits for next-generation devices (*81–83*).

Following the real-time dynamics of carrier interactions necessarily requires time-resolving the excitation and relaxation of electron correlations. Studies at longer time scales are complicated by simultaneous effects of structural distortion together with carrier screening and thermalization. In contrast, few-femtosecond extreme ultraviolet absorption spectroscopy (FXTAS) provides temporal resolution close to the Fourier limit for single-photon excitation with broadband visible light. It has the capability to separate electronic and structural effects on the basis of their intrinsic timescales and can isolate early-time electronic dynamics spectroscopically via atom-specific core-level electronic transitions (*20*, *54*). Previous few-femtosecond and attosecond measurements of electron dynamics in solid-state systems have been restricted to simple band insulators or semiconductors and metals in which dynamics are initiated by the interaction with strong electric fields (*20*, *84–89*). FXTAS measurements of the IMT process are reported following single-photon excitation in vanadium dioxide (VO_2), a promising material for strongly correlated devices, and resolve the timescale of the IMT.

3.1.2 Background Information

The insulating phase of VO_2 has monoclinic symmetry with dimerized pairs of vanadium atoms forming 1D chains within the crystal structure. As illustrated in Figure 3.1, these bonds are broken and the crystal adopts a more symmetric rutile structure upon transition to the metallic phase at 340 K. The relative significance of the structural distortion in mediating the IMT has long been debated, and the driving force of the IMT in VO_2 has been described alternatively as the result of a Peierls-like structural instability, electron correlation and Mott-Hubbard effects, or a complex interplay of both (*90–96*). Previous time-resolved experiments on VO_2 have provided intriguing results: early optical (*97*, *98*) and x-ray (*99*) measurements established sub-picosecond switching times, measuring shorter and shorter timescales until an 80 fs bottleneck for the phase transition was observed in 2004 (*37*). However, more recent experiments in time-resolved photoemission (*38*) and transient reflectivity (*100*) have not observed the bottleneck, and measured speeds <60 fs, which were limited by the temporal resolution of the experiment. In single crystal microrods, timescales were found to vary from 200 fs (non-pulse duration limited) to 40 fs (pulse duration limited) (*39*). Time-resolved electron diffraction (*101*, *102*) has established that dilation of the V-V dimers occurs within ~300 fs, and a coherent stretching of this mode has been observed following the phase transition (*37*, *100*, *103*), but the role of electronic versus structural effects at the earliest timescales is still not well understood. The work here establishes a 26±6 fs timescale for the phase transition following single-photon excitation with a few-cycle femtosecond laser pulse, not limited by the 5.6±0.8 fs instrument response function measured *in situ*. It is noted that the ultrafast timescale, coupled with the finding of a d^2 ground state is inconsistent with a structural Peierls transition, and lends support for Mott transition mechanisms.

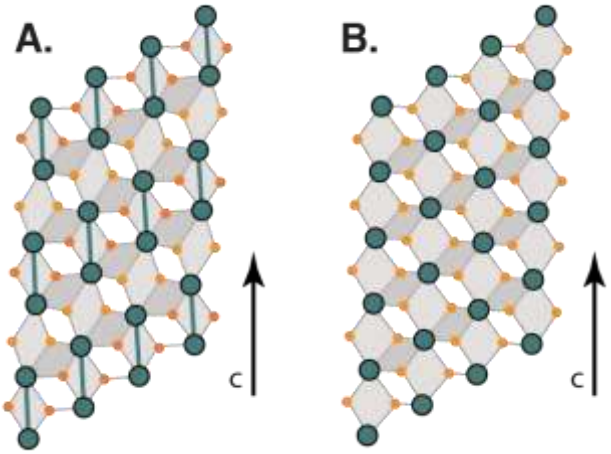

Figure 3.1. (**A**) The insulating ground state of VO_2 (V atoms: grey, O atoms: orange) exhibits a monoclinic crystal structure with dimerized chains of vanadium atoms along the c-axis and two different types of oxygen sites, those between the bonded vanadium atoms, and those between the non-bonded vanadium atoms. (**B**) The final metallic state of the system has a rutile crystal structure in which the vanadium dimerization has been melted.

3.1.3 Experimental Scheme and Measurement Details

The static XUV $M_{2,3}$-edge absorption spectrum of VO_2 is measured for both the insulating and heat-induced metallic phases in transmission geometry, using attosecond pulses that cover a spectral range from 30 to 60 eV. The samples are 25 nm thick polycrystalline thin films of VO_2 deposited on 30 nm thick freestanding Si_3N_4 substrates, which are rapidly rotated to prevent the accumulation of heat from successive laser pulses. The transient evolution of this vanadium edge structure is followed in real time via FXTAS as schematically illustrated in Figure 3.2, which highlights the changes in the electronic structure of VO_2 across the IMT. A sub-5 fs near-infrared (NIR) laser pulse centered at 760 nm impinges on VO_2 in its insulating phase, serving as the pump step to induce the IMT. Time-delayed broadband XUV attosecond pulses are then collinearly transmitted through the VO_2 thin film, probing the core-level absorption of the bulk material around the vanadium 3p transition ($M_{2,3}$ edge) at 39 eV (*104*).

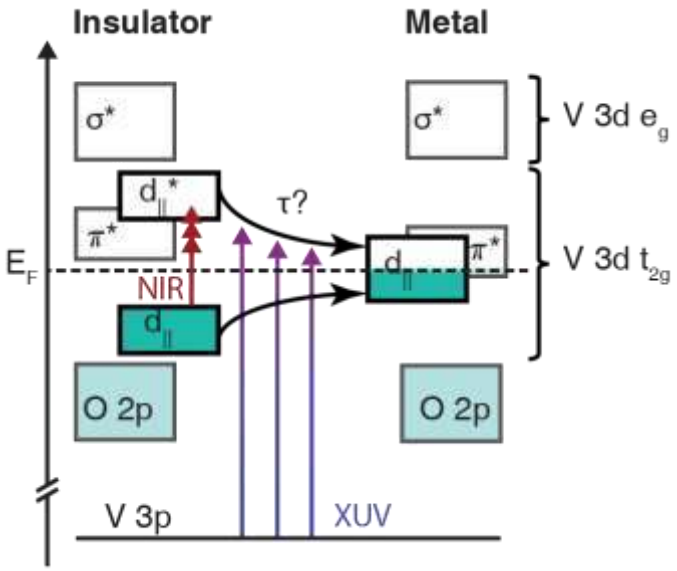

Figure 3.2. The electronic structure of VO_2 is depicted and can be understood via crystal field theory, where the d-orbitals denoted d‖ align parallel to the c-axis of the crystal. Electrons excited across the band gap with a few-fs NIR pulse initiate the IMT, and the progress is tracked via core-level transitions into the unoccupied conduction and valence band states using time-delayed attosecond pulses.

To produce the pump and generation pulses, carrier-envelope phase stabilized pulses from a Femtopower Compact Pro amplifier are compressed to 5 fs duration and 750 μJ pulse energy using self-phase modulation in a neon-filled (2 bar static filling) hollow-core fiber and a chirped mirror compressor. The compressed pulses have a continuous spectrum spanning from 400 to 1000 nm and were characterized using dispersion-scan [Sphere Photonics (*62*)] to have a duration of 4.9 fs, as shown in Figure 3.3.

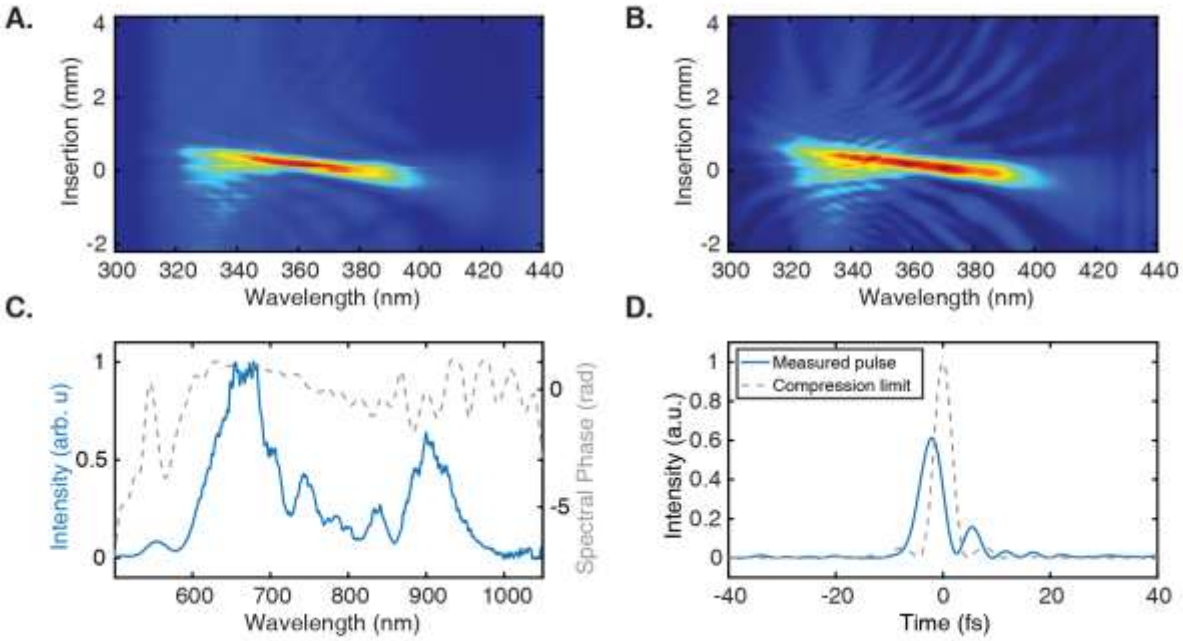

Figure 3.3: Dispersion-scan (Sphere Photonics) characterization of the NIR pulse, showing a 4.9 fs full width at half maximum and a small post-pulse. The measured d-scan trace (**A**) is reconstructed in (**B**). The retrieved phase is shown overlaid on the pulse spectrum in (**C**), and the intensity reconstruction is shown in (**D**), along with the compression limit for the pulse duration, assuming a flat spectral phase.

The 1 kHz repetition rate is reduced to 100 Hz using an optical chopper to avoid sample damage, and the beam is split into two arms using an 80%-20% broadband beam splitter, as shown in the optical layout in Figure 3.4A. Probe pulses are generated using the 80% majority arm, by focusing ~400 μJ 5-fs pulses into a krypton gas target to generate a sub-5 fs attosecond pulse train with a continuous spectrum of extreme ultraviolet (XUV) light spanning from 30 to 60 eV, via high harmonic generation. A representative spectrum is shown in Figure 3.4B. Residual NIR light from the generation process is removed by transmitting the XUV through a 200 nm thick aluminum filter. The XUV pulse is focused through the VO_2 sample using a grazing incidence gold-coated toroidal mirror (ARW Corporation). The 20% pump arm is time-delayed using a retro-reflector on a piezo delay stage with sub-nanometer positional stability (Physik Instrumente). The pump beam is then focused through the sample collinearly with the probe beam by recombining on a 45º annular mirror, where the pump arm is reflected and the probe arm is transmitted. The NIR beam is focused to ~200 μm full-width at half-maximum (FWHM) on the sample, and the XUV beam to ~60 μm FWHM. After the sample the NIR beam is blocked using a pinhole and a 200 nm aluminum filter. The XUV transmission spectrum through the sample is diffracted using a grazing-incidence variable-line-spacing reflection grating (Hitachi) and recorded on an XUV CCD camera (Princeton Instruments PIXIS). The spectral resolution was determined to be ~50 meV at 45 eV, calibrated using the linewidths of the $2s^12p^6np$ ($n = 3,4,5\ldots$) Rydberg series of inner-valence excitations in neon (*105*).

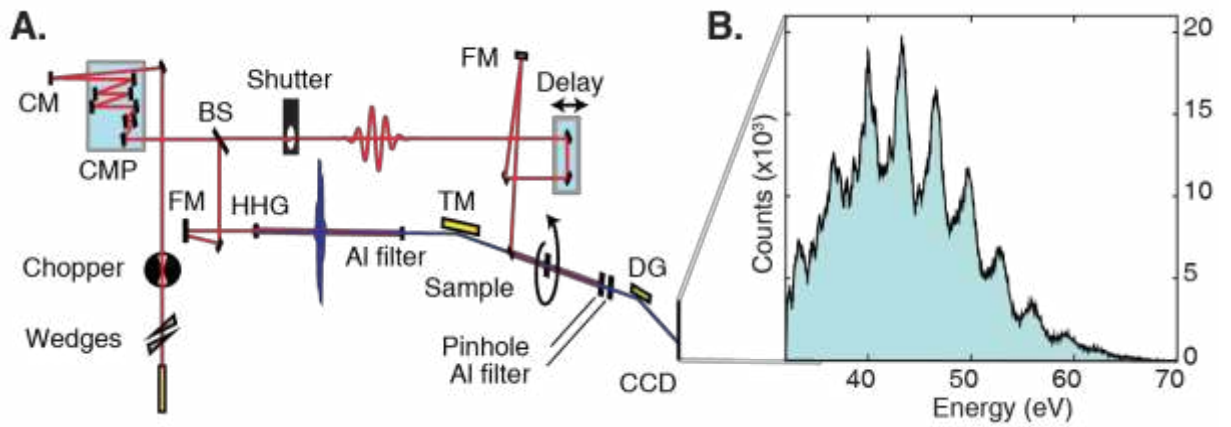

Figure 3.4. (**A**) The optical layout of the experiment: CM = collimating mirror, CMP = chirped mirror compressor, BS = beam splitter, FM = focusing mirror, HHG = high harmonic generation, DG = diffraction grating. (**B**) A representative high harmonic spectrum used in the experiment, at 100 ms exposure time and 100 Hz repetition rate.

The total instrument response function is monitored *in situ* via transient absorption of neon atoms and is measured at 5.6±0.8 fs (details in section 3.4.2). The time-dependent changes in absorption are measured directly via changes in the optical density (ΔOD) in a NIR-pump-on / NIR-pump-off measurement. Transient absorption experiments are carried out on both the low-temperature insulating phase and the higher-temperature metallic phase of VO_2 (produced via a quartz halogen heat lamp) at an incident laser fluence of 25 mJ/cm^2, well above the fluence threshold to induce the phase transition [see reference (*101*) and section 3.4.4]. The experiments on the hot metallic phase serve as a reference for the ultrafast response to interband electronic excitations and provide a direct measurement of the XUV absorption spectrum of the photoexcited metallic phase.

The typical acquisition time to acquire a high quality (2-3 mOD noise level / 15 mOD signal) scan under these conditions was 48 hours, averaging ~300 back-to-back time-delay scans. The relatively long measurement time predominantly resulted from being forced to acquire data at a reduced 100 Hz repetition rate to avoid accumulative thermal effects. Spatial overlap of pump and probe beams was maintained by using a single point beam stabilization in both pump and probe arm. In order to compensate for time-delay drifts over the long measurement periods, a transient absorption measurement would be taken through a neon gas target between each VO_2 scan, by laterally translating the solid sample out of the focal area and moving a gas cell in, without changing any other experimental conditions. Neon exhibits a large amplitude response of the XUV absorption to overlapping and time-delayed NIR pulses, the physics of which are described in section 3.4.2. This allowed high-quality neon scans to be taken within 2-3 minutes, and the time reference to be re-calibrated approximately every ten minutes. Samples were checked before and after each full measurement to ensure that thermal switching behavior was still observed, by recording the transmission of the NIR pump pulse picked off after the sample, as shown in Figure 3.5, below.

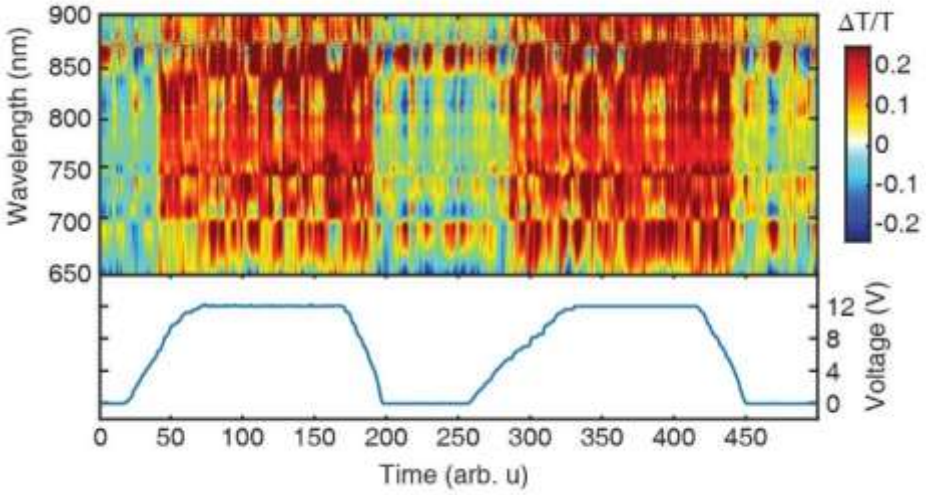

Figure 3.5: Transmission of the NIR pump pulse through the sample in vacuum, while modulating the sample temperature using a heating lamp. The phase transition appears as an abrupt change in transmission when the critical temperature is reached at a certain supply voltage of the heating lamp.

3.2 Static Spectrum Measurements and Simulations

3.2.1 Static Spectrum Measurement

Static absorption spectra were recorded using only the XUV beam and alternating between a sample and a reference target, i.e., a VO_2 sample and a bare Si_3N_4 membrane. The samples were alternated rapidly using fast vacuum translation stages (Physik Instrumente) in order to compensate for fluctuations and systematic drifts of the high harmonic flux, and obtain spectra with sub-1-mOD accuracy. Spectra of the metallic phase of VO_2 were obtained by heating the sample in vacuum using a quartz halogen lamp. Samples were checked for uniformity both via optical microscope and by performing a transmission map measurement in the XUV, where the integrated XUV flux was measured as a function of 2D position on the sample surface, and found not to vary by more than ±5%.

The measured XUV static absorption spectrum around the vanadium $M_{2,3}$ edge is shown in Figure 3.6, for both the insulating and metallic phases. The spectral shape of the measured core-level transition is in excellent agreement with XUV reflectivity measurements of single crystals in the same energy range (*106*). The signal at low energies (E < 39 eV) is assigned to transitions into the continuum from the oxygen 2s core level and from the oxygen-2p–vanadium-3d hybridized valence band. In order to isolate the contribution to the spectrum from the vanadium core-level absorption, the ionization-type background can be fit using the signal below 35 eV, well below the onset of the vanadium M-edge. A 1/E type form provides the best fit between 20 and 35 eV, based on the data in the CXRO database (*107*). This background can be subtracted across all energies to obtain the isolated $M_{2,3}$ edge spectrum.

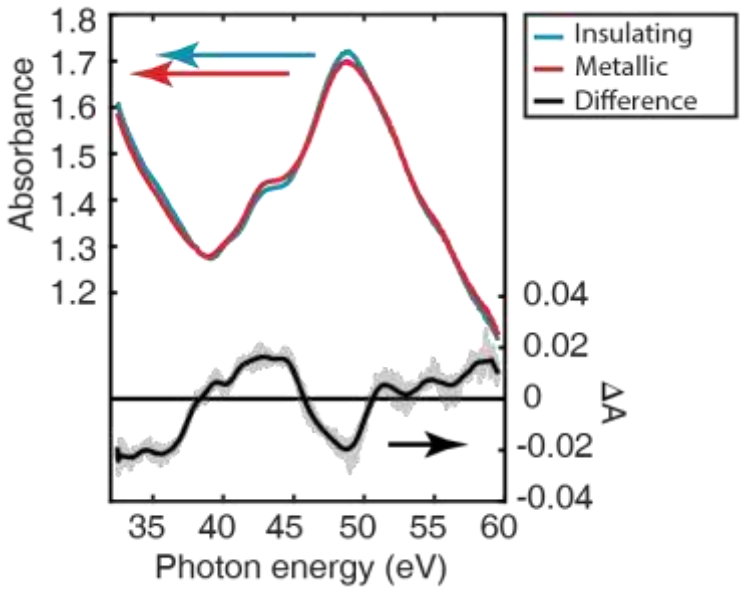

Figure 3.6. Static XUV absorbance spectra of the insulating (blue) and metallic (red) phases of VO_2 are presented on the left-hand y-axis. The difference in absorbance (black) is shown magnified in the lower part of the figure, on the right-hand y-axis, with error bars shown in gray.

3.2.2 Atomic Multiplet Simulations

The $M_{2,3}$ edge absorption spectrum is simulated using atomic multiplet theory, as the L- and M-edge spectra of transition metals are known to be dominated by localized atomic effects (*108*). Spectra were simulated for VO_2 using the software CTM4XAS 5.5 (*109*), an atomic multiplet simulation code that accounts for the strong mixing of the core and valence wavefunctions in the presence of a core vacancy. Because of this effect the spectrum cannot be treated as a partial density of states of the conduction band. Stated another way, due to the reordering of transition energies, spectral features cannot be linearly mapped to corresponding bands or delocalized orbitals. The calculation was performed in octahedral (O_h) geometry with a crystal field strength, 10Dq, of 3.3 eV (*106*). Atomic Hartree–Fock values were used and the charge-transfer effect is neglected in the final state. The generated stick spectra were then multiplied with a Gaussian lineshape of 50 meV full-width at half-maximum to account for the experimental energy resolution. Interference between direct ionization from the V 3d channels and autoionizing channels of the V 3p core-hole excitation is significant in these systems, resulting in an asymmetric Fano-type lineshape (*32*, *110*). The Fano lineshape must be convoluted with the Gaussian energy resolution to retrieve the lineshape of each transition. This was done using a pseudo-Voigt profile, with a Fano lineshape used in place of a Lorentzian. The spectra were normalized and the *q*-parameter was allowed to vary to obtain the best fit. The Fano linewidth was increased linearly by 0.1 eV/eV starting at a width of 1.1 eV at 35 eV in order to account for the energy-dependent core-hole lifetime (*111*).

While consideration of formal oxidation states might suggest modeling VO_2 as a V^{4+}, or d^1, metal center, there is considerable evidence that, due to strong hybridization, the vanadium site in VO_2 is actually closer to d^2 electron occupation (*91*, *112–114*). The atomic multiplet calculation was performed for both a V^{3+} and V^{4+} metal center at the 3p resonance for comparison. The results of the simulation for the V^{3+} metal center are shown in Figure 3.7A, which had a best-fit Fano parameter of q = +2.4 [well in the range of typical Fano parameters for transition metal M-edges: q = 0.7 - 3.5 (*110*, *115–117*)]. The result of the calculation for the V^{4+} metal center is shown in Figure 3.5B, with a best-fit Fano parameter of q = +3.1, showing significantly worse agreement overall, which supports the conclusion of a more strongly hybridized vanadium center in VO_2 (*112*).

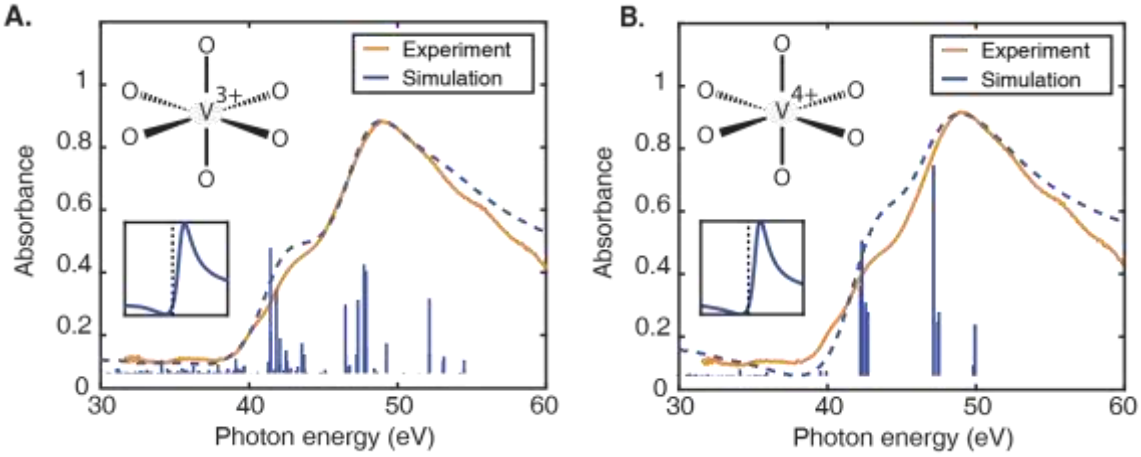

Figure 3.7. (**A**) The vanadium $M_{2,3}$ edge (orange) of the insulating phase spectrum after removing the low-energy ionization contribution. A cluster-model calculation (blue) is shown for a V^{3+} system. The transition energies and amplitudes are convoluted with the inset q = 2.4 best-fit Fano profile to account for final-state interference effects, which maps the stick spectrum to the final simulated spectrum (blue dashed line), where due to the Fano asymmetry, spectral weight is shifted to higher energies. The same computation is shown in (**B**) for a V^{4+} metal center, with a q = 3.1 best-fit Fano profile, showing significantly worse agreement.

3.3 Transient Absorption Measurements

3.3.1 Transient Absorption Measurement Details

Transient absorption spectra were recorded using pump-on / pump-off measurements, where at each time delay a spectrum is saved first with the pump beam switched off and then with the pump beam switched on by means of a computer-controlled optical shutter. This procedure allows spectra to be recorded rapidly back-to-back for higher quality data. The transient absorption measurements were taken in 2 fs steps from –30 to +30 fs, in 5 fs steps from +30 to +100 fs, and in 10 fs steps from 100 to 220 fs, with a repetition rate of 100 Hz and an exposure time of 1 s. In order to prevent accumulation of heat in the sample it is critical that subsequent laser pulses do not impinge on the same area of the sample, as heat dissipation in the thin-film samples in vacuum is

comparable to the 10 ms inverse laser repetition rate after the optical chopper (see chapter 2.3). To counteract this, the samples were rapidly rotated normal to their surface by mounting the sample in a hollow-shaft motor rotating at 37±3 Hz, and the beam was transmitted at a 0.75 mm radius relative to the motor axis. The material's response in the metallic phase was measured by performing the transient absorption measurement with the heating lamp on as a reference. It was confirmed that without the rotating motor turned on the samples displayed the dynamic response of the metallic phase. With the spinning motor turned on, the response of the insulating phase could be clearly isolated, evidenced by the absence of any significant signal at negative delays and a qualitatively different measured transient signal. A transient absorption experiment was also performed on a bare Si_3N_4 substrate and it was confirmed that the substrate material was optically transparent and inert to the pump pulses.

High-quality transient measurements were taken at 25 mJ/cm^2. A transient absorption measurement out to +60 ps was also taken, using 25 fs steps from –100 to +200 fs, 50 fs steps from +200 fs to 1 ps, 0.25 ps steps from 1 ps to 10 ps, and 10 ps steps from 10 to 60 ps, at a fluence of 25 mJ/cm^2, the results of which will be described in the following sections.

3.3.1 Transient Absorption Measurement Results

The time evolution of changes to the $M_{2,3}$ edge absorption spectra are shown in the FXTAS spectrograms in Figures 3.8A and B, for the metallic and insulating phases, respectively. In both cases, the system displays an abrupt response due to the initial photoexcitation and reaches a steady state within less than 100 fs, with the insulating phase equilibrating significantly faster than the metallic phase. In order to compare the data sets the ΔOD changes must be plotted with respect to the same reference spectrum. The metallic phase is treated as the sum of ΔOD changes first upon heating and subsequently upon photoexcitation (as illustrated in Figure 3.8C ,where the purple curve in the lower panel is the sum of the red and blue curves in the upper panel), yielding the purple curve in the lower panel). This gives the cumulative ΔOD changes with respect to the insulating-phase static spectrum, which can be compared to the signal at late time delays measured in the insulating phase directly, in the lower panel of Figure 3.8C. The two core-level ΔOD spectra agree very closely, implying the final state in each case is the same excited state of the metallic phase. Measurements of the fluence dependence (section 3.4.4) further confirm that the signal observed in the insulating phase displays a critical fluence threshold and saturation, confirming that it indeed corresponds to the phase transition.

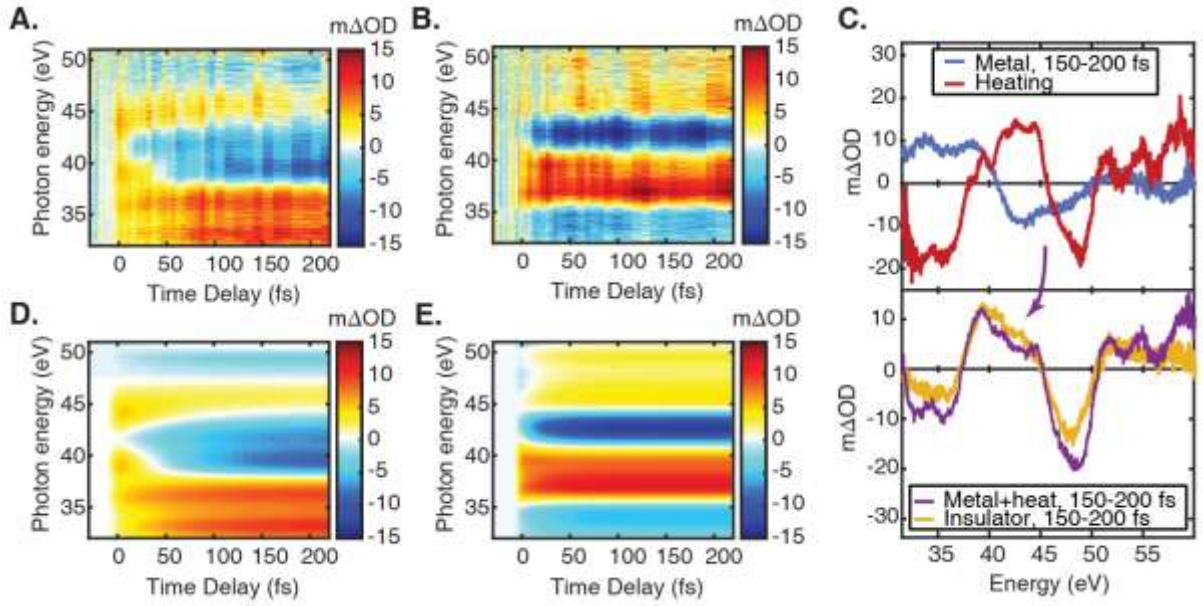

Figure 3.8. Transient absorption spectrograms are shown for the metallic phase (**A**) and insulating phase (**B**) of VO_2, at an incident fluence of 25 mJ/cm^2. (**C**) A comparison of the systems at late time delays shows that the insulator and metal reach the same final state. The metallic-phase ΔOD with respect to the insulating-phase static spectrum, shown in purple in the lower panel, is equal to the sum of the changes first upon heating (red curve, upper panel) followed by photoexcitation (blue curve, upper panel). Note that the red curve is identical to the difference spectrum in Figure 3.6. The global fits for the metallic and insulating phases are shown in panels (**D**) and (**E**), respectively.

3.3.2 Dynamics in the Insulating and Metallic Phases

The metallic-phase dynamics highlight the significant effects that carrier excitation can have on the spectrum, independent of the phase transition. The initial excitation with a NIR pulse excites dominantly ligand-to-metal charge transfer type transitions, which affect the allowed XUV dipole transitions and alter the shape of the spectrum. The dynamics can be globally fit with a two-component model, with an early-time spectral component corresponding to the non-equilibrium charge distribution immediately following photoexcitation and a late-time spectral component corresponding to the charge distribution following carrier-carrier and inter-valley (carrier-phonon) scattering. The global fit is performed using first-order kinetics (see section 3.4.3) and the calculated spectral components and their corresponding kinetic behaviors are illustrated in Figures 3.9A and B, respectively. The tensor product of these curves gives the full 2D global fit that is shown in Figure 3.8D. The global fit captures all of the observed dynamics and is a more rigorous way to account for broadband effects, as opposed to fitting of single lineouts. A 69±11 fs time constant is obtained for the metallic phase kinetics (orange and blue curves, Figure 3.9B).

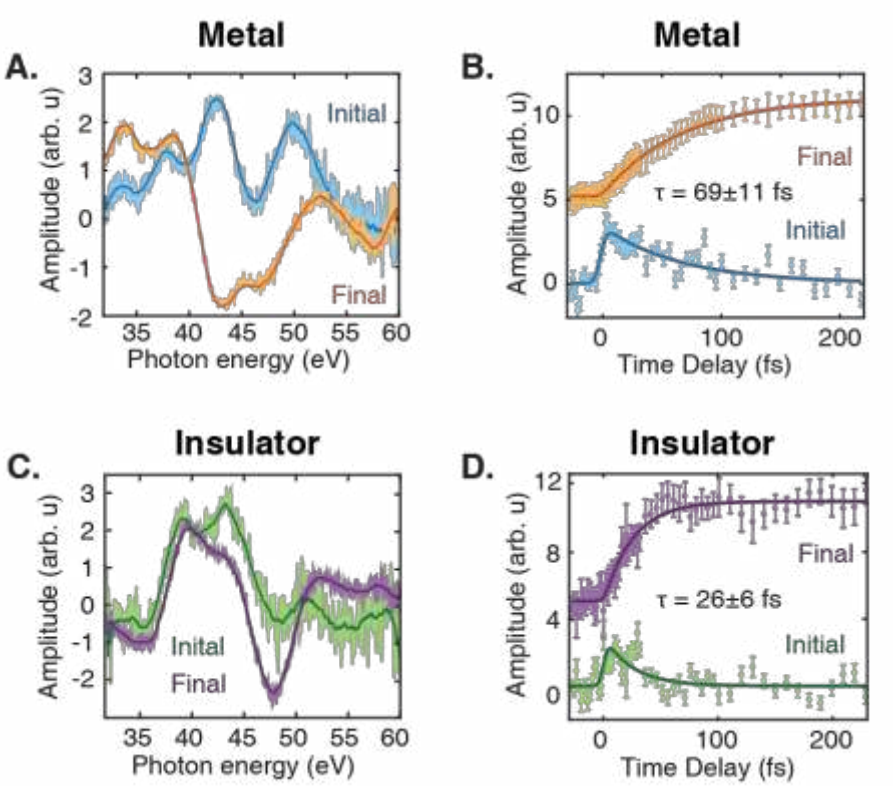

Figure 3.9. (**A**) Spectral signatures of the initial (blue) and final (orange) charge distributions observed in the metallic phase data. Statistical error is apparent from the line fluctuations. The kinetic behavior of each of these spectra in the metallic phase is shown in panel (**B**) where corresponding spectra and kinetics are shown in identical colors. The data points are the result of fitting the ΔOD spectrum at each time delay to a superposition of the two spectral curves in panel A. The results highlight the quality of agreement of the global fit. Analogous spectral and kinetic fit components for the insulating phase are plotted in panels (**C**) and (**D**), respectively, showing much faster kinetics.

In the insulating phase, as in the metallic phase, the time-dependent data are well described by single-exponential kinetics. Biexponential kinetics, related to a separable observation of carrier thermalization and the IMT, are not discernable in the data. The insulating phase is thus also fit by a two-component model, which describes the evolution of an initial excitation to a final charge distribution, encompassing the IMT. The phase transition proceeds directly into an excited state of the metallic phase, as was found by the comparison at late time delays with the photo-excited metallic phase, shown in Figure 3.8*C* (bottom panel). The spectral signatures of the initial and final states of the insulator are shown in Figure 3.9C, and the corresponding kinetics are shown in Figure 3.9D. The time constants of both the rise and decay (purple and green curves) are globally fit with a value of 26±6 fs. The formation of this final state represents an IMT into a long-lived *excited* state of the metallic phase, which persists out to more than +60 ps, as shown in Figure 3.10.

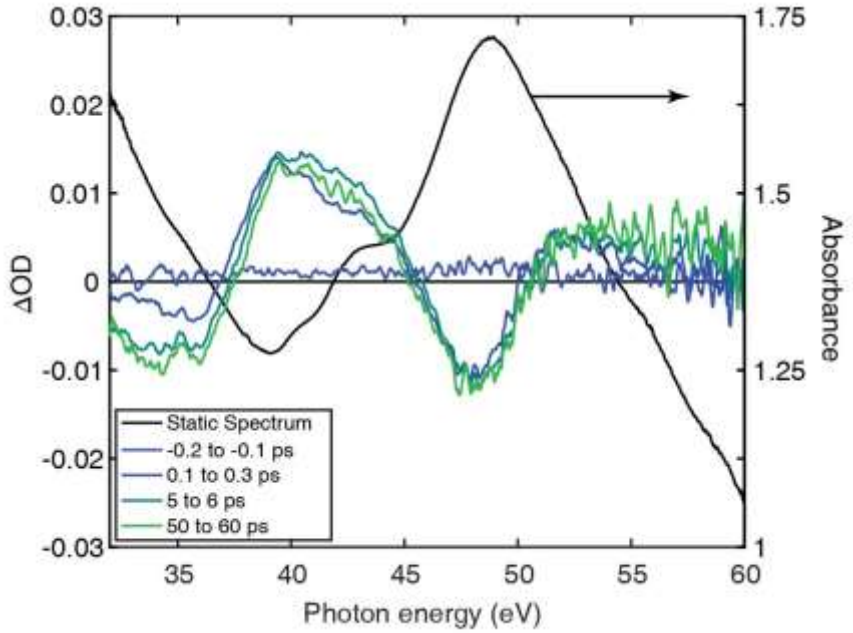

Figure 3.10: Results of a transient absorption measurement on VO_2 out to +60 ps. The ΔOD changes are shown on the left hand y-axis in blue to green colors, and the static absorption spectrum is shown in black on the right hand y-axis, for reference. Only slight changes are observed on this timescale below the $M_{2,3}$ edge onset.

On the picosecond timescale little additional modification to the ΔOD is observed, with the only change being a slight further decrease in absorption from 32-36 eV. The static absorption spectrum is plotted in Figure 3.10 for reference, showing that this energy region occurs at energies below the main onset of the $M_{2,3}$ edge at 39 eV, in the portion of the spectrum dominated by ionization from the O 2s core level and the (mainly O-2p-character) valence band. The changes are observed on a ~2 ps timescale, which matches very closely with the 1.6 ps timescale observed by Morrison et al. (*102*) in time-resolved electron diffraction, which was attributed to a 1D reorganization of valence charge density along the c-axis of the crystal, mediated by electron-phonon coupling.

As noted, the phase transition and carrier thermalization processes are not distinguishable in the data of the insulating phase. As described in section 3.4.3, a three-component fit that attempts to separate these effects retrieves only one timescale for both the carrier thermalization and the insulator-to-metal transition, and no signature of the longer timescale measured in the metallic phase is discernable. This may be due to differences in the excitation step, which in the metallic phase exhibits more ligand-to-metal charge transfer type transitions (O 2p to V 3d-bands) and the insulating phase exhibits more $\sigma \rightarrow \sigma^*$ (or $d_{\|}$ to $d_{\|}^*$) type transitions, as illustrated in Figure 3.2. In the final state, electrons and holes thermalize to the band edge, which has d-band character; thus this process may be apparent only in the metallic case, where the scattering processes result in a net change of oxidation state.

3.3.3 Discussion of Results

The XUV measurements directly probe the electronic response of the vanadium atoms in the bulk material, establishing that the ultrafast response is not limited to the surface (*38*) or to single-crystal samples (*39*). The excited carrier density in this experiment, n_e, is estimated to be ~5x10^{21} cm^{-3} given the experimentally measured fluence of 25 mJ/cm^2, a central photon energy of 760 nm, and a mean penetration depth for VO_2 of ~180 nm at this wavelength (*39*). The plasma frequency ω_p is then given by

$$\omega_p = \sqrt{\frac{n_e e^2}{m^* \varepsilon_0}} \qquad \text{Eqn. 3.5}$$

where e is the elementary charge and ε_0 is the vacuum dielectric permittivity. The effective mass m^* in VO_2 has been measured to range between 1.7 and 7.0 times the free electron mass m_e (*43*). A value of $m^* = 7\ m_e$ is taken here to provide a lower limit on the plasma frequency and an upper limit on the plasma period, yielding values of 1.5 PHz and *4.2 fs*, respectively. The observed dynamics are significantly slower, with a 26±6 fs timescale.

While the plasma frequency is frequently associated with screening, there is some evidence that purely electronic bottlenecks could be longer for Mott transitions (*118*). Indeed, the electronic screening time may be a complex function of orbital-specific carrier occupation and mobility, where only a subset of the excited carriers can participate in the relevant local screening. A free-carrier screening-mediated Mott transition is schematically illustrated in Figure 3.11. Upon exciting an electron-hole plasma, the carriers are spatially distributed according to the oscillator strengths and joint density of states of the interband transitions. As Coulomb forces drive these carriers to new equilibrium spatial distributions the ionic vanadium sites of the lattice are progressively screened. The screened Coulomb potential (frequently described by a Yukawa potential, as illustrated in Figure 3.11) narrows and can reach a critical point where the d-electrons, initially localized on the vanadium sites, are no longer bound and the system becomes metallic, as in a doping-driven Mott transition (*36*, *119*, *120*).

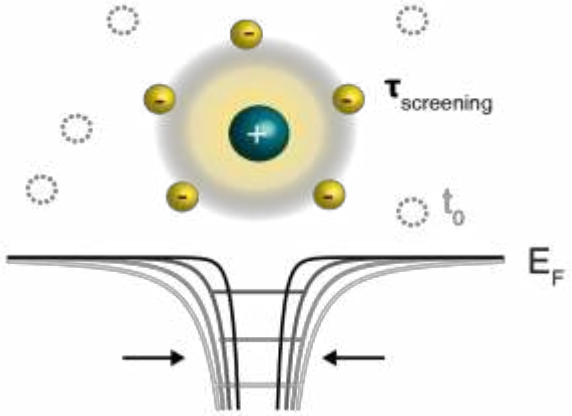

Figure 3.11. Schematic of how the phase transition can occur in time as the carriers redistribute spatially to screen the ion cores. The potential well changes from a Coulomb potential (light gray) to a screened Coulomb, or Yukawa potential (dark gray to black), while the horizontal lines represent the binding energy of the d-electron, leading up to the Fermi level. As the potential is screened and narrows, eventually a bound state is no longer supported.

Considering a structural involvement, the 26±6 fs timescale observed for the IMT is well below the 160 fs-period of the A_g phonon mode previously thought to create a structural bottleneck for the phase transition (*37*). The fastest phonons previously hypothesized to play a role in the IMT have a period of 98 fs (*121*) and are related to the V-V dimer stretch. However, the timescale measured here is more consistent with the half period of octahedral V-O-V bending modes at 620 cm^{-1}, which have a period of 55 fs (*122*). New lattice vibrations could also occur on the excited state potential, which is altered as a result of pump-pulse induced changes in orbital occupation (*100*, *103*, *123*). The process is schematically illustrated in Figure 3.12. The resulting displacement can alter the overlap of atomic orbitals and screening, leading to a bandwidth-driven Mott transition (*36*). While a 1D Peierls type mechanism has often been discussed, the classical Peierls instability is a feature of d^1 systems (*41*), whereas VO_2 is determined here to be more accurately d^2. Additionally, the short IMT timescale measured here, which does not align well with vibrational modes typically associated with a Peierls transition (*37*, *121*) , lends support to a Mott-like picture.

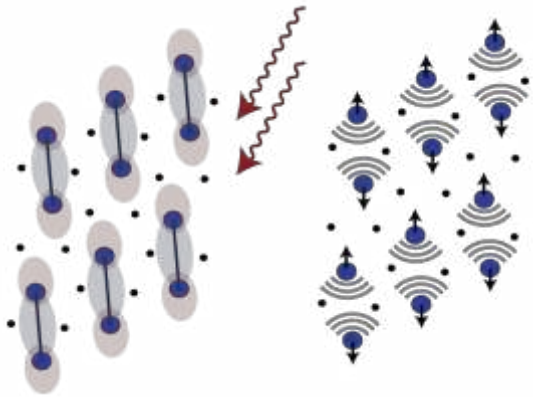

Figure 3.12. Schematic of the lattice response, where a change in the excited state potential energy surface (red: increase, blue: decrease) may trigger impulsive nuclear motion via phonon excitation.

The dynamics observed in this work are consistent with, but establish even faster dynamics than recent femtosecond photoemission (*38*) and transient reflectivity (*39*) results on the IMT in VO_2 that yielded 60 and 40 fs (pulse-duration limited) timescales, respectively. The measurement of a non-pulse-duration-limited 26±6 fs timescale supports a Mott-like mechanism as opposed to Peierls, but does not rule out structural involvement. Electronic and structural effects may indeed be working cooperatively (*103*). A full theoretical description of the dynamics would likely need to incorporate the electron hopping time, or transfer integral, as well as screening to fully capture the role of both energy shifts and bandwidth changes across the phase transition. The observation

of a common non-thermal final state is similar to recent ultrafast pump-probe measurements on the insulating and metallic phases of the prototypical Mott-Hubbard transition in V_2O_3 (*124*). Further elucidation will require more advanced theory, mapping screening and structural distortion effects onto the XUV spectrum - an exciting and tangible possibility.

The time constant measured here is not necessarily a fundamental lower limit on the timescale of the IMT process in VO_2. It may vary and indeed be faster based on sample crystallinity, doping, strain, and starting temperature (*39*, *125*), as well as on the pulse spectrum and energy of the pump beam, which determines the initial spatial and energy distribution of the injected charges. While all of the previous ultrafast experiments on VO_2 (as well as this work) have used Ti:Sapphire laser pulses, the bandwidth and central wavelength of the pulses is varied– however, as most of these results were ultimately limited by the temporal resolution of the experiment, it is not yet possible to map out a trend as to how these factors influence the dynamics. In regards to sample crystallinity, results to date are generally in agreement between single crystal and polycrystalline films: time-resolved electron diffraction has measured structural timescales in agreement (*101*, *102*), and the fastest electronic timescales measured for each case were previously limited by the pulse duration (<60 fs for thin films (*38*), and <40 fs for microrods (*39*)). It may be speculated that excitation closer to the band-edge and in single crystal samples would provide the "natural" speed limit, however, based on this work, dynamics in polycrystalline samples may actually be faster, and more data will be needed to understand this. Broadband XUV attosecond pulses provide access to core-level transitions with unprecedented temporal resolution, making FXTAS a powerful tool to study these effects. For VO_2, it is shown that the IMT occurs within 26±6 fs following a change in orbital occupancy. Together with global analysis and theoretical modeling, this methodology has the potential to disentangle the effects of spin, lattice, and orbital degrees of freedom in other correlation-driven phenomena in condensed matter systems.

3.4 Supporting Information

3.4.1 Sample Characterization

Experiments were carried out on 25 nm thick polycrystalline VO_2 thin films prepared by pulsed laser deposition (*68*) in an Epion PLD-3000 system (base vacuum of $9x10^{-7}$ Torr). A vanadium metal target was ablated at room temperature in an oxygen atmosphere ($1.1x10^{-2}$ Torr maintained by 2 ccm flow) by an excimer laser (248 nm, Lambda Physik Comp-Ex 205, nominal pulse duration 25 ns), at a fluence of 4 J/cm^2 with a pulse repetition rate of 25 Hz. The average deposition rate of the VO_x film was 0.3 Å/s. After deposition, the films were annealed in a tube furnace at 450 ºC for 10 min in 250 mTorr oxygen to produce stoichiometric VO_2. The samples were deposited on 30 nm thick freestanding Si_3N_4 membranes provided by Silson Ltd. The clear membrane and sample area was 3 mm x 3 mm, and the membrane was supported on a silicon frame of dimensions 7.5 mm x 7.5 mm.

The VO_2 films were characterized via Raman spectroscopy, as shown in panel A of Figure 3.13. Spectra were taken in a Raman microscope in a backscattered geometry at 532 nm and 1.0 mW power. Spectra were taken over the silicon frame as opposed to the freestanding area to collect sufficient reflected light. Reference spectra were taken for a silicon nitride substrate and subtracted

from the final VO_2 signal. All of the peaks in the Raman spectrum are well matched to previous measurements (*39*, *126–128*). The thermal phase transition in the samples was characterized by heating and cooling the sample and measuring the transmission of a HeNe laser beam onto a photodiode, yielding the hysteresis curve shown in Figure 3.13B. It should be noted that the optical hysteresis curve in transmission increases when measured at 633 nm, unlike the typical IR transmission; this is because the imaginary part of the dielectric function decreases in the UV-VIS across the phase transition, while it increases for wavelengths in the IR and beyond. The IMT was observed at 69 ºC and the observed hysteresis was 6 ºC wide, as quantified by the difference in temperature between the heating and cooling curves at their half maximum transmission value. Hysteresis width in VO_2 generally increases with smaller nanocrystal domain sizes, with a minimum in the bulk crystal of ~1 ºC to values up to 10-15 ºC in polycrystalline thin films (*63*, *128*). The relatively sharp hysteresis observed here indicates a high-quality film. Early studies of vanadium dioxide nanoparticles and thin films showed that size- and thickness-dependent optical contrast between the semiconducting and metallic states of VO_2 is strongly associated with the proper 1:2 stoichiometry (*129*). Moreover, optical studies of single-grain and multiple-grain vanadium dioxide nanoparticles and thin films also show a clear dependence of hysteresis width on nanoparticle or thin-film grain dimensions (*130*). From comparison to previous literature (*131*), which characterized hysteresis width as a function of grain size for polycrystalline VO_2 films (also on silicon nitride substrates), it can be expected that grain sizes are on the order of 25 nm, however domain sizes were not measured directly in this work. As the crystallites are randomly oriented no sample orientation dependence is observed with respect to the laser polarization in either the static XUV spectrum or dynamics, and measure an average over all orientations.

Sample switching was checked in vacuum using a quartz halogen lamp, where it was confirmed that the phase transition boundary had been crossed by observing an abrupt jump in the change in transmission of the NIR light (see back to Figure 3.5), similar to what was observed at 633 nm.

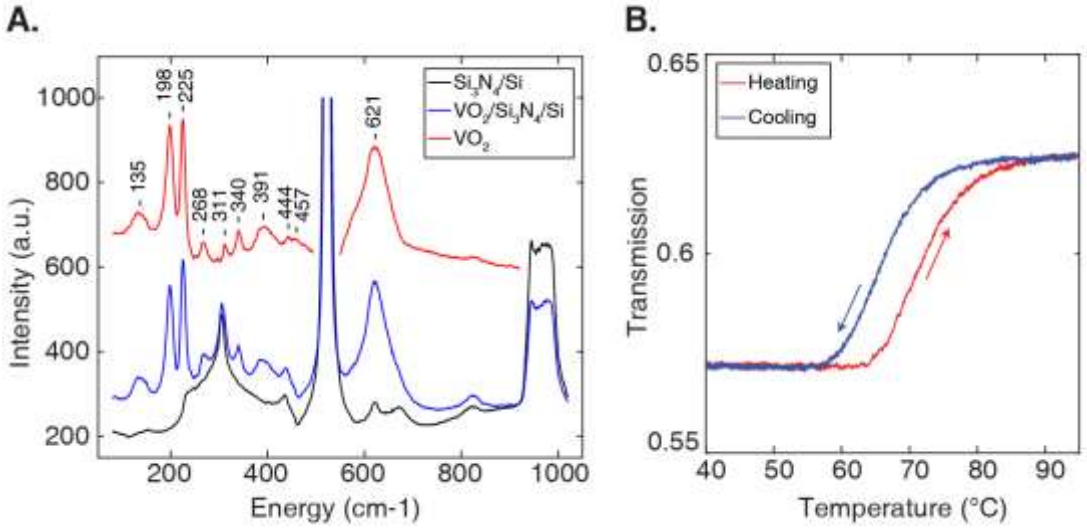

Figure 3.13: (**A**) Raman spectrum of a VO_2 sample (25 nm VO_2 on 30 nm Si_3N_4 on a silicon frame) and reference substrate (30 nm Si_3N_4 on a silicon frame). The VO_2 signal is obtained by subtracting the reference spectrum from the sample spectrum. Regions where the strong Si and

SiO_2 peaks dominate have been removed for clarity. (**B**) Hysteresis curve for VO_2 showing the transmission of 633 nm light from a HeNe laser through a 25 nm thin-film sample.

3.4.2 in Situ Pulse Characterization

Neon transient absorption measurements are performed on the neon $2s^12p^6np$ ($n = 3,4,5\ldots$) Rydberg series of XUV-excited inner-valence transitions, spanning from the 3p line at 45.5 eV to the $2s^1$ ionization threshold at 48.4 eV (*105*). Transient measurements probe the perturbation of these lines due to the presence of an overlapping and time-delayed femtosecond NIR pulse. Following the excitation with the XUV pulse, the NIR pulse can cause several effects. One dominant effect is a phase shift of the emitted XUV dipole radiation due to a transient Stark shift of the Rydberg level that results in a Lorentzian-to-Fano (*132*) type line shape change. The time-delayed NIR pulse, through non-resonant and resonant coupling mechanisms, i.e., dipole-allowed transitions to nearby levels, alters the emitted XUV dipole radiation, resulting in hyperbolic sidebands flanking the line. Furthermore, persistent oscillatory effects versus time show up if a coherent wavepacket can be launched. The analysis here focuses on the 4p line at 47.1 eV, since the resonant coupling to other states is suppressed (cf. the NIR ~1.6 eV photon energy). The non-resonant ponderomotive-type couplings with the NIR dominate the observed modifications of the line shape, while still retaining a sufficiently high signal-to-noise ratio of the observed spectral changes across this state. It is in this regime that the experimental pulse geometry can be characterized directly from the transient absorption data, as was previously demonstrated for a helium target (*67*).

Transient absorption modifications of the neon $2s^12p^64p$ line are shown in Figure 3.14. The data display the average of ~300 scans taken *between* each VO_2 scan over a 48 hour period, synchronized in time in the same way as for the VO_2 scans, as described in section 3.4.3. The line shape is fit as a function of time delay, as shown in the second panel of Figure 3.14, which fully captures the observed dynamics. The model includes and quantifies the NIR-laser-induced phase change of the XUV dipole response at arbitrary delay times directly from the absorption data, leading to an *in-situ* determination of the instrument temporal response function as described in reference (*67*). Most importantly, both line shape asymmetry effects and hyperbolic sidebands are included and accounted for in this model.

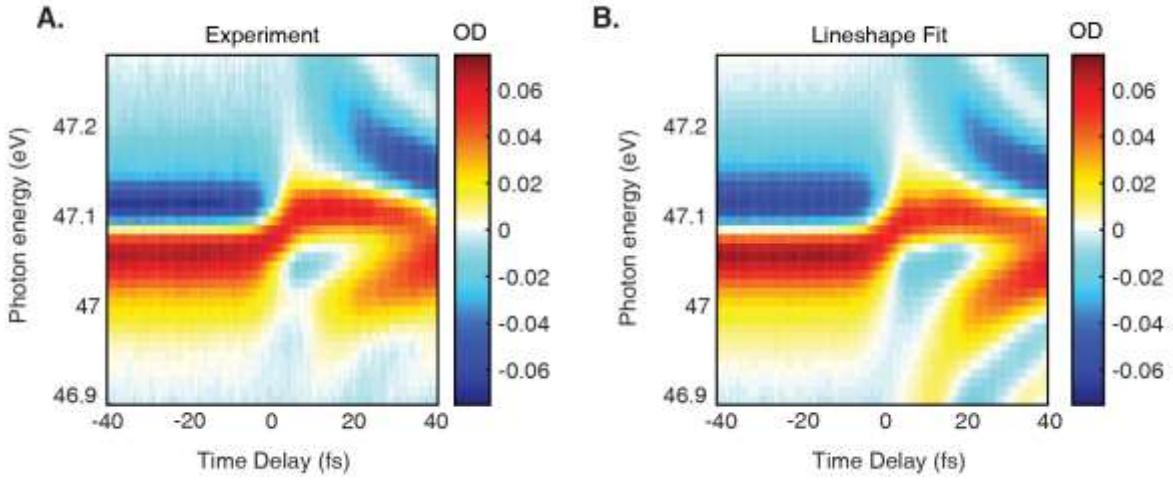

Figure 3.14: Transient absorption across the neon $2s^1 2p^6 4p$ line, measured *in situ* during the VO_2 experiment. The measured data is shown in (**A**), where all scans have been synchronized in time and averaged together, as described in section 3.4.3. The line shape fit is shown in (**B**), showing excellent agreement.

The first derivative of the retrieved phase as a function of time delay is directly proportional to the NIR-induced transient energy shift of the $2s^1 2p^6 4p$ state, which therefore gives direct access to the NIR pulse shape, convoluted with the duration of the XUV excitation, yielding the instrument response function. The result is shown in Figure 3.15. For the insulating phase and metallic phase measurements, values of 5.6±0.8 fs and 7.0±0.8 fs full width at half maximum pulse widths are obtained, respectively. The shape very closely matches the form of the NIR pulse measured via a dispersion scan (see Figure 3.3), including the small post-pulse at +10 fs, with a weak additional broadening due to the XUV attosecond pulse train. No additional effects of the pulse train other than this broadening of the instrument response function have been observed.

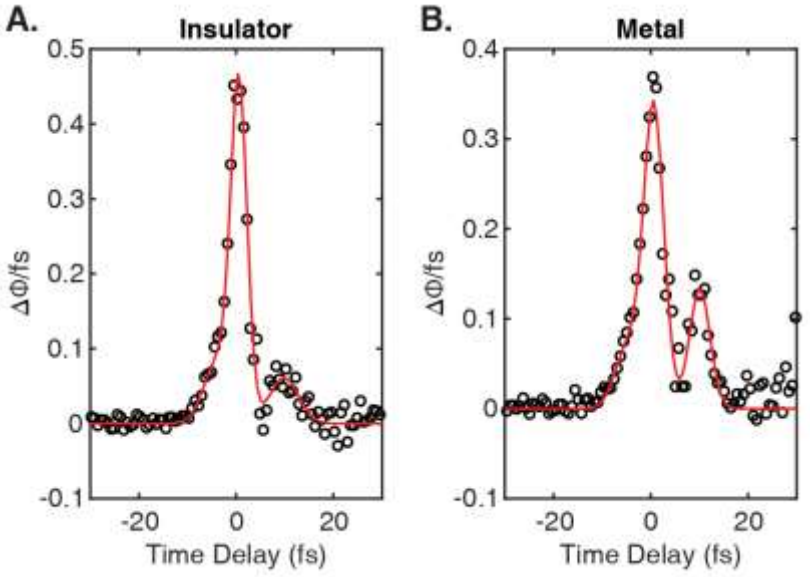

Figure 3.15: The derivative of the phase extracted from the neon line shape fit for the insulating (**A**) and metallic phase (**B**) measurement datasets, yielding an *in situ* characterization of the instrument response function. The change in phase of the Fano line shape due to the perturbation of the XUV-induced dipole by the NIR pulse is fit versus time delay with a sum of three Gaussians, which are plotted as a guide to the eye. The full widths at half maximum of the two datasets are found to be 5.6±0.8 fs and 7.0±0.8 fs, respectively.

3.4.3 Data Analysis and Fitting Methods

Static and transient absorption spectra of both VO_2 and neon were Fourier filtered to remove residual periodicity of the individual harmonics in the spectrum from being imprinted on the data. A narrowband notch filter was used to remove frequency components between 0.54 and 0.97 fs^{-1}, where the high harmonic periodicity appeared. Absorption spectra were calculated via Beer's law, by taking the negative logarithm of sample signal divided by reference signal for static spectra and the negative logarithm of pump-on signal divided by pump-off signal for difference spectra.

In order to synchronize all scans in time and account for any interferometric drifts between pump and probe arm, the neon data were analyzed for each scan by taking a lineout over the positive part of the $2s^1 2p^6 4p$ transition line ranging from 47.10 to 47.15 eV. The reference time-point was taken for each scan to be the maximum of the derivative (ΔOD/fs) over this lineout. Using this reference point, the time delay drift between subsequent VO_2 scans could be determined. The time-delay drift as a function of the elapsed time within the experiment was fit to a spline function, and the time delay axis for the VO_2 scans was then corrected based on the time of day of the recorded scan. All VO_2 scans were then interpolated onto a common time-delay axis and averaged together to create the 2D plots in Figures 3.8A and B of the main text. The same was done with all of the neon scans to provide high-quality data for the retrieval of the instrumental response function as described in the previous section (3.4.2).

Global fitting of the 2D transient absorption maps for VO_2 was performed using the software GLOTARAN 1.5.1. Two spectral components were found for both the insulating and metallic phase corresponding to an initial and final state, where the initial state grows in during the excitation, characterized by the instrument response function, and decays exponentially with a time constant τ to populate the final state. The functional forms are shown below, where $S_1(E)$ and $S_2(E)$ describe the spectral functions of component 1 and component 2, respectively, and $K_1(t)$ and $K_2(t)$ describe the kinetic functions. $S_1(E)$, $S_2(E)$, and τ are all determined from a global fit, where the temporal spread σ and the zero-delay reference t_0 are independently determined via the instrument response function as measured in neon (section 3.4.2). The energy- and delay-dependent functions for the two components $C_1(E,t)$ and $C_2(E,t)$, respectively, are then evaluated as:

$$C_1(E,t) = S_1(E) \otimes K_1(t) \qquad \text{Eqn. 3.1}$$

and

$$C_2(E,t) = S_2(E) \otimes K_2(t), \qquad \text{Eqn. 3.2}$$

where "⊗" denotes the tensor product, and the kinetic functions are given as

$$K_1(t) = \left[\frac{1}{\sigma\sqrt{2\pi}} e^{-\frac{1}{2}\left(\frac{t-t_0}{\sigma}\right)^2} \right] * \left[\left(1 - e^{-\frac{t-t_0}{\tau}} \right) \times \theta(t-t_0) \right] \quad \text{Eqn. 3.3}$$

and

$$K_2(t) = \left[\frac{1}{\sigma\sqrt{2\pi}} e^{-\frac{1}{2}\left(\frac{t-t_0}{\sigma}\right)^2} \right] * \left[e^{-\frac{t-t_0}{\tau}} \times \theta(t-t_0) \right], \quad \text{Eqn. 3.4}$$

with "∗" denoting the convolution with the instrument response function. The final 2D fit is given by the sum of $C_1(E,t)$ and $C_2(E,t)$, where the amplitude is equal to the change in absorbance (ΔOD) at each point in energy and time. As a check of the fit quality, the spectrum at each time delay point is fit to a superposition of $S_1(E)$ and $S_2(E)$, and the resulting amplitudes are plotted alongside the kinetic curves $K_1(t)$ and $K_2(t)$ in Figure 3.9 of the main text, showing good agreement. The changes in ΔOD are a complex function of the modified valence band structure, the change in screening of the core hole due to free carriers, and state opening and blocking effects, which requires a higher level of theory to disentangle. The 2-component fit yields a 69±11 fs timescale for the metallic phase of VO_2 and a 26±6 fs timescale for the insulating phase, both providing good agreement with experiment, as shown in Figure 3.8 of the main text.

Given the common final state of the insulating phase and metallic phase following photoexcitation, an attempt was also made to use the spectral components obtained from the metallic phase data to fit the insulating phase, in order to separate the carrier thermalization and phase transition processes. This model assumes three spectral components, one corresponding to the initial excitation (from the metallic phase), one corresponding to the hot carrier thermalization process (from the metallic phase), and one corresponding to the insulator-to-metal phase transition. The phase-transition component was obtained iteratively by fitting each time point in the insulating-phase data to a superposition of the two metallic phase components and adding the residual signal into a third phase-transition component. The obtained phase-transition spectral signature from the time-resolved data matches very closely with the phase-transition signature measured by heating, as shown in Figure 3.16. The initial and final components from the metallic phase that were used can be found in Figure 3.9A of the main text. The final fit amplitudes and the resulting global fit are shown in panels 16B and C, respectively, where the amplitudes have been fit to equations of the form of Equations 3.3 and 3.4.

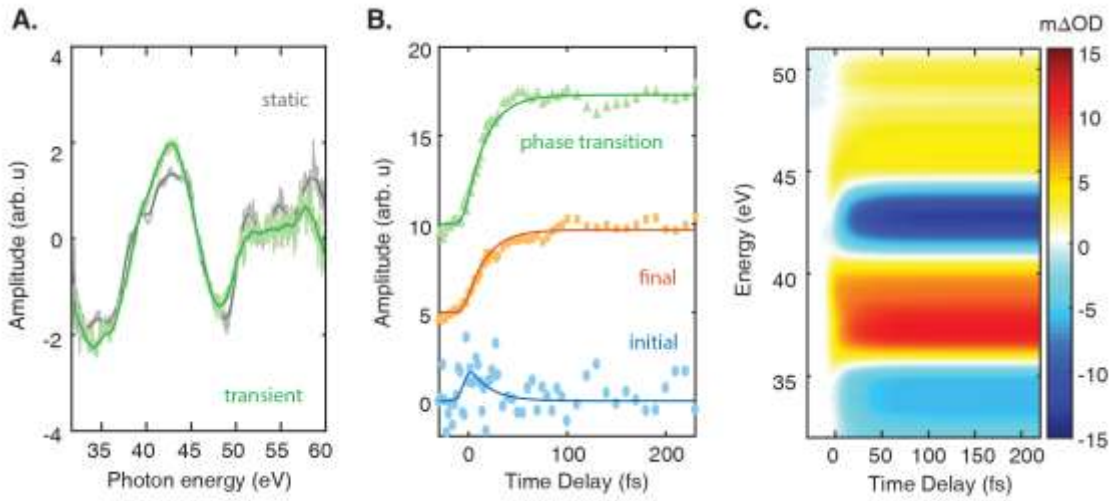

Figure 3.16: Results of the three component fit on the insulating phase VO_2 data, using the initial and final components from the metallic phase data (see Figure 3.9A, main text) and an additional phase transition component shown in green in (**A**), alongside the measured changes to the static spectrum upon heating, for reference. (**B**) The amplitudes of each component as a function of time delay, fit with a 28±8 fs rise and decay. (**C**) The resulting global fit.

Using this model, it is found that only one timescale governs the dynamics, 28±8 fs, compatible with the 26±11 fs timescale obtained with the two-component fit in the main text. The two-component model provides a better fit, as the metallic-phase early-time component does not match the insulating-phase initial response as well. The results are not significantly changed by using the early time signature from the insulating phase two-component fit in the three-component model. There is no evidence of a 69±11 fs timescale present in the response of the insulating phase, in contrast to the metal, however thermalization of carriers must surely also be taking place. This result is likely because of the different character of the excitation in the two systems, given the different band structures. Another possible explanation is competitive kinetics, where the thermalization and phase transition are both drawing excess energy from the same hot electron bath, causing a faster depletion and an apparent common timescale in the insulating phase.

3.4.4 Fluence Dependence

Fluence-dependence measurements at ±100 fs (when insulating state response was no longer evolving) were performed for fluences of 2.9, 3.1, 6.5, 7.3, 7.5, 9.2, 10.8, 13.1, 16.9, 22.3, 24.2, 25.3, and 32.8 mJ/cm^2, in a pump-on / pump-of scheme. A power measurement was taken by picking the beam off before the sample (calibrated for any losses between the pickoff mirror and power meter head), and an image of the pump beam profile at the focus was saved for each measurement, in order to ensure that the size and shape of the beam profile did not change. Due to the very low ΔOD values a full transient measurement could not be performed for each fluence within a reasonable time for data acquisition, although a fluence dependence study of the dynamics would certainly be illuminating.

The resulting ΔOD spectrum for each fluence at +100 fs is shown in Figure 3.17. Each ΔOD spectrum is fit with the final state spectrum of the insulating phase (main text, Figure 3.9C), and the resulting fit amplitudes as a function of fluence are shown in panel B. The results show a threshold fluence at ~3 mJ/cm^2 and saturation setting in around 13 mJ/cm^2. These two classic characteristics of the phase transition, well documented for time-resolved studies on VO_2 throughout the literature (*37*, *40*, *79*, *133*), confirm that the signal observed in the time-resolved studies is indeed the insulator-to-metal phase transition. The ratio of threshold fluence to saturation fluence is ~1:4, consistent with the data noted by Wegkamp et al. (*40*). Systematic uncertainties in the determination of the absolute NIR intensity, as well as the broadband spectral distribution of the pump wavelengths, are most likely responsible for the remaining deviation on the absolute intensity scale.

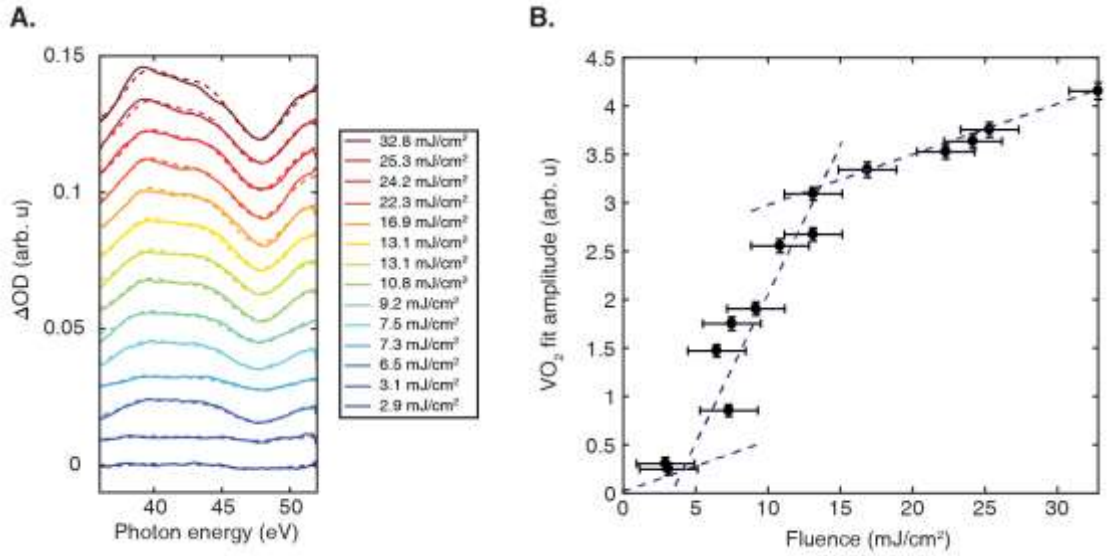

Figure 3.17: Intensity dependence data for VO_2 at +100 fs time delay. (**A**) The measured ΔOD change at each fluence, fit with the final state component of the insulating phase global fit. (***B***) The amplitude of the fit coefficient as a function of fluence, showing clear saturation of the effect as the fluence is raised. The blue dashed lines are shown as a guide to the eye.

Chapter 4.

Optical Design of an Endstation for Attosecond-Pump Attosecond-Probe Experiments

4.1 Introduction to the Project

In this chapter, an endstation is described that was designed and built as part of a large-scale collaboration between the groups of Stephen Leone and Daniel Neumark at UC Berkeley, the group of Zenghu Chang at University of Central Florida, and the groups of Paul Corkum and François Légaré at University of Ottawa and INRS, respectively. The goal of the project is to develop the first-ever tabletop apparatus to perform attosecond-pump attosecond-probe measurements, with a focus on few- and sub-femtosecond dynamics that can occur in solids as a result of electron correlation. Such experiments will help provide a new understanding of the instantaneous response of materials to high-energy extreme ultraviolet (XUV) radiation by following the core-hole decay process and the subsequent correlation- and screening-driven electron dynamics in real time.

The following sections will go over the required capabilities and an optic-by-optic overview of the endstation system. Some emphasis is placed on potential pitfalls and alternative solutions that will hopefully serve as a useful resource for the graduate students and postdoctoral scholars that are currently and will in the future be working on this apparatus – this is not intended to take away from the current design, but rather to provide avenues for possible future enhancements.

4.1.1 Motivation and Project Goals

Because of the low conversion efficiency of the high-harmonic generation (HHG) process, attosecond pulse energies are typically on the order of a few tens of picojoules, and even few-nanojoule energies in the target region are considered high-energy (*134*, *135*). Thus experiments utilizing attosecond pulses to date have typically been accomplished with an attosecond pulse only as the probe or for initial excitation, and a more intense near-infrared (NIR) pulse has been used either as a pump to induce the dynamics or a probe to perturb the result of the attosecond excitation. Sub-femtosecond strong-field processes can be followed in this way by tracking changes that are synchronized to the electric field cycles of the NIR pulse, and resulting phenomena such as time-delays in electron photoemission from different core levels can be measured with few-attosecond precision (*21*). However, following dynamics on the attosecond timescale in the absence of an overlapping field has to date not been possible. Accessing this regime would allow for the study of fundamental processes such as Auger decays of core-excited atoms, interatomic Coulomb decay

in molecules and solids, core-hole screening (with timescales on the order of the material's plasma frequency), and other electron-correlation-driven phenomena. Such experiments will require attosecond pump pulses with orders of magnitude higher energy than the picojoule sources typically used.

Toward this end, the group of Zenghu Chang at University of Central Florida has constructed a Joule-level femtosecond laser system for generating isolated attosecond pulses with energies up to 1 μJ. The energy of attosecond pulses produced via HHG cannot easily be scaled up simply by increasing the focused intensity of the generation beam, as losses from ionization of the target gas rapidly deplete the number of atoms that can participate in HHG. Thus the objective of Chang's group is to scale up the pulse energy and focal size in tandem, also maintaining phase matching conditions. Carrier-envelope phase (CEP) stabilized driving pulses of ~15 fs duration and 3 J pulse energy are to be produced using a home built 10 Hz Ti:Sapphire-based chirped pulse amplification (CPA) laser system. Generalized double optical gating (GDOG) (*136*), a combination of polarization and two-color gating (see Chapter 1.1.2), can then be used to generate isolated attosecond pulses from this driving field. The group has already demonstrated this scheme with 200 mJ NIR driving pulse energies to achieve ~100 nJ isolated attosecond XUV pulses following the HHG interaction region in argon gas (*137*). Using the 3 J NIR driving laser they expect to scale the XUV pulse energy up to 1 μJ. The bulk of the residual NIR light following the HHG process will then be removed by reflections on high damage threshold silicon wafers at Brewster's angle or dielectric mirrors.

The endstation, which will be used to manipulate these attosecond pulses for experiments, has been developed in this thesis at UC Berkeley. It is configured for: separating the source into a pump and probe pulse (with variable attosecond time delays between them), focusing the pump pulse to high intensity in the target region, measuring the XUV spectrum, and providing an array of diagnostics on the pulse energy, duration, beam overlap, and spot sizes at the target focus. The optical layout designed to achieve this is described in the remaining sections of this chapter. The vacuum system construction, diagnostics, and preliminary testing are described in Chapter 5. A schematic of the final apparatus, including both the University of Central Florida laser system and UC Berkeley endstation, is shown in Figure 4.1, with a human figure for scale.

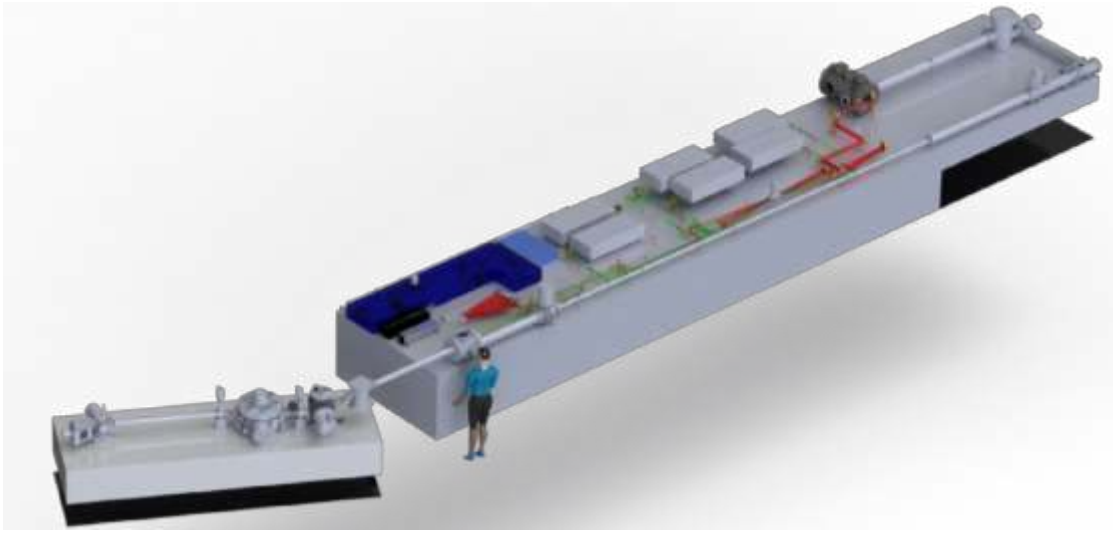

Figure 4.1. CAD design of the attosecond-pump attosecond-probe spectroscopy apparatus. The University of Central Florida laser system is assembled on the larger optical tables in the upper right, with multiple amplification stages. The UC Berkeley endstation is shown on the table in the lower left.

As another part of the collaboration, the groups of Paul Corkum and François Légaré are developing a frequency-domain optical parametric amplification (FOPA) system (*138*) that will produce 1.8 μm few-cycle pulses and allow for the generation of x-ray probe pulses. While the FOPA will eventually be combined with the apparatus in Figure 4.1, it is not shown at this time and will not be described in this dissertation.

4.2 Required Capabilities and Overview of Optical Elements

4.2.1 Required Capabilities

For performing attosecond-pump attosecond-probe experiments, a temporal stability of <200 as jitter in time delay (on the order of the pulse duration) is desired, and diagnostics should be in place to measure the pulse energy, measure the focal spot size, check pump-probe spatial overlap, measure the pulse duration, and acquire the pulse spectrum. However, by far the largest challenge is achieving sufficient intensity of XUV light in the sample region to induce dynamics in the types of samples of interest.

The insulator-to-metal transition (IMT) in vanadium dioxide was considered as a benchmark for the type of experiment of interest, and was used as a starting point to calculate a target intensity for a proposed experiment. As calculated in Chapter 1.3.3, according to the Mott criterion, the free carrier density that must be excited to induce the IMT in VO_2 is $N_e \cong 1.27 \times 10^{20}$ per cm^3, corresponding to ~0.4% of vanadium atoms excited. From the XUV static absorption measurements in Chapter 3, an absorption coefficient of $\mu = 0.07$ nm^{-1} at 50 eV (peak of the $M_{2,3}$ edge, tailored to studying dynamics at and above the vanadium edge onset at 39 eV (*107*)) can be estimated. We can use this required carrier density and absorption coefficient to estimate the number of XUV photons needed. In reality, due to Auger processes and shake up excitations, the

number of generated free carriers due to the XUV pump pulse will rapidly exceed the number of initially absorbed photons. However, this number provides a good upper estimate to the required intensity. Based on the number of absorbed photons per unit area ($\Phi_0 - \Phi$, incident minus transmitted flux), the required incident photon flux is approximately equal to $\Phi_0 = N_e l * (1 - \mathrm{e}^{-\mu l})^{-1}$ If we assume the same sample thickness of $l = 25$ nm, allowing good XUV transmission, then Φ_0 = 3.84 x 10^{14} photons / cm^2. Assuming a central XUV photon energy of 50 eV the required energy density is 3.08 mJ/cm^2. To be even more conservative a factor of 10 higher can be aimed for, which corresponds to roughly 31 mJ/cm^2. We can then set the condition

$$\frac{E_{XUV}}{\pi\left(\frac{d_{FWHM}}{2}\right)^2} \geq 31\frac{\mathrm{mJ}}{\mathrm{cm}^2}, \qquad \text{Equation 4.1}$$

where, for example, with a full-width at half-maximum (FWHM) diameter d_{FWHM} of 10 µm, a pulse energy E_{XUV} of $\geq$ 24 nJ *on target* would be required. For a 200 as pulse, this energy density corresponds to an intensity of ~1.5 x 10^{14} W/cm^2.

4.2.2 Overview of Optical Layout

The first thing that must be done following HHG is removal of the residual NIR pump beam. To accomplish this, two high-damage-threshold silicon plates at Brewster's angle were planned to be used as output couplers, to remove any of the generation beam that has either horizontal or vertical polarization components. Brewster's angle for the NIR wavelength (central wavelength ~780 nm) on silicon is 15 degrees, which corresponds to an XUV reflectivity of ~60% at 50 eV, and falls off rapidly at higher energies. The vertical reflection will result in a beam propagating at a 30 degree downward angle. This angle must then be corrected, which will be done with a split mirror to introduce a time delay, minimizing the total number of reflections. The split mirror will be gold coated, which also results in 60% reflectivity at 50 eV. Additional aluminum or other thin metal filters will then be used to remove any residual NIR light. The transmission of the XUV beam through a 200 nm thick aluminum filter is ~70% at 50 eV. This NIR light removal scheme is shown in Figure 4.2, below, and the split mirror is described in more detail in section 4.3.2. In subsequent work at University of Central Florida (UCF), the silicon plates became damaged by the 800 nm light. Dielectric coated reflectors have sustained operation with 300 mJ of output, but have not been tested with 3 J. While the incidence angles may change slightly based on the dielectric coating the general scheme in Figure 4.2 remains accurate.

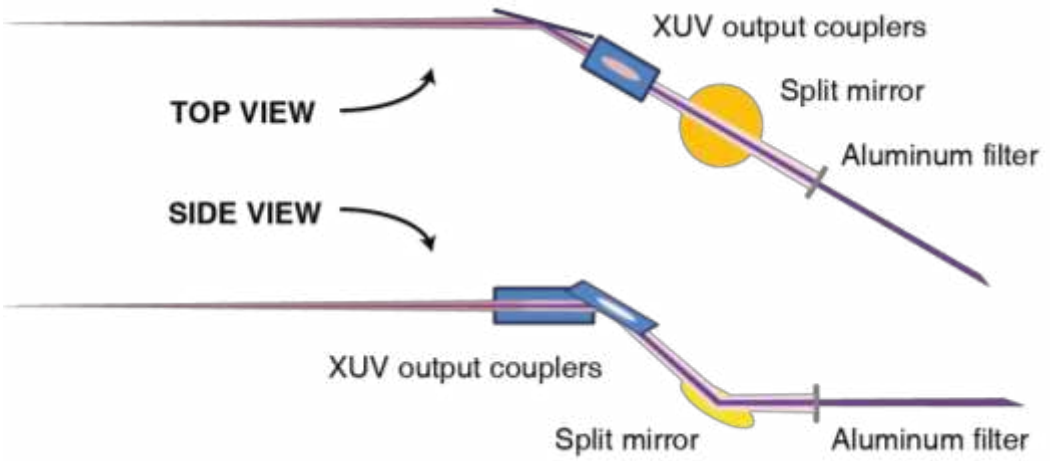

Figure 4.2. NIR light removal scheme, where two silicon plates at Brewster's angle are used as output couplers to remove light from the generation beam of any polarization. Following these reflections the beam is propagating at a downward angle, which will be corrected with a split mirror, and any residual NIR light will be removed using aluminum filters. Figure modified from correspondence with the group of Zenghu Chang.

Following the NIR removal and time delay introduced by the split mirror, the XUV light must be focused through the target area. Based on a tradeoff between the decreasing XUV reflectivity of gold and increasing mirror focusing ability at less grazing incidence angles (described in more detail in section 4.3.3), a 20 degrees grazing incidence ellipsoidal mirror was chosen, which has an XUV reflectivity at 50 eV of 45%. Thus, following all losses (2 silicon wafers, 1 split mirror, 1 aluminum filter, and 1 ellipsoidal mirror) we can expect the XUV pulse energy at the target to be reduced by a factor of ~15 relative to the pulse energy immediately after the HHG region. A 1 µJ pulse energy after the HHG will then correspond to ~132 nJ at the target region. If approximately half of this pulse energy goes into the pump pulse this will be further reduced to ~66 nJ on target. Because of these inherent losses when working with XUV, the ellipsoidal mirror geometry was selected to provide the tightest possible focusing conditions, and the resulting target focus was estimated via ray tracing calculations to have a 1.1 µm FWHM diameter. The calculations will be described optic-by-optic in the following section (4.3). If all of the conditions described here are met, the pump pulse XUV energy density at the focus could reach 870 mJ/cm^2, or ~ 4.3 x 10^{15} W/cm^2 intensity, easily exceeding the target goal. The HHG efficiency is also generally higher for lower energies, and the XUV reflectivity of gold and silicon is as well, meaning the reflection losses on the optics will not be as severe. Attenuation will be easily possible using thicker metal filter combinations, however the high peak intensities that could be accessed may enable groundbreaking studies of nonlinear XUV-matter interactions with attosecond time resolution.

Following the strong focusing through the target region, the resulting highly divergent beam must be refocused into the entrance of the spectrometer. A smaller projection will be used compared to the first ellipsoidal mirror resulting in a ~20 µm FWHM focused beam diameter, which could potentially be used as a second interaction region or diagnostic point in the future. With this beam size and the grating and XUV CCD camera selected, a best-case spectral resolution of ~25 meV at 50 eV may be possible to be achieve. An entrance slit may be additionally introduced if necessary.

An overview of the endstation concept design is illustrated in Figure 4.3, below, and more details and simulations will be provided in the following sections.

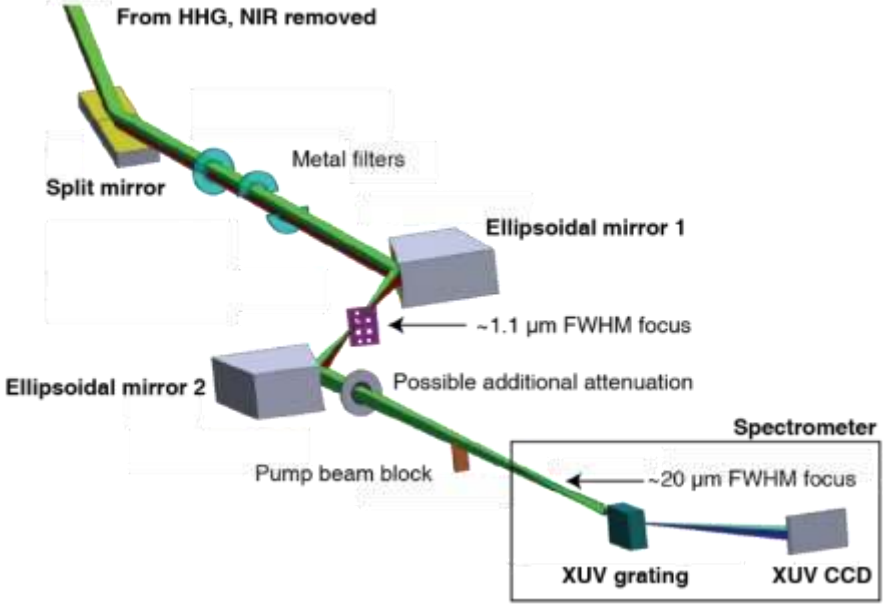

Figure 4.3. Concept design for optical layout of attosecond-pump attosecond-probe endstation. The XUV beam with residual NIR light removed is shown entering from the top left. It undergoes reflection and time-delay on the split mirror, is focused through the target region with the first ellipsoidal mirror. It is refocused into the spectrometer with the second ellipsoidal mirror, where a reflective diffraction grating disperses it onto an XUV CCD camera.

4.3 Ray Tracing Simulations of the Optical Path

4.3.1 Source Condition Estimates

As the endstation and driving laser system were designed and built in parallel, the XUV beam could not be characterized in advance, and some estimates of the beam properties had to be made in order to design the endstation optical layout. Based on the 20 m focal length of the NIR beam into the HHG target and the previous experience at UCF with the 200 mJ / 100 nJ (NIR / XUV) system, the Chang group estimated the XUV pulses would have a beam diameter (FWHM) of 9 mm after 9 m propagation distance, which is approximately where the endstation will be placed. From this starting condition and assuming a central wavelength of 25 nm (50 eV) some further approximations were made. The source conditions that are described here are based on Gaussian beam optics and the definitions in the x-ray tracing code *SHADOW3* (*139*, *140*), which was used to model the optical system. The Gaussian beam definition used in the program is

$$I(x) = I_0 e^{-\frac{x^2}{2\sigma^2}}, \qquad \text{Equation 4.2}$$

where the parameter σ is equal to the $e^{-1/2}$ intensity beam radius, or half of the $1/e^2$ intensity beam radius (ω). It can also be easily shown that $\sigma = d_{FWHM} / \sqrt{2\ln(2)}$. The divergence in the *SHADOW3*

program is defined in the far-field limit as $\theta_\sigma = \arctan(\sigma/z)$, where z is the propagation distance. Thus using our FWHM beam diameter of 9 mm at z = 9 m it can be calculated that $\theta\sigma$ = 425 µrad ($\theta\omega$ = 849 µrad). The other remaining source parameter that must be estimated for the ray tracing calculations is the beam waist. For a 50 eV photon energy and divergence of $\theta\omega$ = 849 µrad, assuming a Gaussian beam, we could use Equation 4.3 to estimate that the $1/e^2$ beam waist (ω_0) should be equal to 9.4 µm, and σ (= 2 ω_0) is thus equal to 4.7 µm.

$$\omega_0 = \frac{\lambda}{\pi\theta_\omega} \qquad \text{Equation 4.3}$$

Using a similar procedure, the NIR beam waist could be calculated based on the 20 m focal length distance, 780 nm wavelength, and 3 cm (FWHM) spot size on the focusing mirror to be ω_0 = 195 µm. However, given the strong 3 J / 15 fs pulses that are being produced, this focusing condition will generate far too high of intensity for HHG, on the order of nearly 10^{17} W/cm^2. In the Chang group's previous work, the condition was set that the NIR intensity should not exceed 10^{15} W/cm^2, which is the ionization saturation intensity for HHG in argon. For their previous 200 mJ / 15 fs pulses, using the same GDOG technique, this condition was met with a ~300 µm FWHM (ω_0 = 353 µm) focal size (*137*). Thus we can extrapolate that since the pulse energy is 15 times higher in this case, the NIR focal size should be √(15) times larger, or roughly 1.2 mm FWHM. With the focusing conditions given by the Chang group this would imply a very non-Gaussian beam (M^2 ~ 6), however as their system includes a deformable mirror to customize the NIR beam wave front, it should be possible to achieve by modifying the beam's spatial distribution. If we assume the same fractional increase in the HHG spot size, the XUV beam waist at the source would then be ω_0 = 65 µm (σ = 28 µm). The x-ray tracing calculations described for each optic in the following sections will thus assume a σ = 28 µm beam size and $\theta\sigma$ = 425 µrad beam divergence as inputs, assuming that the XUV divergence estimate provided is still accurate.

The amount of guesswork in making these kinds of estimates when the source laser has not yet been built is clearly not ideal, however, the optical layout was designed to be accommodating to variations in these parameters. In particular, the ellipsoidal mirror geometry is not sensitive to the beam divergence at all, as long as the beam fits on the mirror surface, and it only depends on the source position, which can be much more easily controlled. The 60:1 projection chosen is strong enough that even in the worst-case scenario of a very large XUV focus (up to ω_0 = 250 µm) due to the strong demagnification the beam waist at the focus can still be < 10 µm if the ellipsoidal mirror is optimally aligned. For all of the calculations shown in the following sections 100,000 random rays were propagated, distributed between six different energy lines at 36.8, 40.0, 43.2, 46.4, 49.6, and 52.8 eV (corresponding to the 23rd, 25th, 27th, 29th, 31st, and 33rd harmonics, respectively, as exemplary of the broadband continuous attosecond output). The general geometry used in *SHADOW3* is illustrated in Figure 4.4, where the image plane of the previous optical element is defined as the source plane of the next optical element. The image plane distance can be varied to probe the beam cross section at various distances following each optic. The image plane of the preceding optic becomes the source plane of the next optic. Thus the distance between adjacent optical elements is equal to the image distance of the first optic plus the source distance of the second.

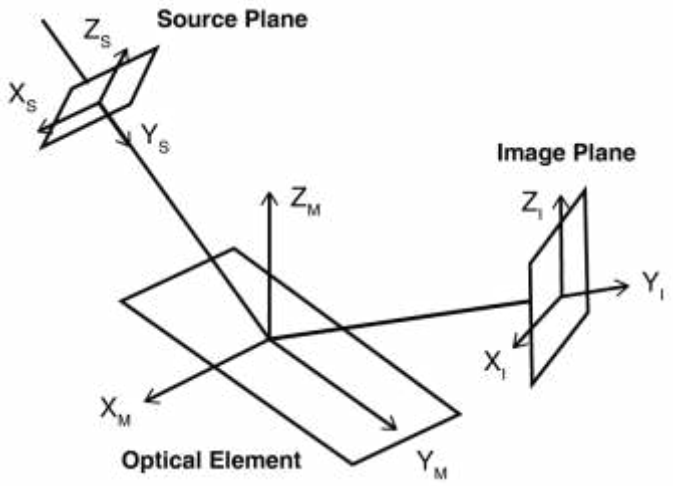

Figure 4.4. Geometry used in ray tracing calculations. The incidence angle on each optical element is defined with respect to its surface normal (*Z*). Figure modified from the *SHADOW3* user manual.

4.3.2 Split Mirror Design

In order to separate the source beam into two pulses, a pump and a probe, a split mirror design is used. One half of the mirror can be retracted with respect to the other, resulting in a different path length for the upper and lower beams. The concept is illustrated in Figure 4.5, below. Such designs have been demonstrated in previous experiments and are an established method for introducing time delays in the XUV (*141–143*). A simple split-in-half design was selected as opposed to a circular mirror with an inner and outer portion because of the simplicity and greater versatility. It can be easily shown in either case that the change in path length as a function of mirror displacement satisfies the Bragg condition, where $\Delta l = 2dsin(\theta)$, and thus $\Delta t = c/(2d\ \sin(\theta))$.

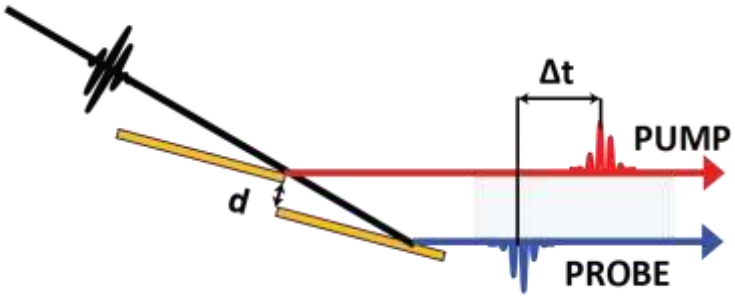

Figure 4.5. Split mirror concept, where upper and lower halves of mirror are offset to introduce a time delay between the two halves of the beam, which will become the pump and probe, respectively.

It is worth noting that at nonzero displacements a shadow is cast on the surface of the lower mirror by the upper mirror, leading to a slight gap between the pump and probe beams. At negative time delays the situation is reversed and part of the reflection from the upper mirror is blocked, leading to slight attenuation of the pump beam. It can be shown geometrically that the width that is shadowed on the mirror surface is equal to $d/\cos(\theta)$ and the resulting gap between the beams is equal to $2d\cos(\theta)$. In the case of a 100 fs displacement and 15 degrees incidence, the size of the

shadow is 60 µm and the resulting gap width is 112 µm. As this gap is on the order of or smaller than the dead region between the mirrors, it will likely not have an impact. However, it is important to be aware of this to ensure that there are no systematic changes in either pump or probe intensity as a function of time delay, which would need to be calibrated for or blocked.

Because the mirror angle must be fixed to 15 degrees grazing incidence in order to correct for the downward angle of the beam from the Brewster's angle output couplers, the size of the mirrors required can be easily determined, given the beam size and divergence conditions described in section 4.2.2. A footprint of the beam on the split mirror is shown in Figure 4.6. The entirety of the beam fits quite well on a 4 x 12 cm surface. Two 5 x 8 cm mirrors were selected to provide some additional buffer space so that the beam could be aligned off center on the mirrors if desired. The surface quality of the mirrors is guaranteed out to the knife edge where the gap will be, and the inner corner of the substrate is machined to a slightly acute angle (~88°) such that the mirrors have more range of angular motion.

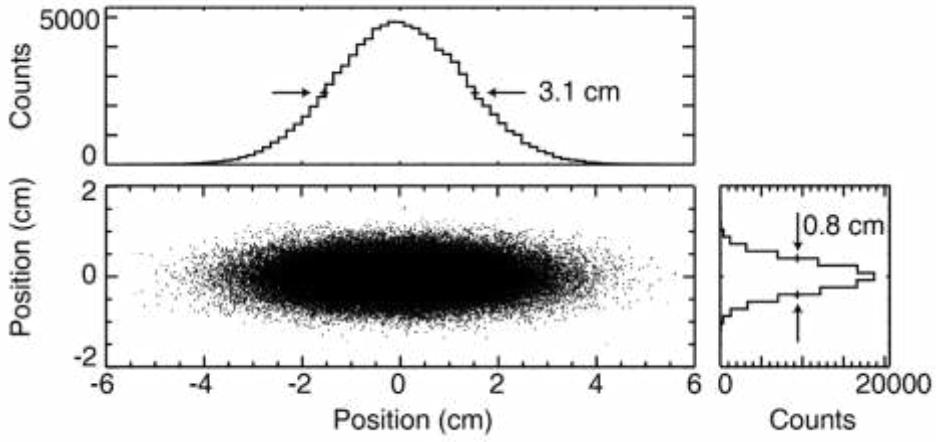

Figure 4.6. Ray tracing simulation of the XUV beam footprint on the split mirror at 15 degrees grazing incidence and a distance of 8 m from the source.

Another aspect to consider is that as a function of split mirror displacement, the ellipsoidal mirror will see a small parallel displacement of the incident probe beam in the vertical direction, which may very slightly change the focusing. If this is significant it is possible that a small relative angle may need to be introduced between the beams in order to ensure perfect pump-probe overlap. The split mirrors are mounted on five-axis picomotor-based alignment stages to ensure such compensation will be possible, although depending on how critical this becomes it may be necessary to replace the stages with a closed-loop motorized mirror mount with absolute and repeatable positioning.

Ray tracing calculations were performed to provide an estimate of this probe beam spatial drift as a function of time delay at the target region, after focusing by the twenty degrees grazing incidence 60:1 projection focusing mirror selected (see section 4.2.3). Calculations were performed at 0 µm and ±58 µm displacement offset, which corresponds to 0 fs and ±100 fs time delay. It is important to note that interference effects and diffraction are not able to be modeled in this software, and thus the beam profiles shown at the focus will not be exactly correct. However, the geometric

effect in terms of how the mirror displacement moves the effective source point, and how this affects the position of the ellipsoidal mirror's focal spot are what is of interest in this case. The results are shown in Figure 4.7, below. It can be clearly seen that the focal displacement over 100 fs time-delay change is approximately 2 µm. It will depend on the final pump beam focal size and uniformity whether this drift is significant and needs to be compensated for.

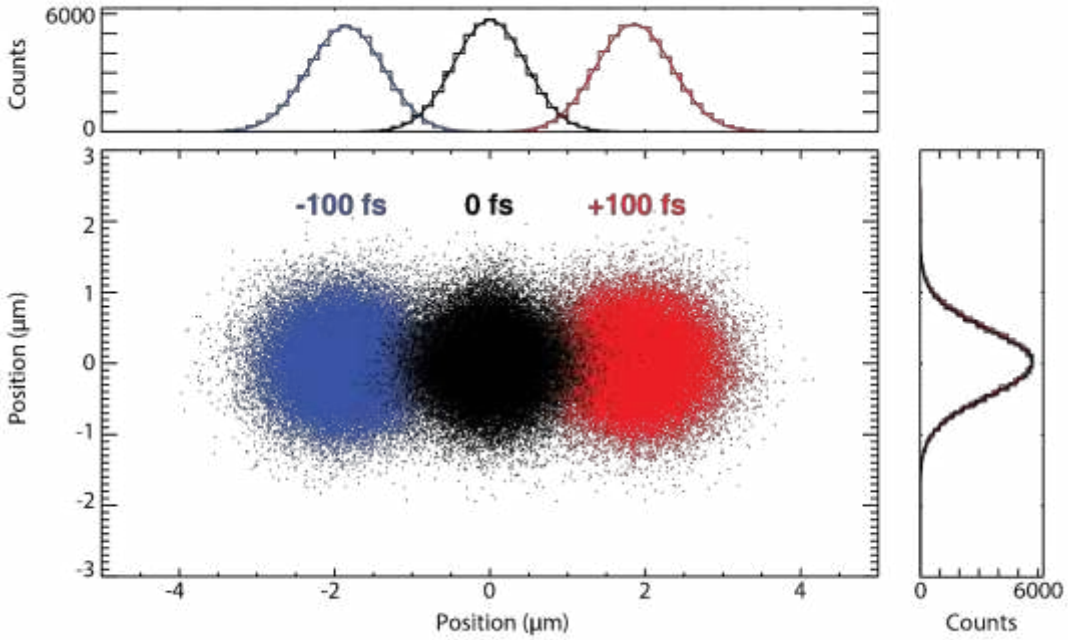

Figure 4.7. The probe beam focus at different split-mirror time delays, shown in the sample plane following the ellipsoidal focusing element. Pump-probe delays of -100 fs, 0 fs, and +100 fs are shown in blue, black, and red, respectively. The vertical dimension in the plots corresponds to the horizontal dimension in the true optical system.

The desired condition is of course that the pump beam focal volume is significantly larger than the probe beam, which can be difficult to achieve when the same focusing element is used for both beams. In the default scenario, the focal volume of each beam will be approximately the same size, the results will be intensity averaged, and the mirror stage position as a function of time delay will likely need to be calibrated to ensure good spatial overlap at each point. However, some techniques can be used to increase the pump volume and achieve the more desired scenario, where these efforts may not be necessary. For instance, by aligning off center on the split mirror and applying an aperture to the upper half of the beam in the far field, the size of the pump beam at the focus will be significantly increased. A schematic of this geometry is shown in Figure 4.8. This will of course result in a loss of pulse energy, another reason that the minimal total reflections and strong focusing are critical, and the probe beam will need to be attenuated. The sharp edges where the pump beam aperture and the split mirror cut into the beam profile will soften as a result of diffraction over the ~ 1 m remaining distance to the focus. While incorporation of these effects is beyond the scope of the ray tracing software used, previous studies of the focusing of a cut-in-half Gaussian beam suggest the probe beam focus will still be relatively uniform and not much larger than the focus of the non-cut-in-half Gaussian mode (*144*). Decisions on the final aperture

dimensions and alignment will be made once preliminary measurements of the XUV beam size at the split mirror can be made.

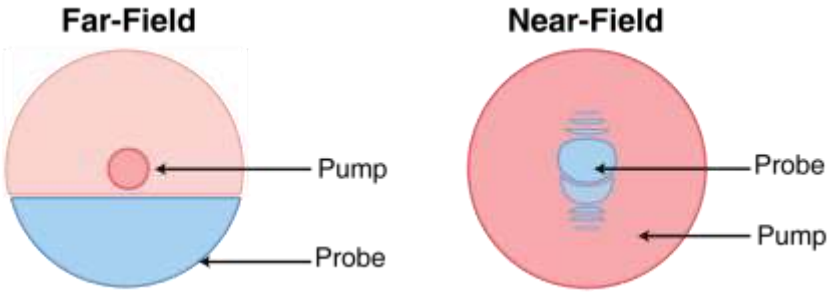

Figure 4.8. Example of beam profiles in the far field that could be focused to achieve the condition that the pump volume > probe volume in the near field. The beam would be aligned off center on the split mirror, and a mask could be used to aperture the pump beam. If need be an angle can be introduced between the split mirror halves to ensure the beams overlap at the focus. The near-field image is a schematic and not a calculation, where the shape of the pump beam is adapted from the focus of a half-Gaussian beam as calculated and measured in Reference (*144*).

4.3.3 Focusing optics: Ellipsoidal Mirrors

Following the split mirror, the beam must be focused into the target region. As already mentioned, for the final apparatus, a 20 degree grazing incidence gold-coated ellipsoidal mirror was selected as the main focusing element. This section outlines some of the considerations that went into this selection.

For focusing light in the XUV, one option is to use grazing incidence focusing elements such as toroidal or ellipsoidal mirrors, or elliptical mirror pairs (Kirpatrick-Baez mirrors), which yield reasonably high reflectivities. Alternatively, in order to use more traditional larger-angle reflective focusing optics such as spherical or parabolic mirrors, a custom multilayer coating for the wavelength region of interest must be applied. While there is a cost advantage for such multilayer coatings the bandwidth is typically on the order of 10-15 eV at most, and even in the optimal energy window the reflectivity is generally lower than for grazing incidence optics. Thus for greater flexibility of the design, it was decided to use a grazing incidence reflective focusing element. The damage thresholds of both types of optics are similar, typically 1-2 J/cm^2 (*145*), which will certainly not be a problem with the source conditions of this apparatus.

Geometrically, the two-dimensional shape that reflects light from one focused point to another with no aberration is an ellipse, as illustrated in Figure 4.9A, because the tangent normal at each point on the surface precisely bisects the angle between the two foci. By rotating the ellipse about the major axis a rotational ellipsoid (prolate spheroid) is generated, which focuses light between the same two foci for a three-dimensional divergent source point, and results in aberration-free focusing. However, in the work described in Chapter 3, and a large fraction of the NIR-pump XUV-probe literature, a toroidal mirror is used instead. The toroidal surface is shown in Figure 4.9B, and it is a good approximation to an ellipsoid when x << y, or when the distance between the two foci is similar, as in a 1:1 or 1:2 projection. The sagittal and tangential radii correspond

approximately to the minor and major radii of the ellipse, and the spherical rotation path of the toroid makes the geometry significantly easier to manufacture. However at larger projections the aberration with toroidal mirrors becomes quite significant, as will be shown.

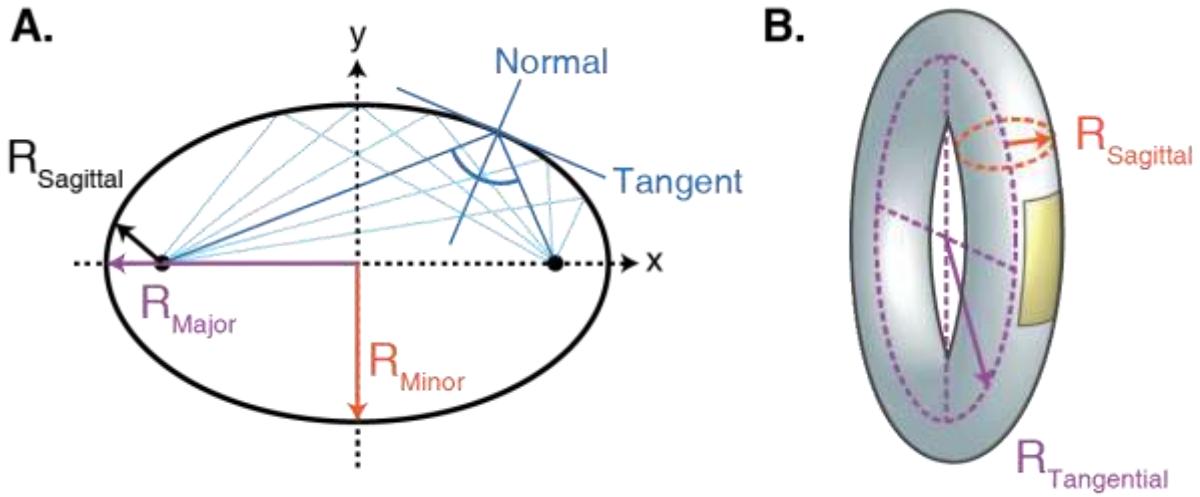

Figure 4.9. Elliptical geometry (**A**), which can be rotated about the major axis to generate a rotational ellipsoid, which focuses rays originating from one focus (the source) perfectly to the other focus (the image). Toroidal geometry (**B**) can be a good approximation to an ellipsoid under certain conditions. The surface that might be manufactured into a mirror is highlighted in gold.

The necessary rotational ellipsoid geometry can be fully defined by the desired distance to each focus and the angle of incidence. However, because of the difficulty of manufacturing aspheric mirrors there are some restrictions on the geometries that can be produced, in terms of the minimum sagittal radius and maximum slope gradients. As a result, the stronger projections ($d_{focus1} >> d_{focus2}$) can only be manufactured at larger incidence angles, leading to a tradeoff between the XUV reflectivity and the strength of focusing. In order to escape such limitations, what is often done at synchrotrons is to use two deformable elliptical mirrors known as a Kirkpatrick-Baez pair, which are used to focus light independently in the vertical and horizontal dimension to the same point, and this can be done under very grazing incidence for high reflectivity. While this would be the most ideal solution, the cost and dimensions required were out of the scope of this project. Because an ellipsoidal mirror is still able to meet the desired intensity requirements for this project, this was the focusing optic chosen.

Given the size of the room that will house the endstation, the position of the focusing element was fixed at 9.0 m from the source, which was as far away as reasonably possible to allow for expansion of the generation beam before the NIR removal. Different projections and incidence angle ellipsoidal mirrors were compared, taking into account also the reflectivity of gold at each angle, in order to decide on a suitable geometry for the focusing. The results are shown in Table 4.1, below, where the intensities are calculated assuming 50 nJ XUV pump pulse energy just before the ellipsoidal mirror. The general trend is clear that the increase in intensity from going to a shorter focal length outweighs the decease due to the reduced reflectivity of gold at the less grazing incidence angles required. This is also convenient as with a less grazing incidence angle, the mirror surface area is not required to be as large, and the manufacturing costs are reduced. Of the

considered conditions, the mirror that resulted in the highest peak energy density that could still be manufactured was selected: a 20 degrees grazing incidence ellipsoidal mirror with a 900 cm source distance and 15 cm focal length (60:1 projection). The simulated focal spot via ray tracing with the source parameters described is shown in Figure 4.10A, below, showing a clean Gaussian profile with no aberration, and 1.1 μm FWHM.

Table 4.1. Focusing comparison for different ellipsoidal mirror geometries, tabulating the spot sizes and estimated peak energy density for different incidence angles and projections. Mirrors that cannot be manufactured are shaded in gray.

Angle (deg.)	**Au reflectivity (50 eV)**		**Focal Length (cm)**		
			22.5 (40:1)	**15 (60:1)**	**10 (90:1)**
5	83%	Spot size (μm)	1.6 x 1.6	1.0 x 1.0	0.6 x 0.6
		Energy density (mJ/cm^2)	520	1300	3700
10	68%	Spot size (μm)	1.6 x 1.6	1.1 x 1.1	0.7 x 0.7
		Energy density (mJ/cm^2)	420	890	2200
15	56%	Spot size (μm)	1.6 x 1.6	1.1 x 1.1	0.7 x 0.7
		Energy density (mJ/cm^2)	350	740	1800
20	45%	Spot size (μm)	1.6 x 1.6	1.1 x 1.1	0.7 x 0.7
		Energy density (mJ/cm^2)	280	590	1500

[3,4]

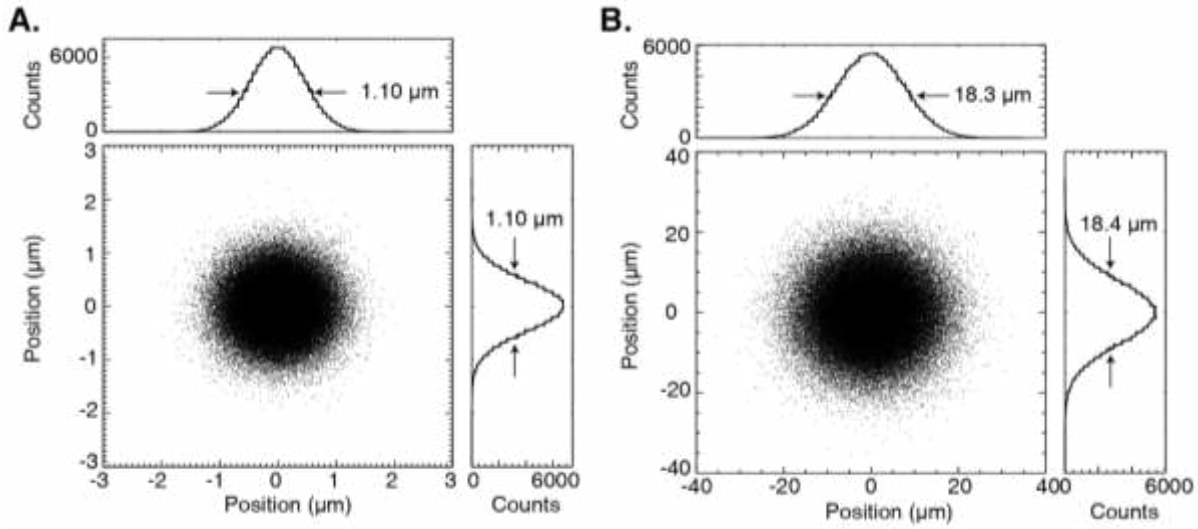

Figure 4.10. (**A**) Simulated focus via ray tracing following the 20 degree grazing incidence 60:1 projection (900 cm to 15 cm) ellipsoidal mirror for focusing into the target region. (**B**) Simulated focus following the second 20 degree grazing incidence ellipsoidal mirror for refocusing into the spectrometer, which has a 15 cm to 250 cm projection.

[3] The mirror conditions shaded in grey cannot be produced by the manufacturer.
[4] The peak energy density of the available mirrors is highlighted in red and corresponds to the mirror selected.

Due to the short focal length used, the XUV beam following the target region will be very divergent. Thus it is necessary to either collimate or refocus the beam into the spectrometer. It was decided to place the second ellipsoidal mirror symmetrically about the focus with respect to the first mirror, at a 15 cm distance from the target and 20 degrees grazing incidence. A 2.5 m refocusing distance was selected, corresponding to a 1:17 projection. These conditions ensure the beam will not be so large as to exceed the mirror clear aperture, and it allows for a long distance over which to propagate, where, for example, a beam block could be put in place to block the XUV pump light. At the second focus the intensity will be lower, and various diagnostics can potentially be placed at this additional interaction region. The simulated focus of this mirror is shown in Figure 4.10B, showing a clean Gaussian profile and 18.4 μm FWHM.

Because the distance and angle with respect to the target is the same for both ellipsoidal mirrors is the same, the beam will have the same footprint size on each mirror, which is shown in Figure 4.11. The FWHM of the dispersed beam is 2.6 cm in the horizontal direction, which corresponds to a $1/e^2$ diameter of 4.4 cm. The vertical dimension shows the expected 9 mm FWHM after 9 m propagation distance, which corresponds to a $1/e^2$ diameter of 1.5 cm. To fit this ~4.4 cm x 0.9 cm beam profile a 5 cm x 3 cm clear polished aperture was chosen (although the mirror substrate as a whole is significantly larger).

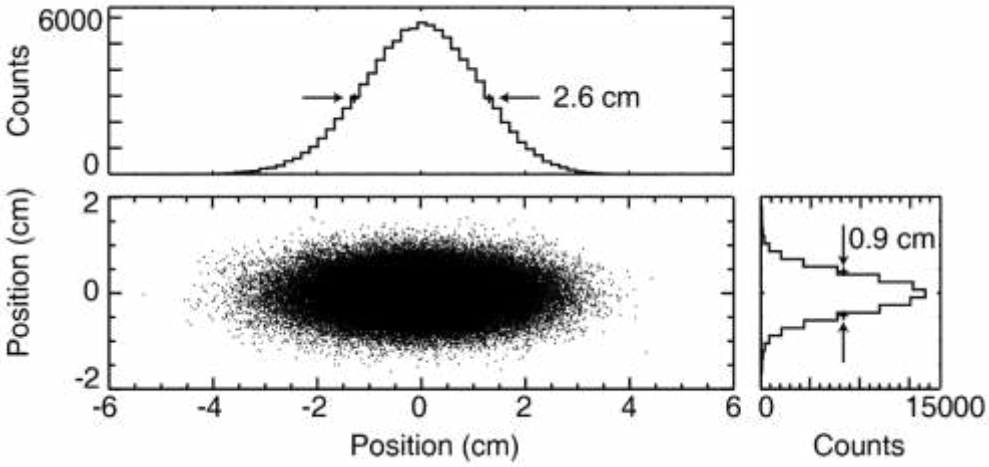

Figure 4.11. Footprint of the beam on the ellipsoidal mirror at 20 degrees grazing incidence at a distance of 9 m from the source (15 cm from the target).

As the second mirror is at a 1:17 projection, as opposed to the 60:1 projection of the first mirror, it was also considered, whether a toroidal mirror could be used in this location. For the toroidal mirrors considered the same source distance of 15 cm from the target was maintained to ensure the beam would not become too large, and the angle of 20 degrees grazing incidence was also maintained such that following the two mirrors the beam would continue parallel to its initial propagation direction. Ideally the refocusing would be done to a lower intensity than the initial focusing into the target region, but a variety of conditions were considered. The cases of 1:1, 1:2, 1:3, 1:5, and 1:10, and 1:15 were all calculated, corresponding to distances of 15 cm, 30 cm, 45 cm, 75 cm, 150 cm, and 225 cm to the second focus. The resulting beam profiles are shown in

Figure 4.12, below, where it is immediately clear that the large degree of aberration will make it impossible to use any of these geometries, even the 1:1 projection.

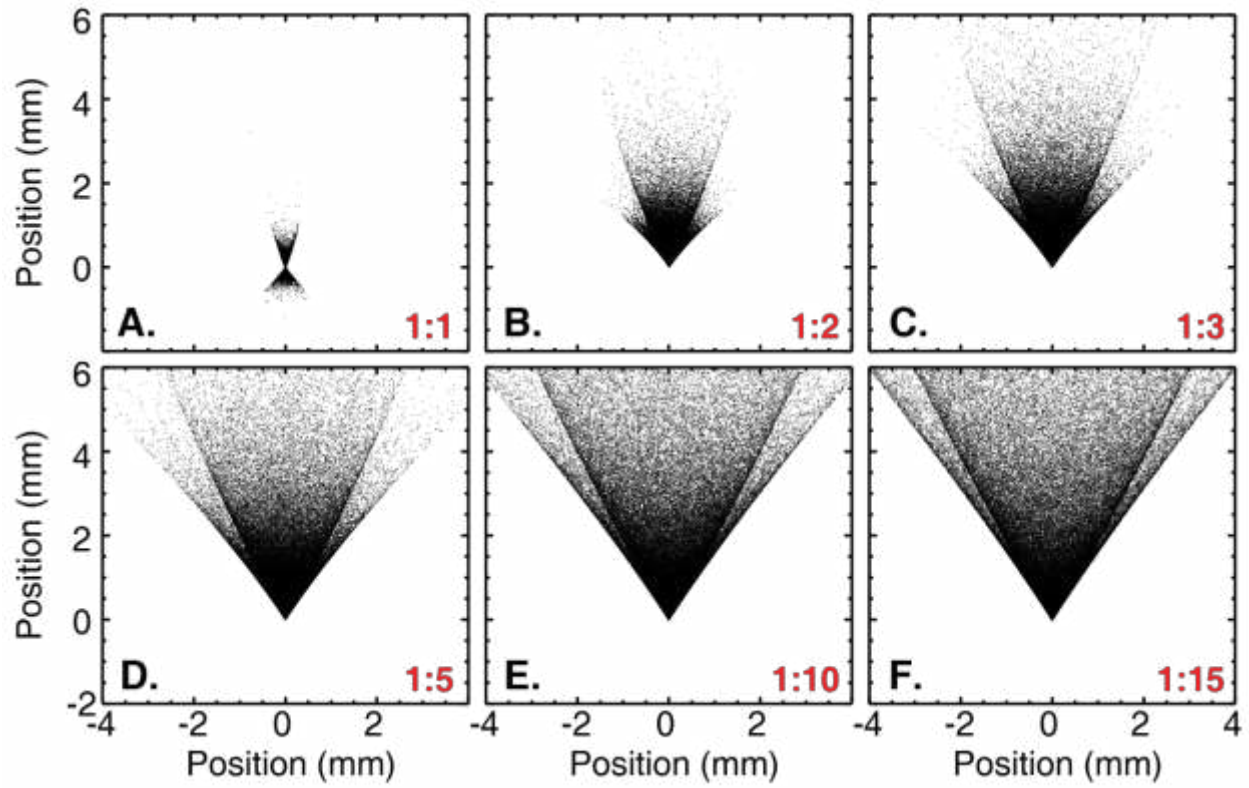

Figure 4.12. The simulated focus following a 20° grazing incidence toroidal mirror at 15 cm distance from the target region, where the projections used in (**A-F**) correspond to a 1:1, 1:2, 1:3, 1:5, 1:10, and 1:15 projection (15 cm, 30 cm, 45 cm, 75 cm, 150 cm, and 225 cm, respectively). The vertical dimension in the plots corresponds to the horizontal dimension in the true optical system.

To see how the beam profile changes between the 1:1 and 1:2 projection, where the qualitative differences are the largest, and to see if there is perhaps an optimum case in between, simulations were also carried out for a 1:1.17 projection (15 cm to 17.5 cm) and a 1:1.33 projection (15 cm to 20 cm). The results, shown in Figure 4.13, show that there does appear to be an optimum, at least in part of the beam profile, visible in the 1:1.17 projection in panel B. However, the overall shape still displays significant aberration, and even this most ideal portion of the beam is significantly larger than the beam size that would be expected for perfect focusing. A close up, shown in the inset, reveals that the beam profile here is still quite distorted. It is worth noting that the aberration is in no way due to the preceding ellipsoidal mirror, as the beam remains perfectly Gaussian following this optic. The results are the same when using the ellipsoidal mirror and using a Gaussian point source with equivalent spot size and divergence. The distortions seen in the beam profile are a manifestation of spherical aberration in the toroidal mirror system, which becomes significant at short focal lengths and when a large fraction of the mirror surface is illuminated. Thus a toroidal mirror is clearly not appropriate for such divergent beam conditions.

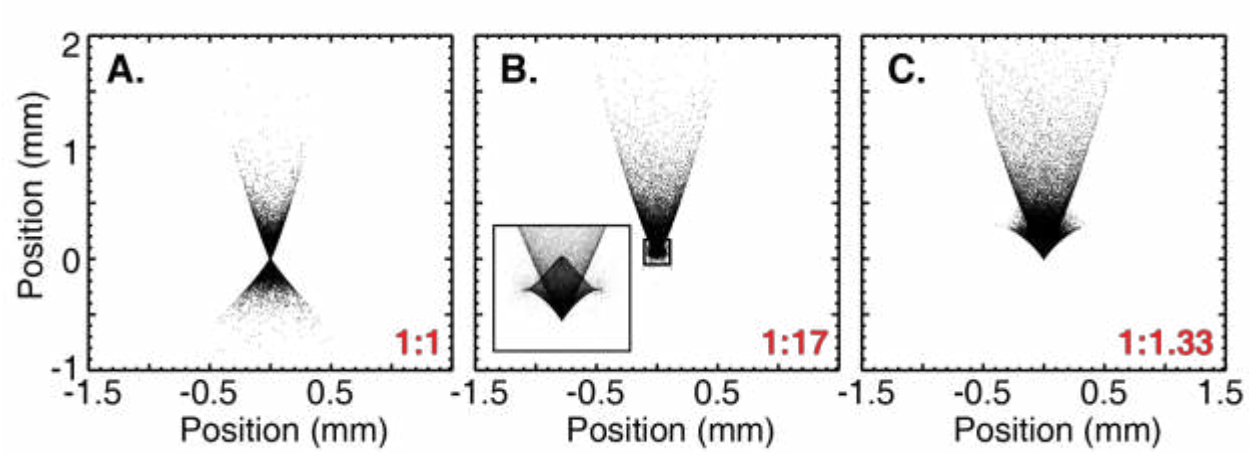

Figure 4.13. The simulated focus of a 20° grazing incidence toroidal mirror at 15 cm distance from the target region, where the projections used in (**A-C**) correspond to a 1:1, 1:17, 1:3.33 projection (15 cm, 17.5 cm, and 20 cm, respectively). The inset in panel B shows a close up of the region inside the box. The vertical dimension in the plots corresponds to the horizontal dimension in the true optical system.

4.3.4 Spectrometer Design

For the XUV spectrometer, it was desired to achieve a spectral resolution of approximately $\Delta E/E = 0.001$, for instance 50 meV at 50 eV. Because of the typical reflectivity considerations with XUV light, a reflective grazing incidence diffraction grating must be used to disperse the light. Ideally, to avoid more losses due to multiple reflections, this same grating would also be used to focus the light onto the imaging screen or CCD camera used to image the spectrum. Such concave, grazing incidence reflection diffraction gratings are indeed available for the XUV, and in fact variable line spacing algorithms have allowed for the development of aberration-free flat-field focusing using these optics, where the focal plane is normal to the grating surface (*146–148*). A grating was selected that is rated from 11-62 nm, or 20-113 eV (Hitachi #001-0640). The grating was lined with σ_0 = 1200 grooves/mm, had a radius of curvature of R = 5.649 m, a blaze angle of 3.7° (optimized for 16 nm), an angle of incidence of $\alpha = 4.7°$ grazing incidence, a source distance of r = 35 cm, an image distance of r' = 46.9 cm, and an area of 3 cm x 5 cm.

From the distances and angles specified, the footprint of the beam on the grating surface can be calculated based on the XUV beam size and divergence following the second ellipsoidal mirror. The footprint is shown in Figure 4.14. Although the angle of the grating is significantly more grazing than the preceding optics, the long focus of the second ellipsoidal mirror and means that the beam is only on the order of 1 mm in diameter (FWHM) when it impinges on the grating, and the beam is thus spread over a 1.5 cm FWHM (2.5 cm $1/e^2$ diameter) distance, which fits nicely on the grating surface without requiring an entrance slit. Covering this large fraction of the grating surface is optimal, because the energy resolution scales approximately linearly with the number of grooves illuminated $\Delta\lambda/\lambda \sim mN$, where m is the diffraction order and N is the number of illuminated grooves.

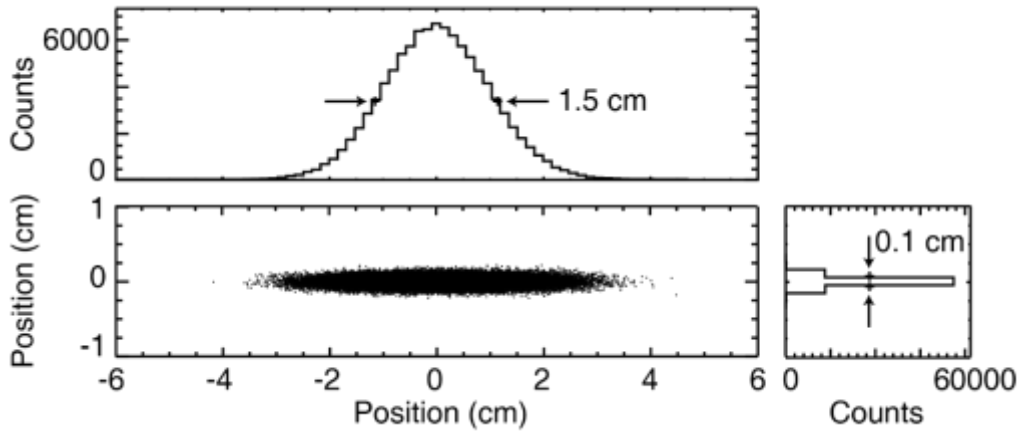

Figure 4.14. Footprint of the beam on the diffraction grating, at 4.7° grazing incidence and a distance of 35 cm from the second ellipsoidal mirror focus.

In order to properly simulate the diffracted and focused spectrum and thereby estimate the expected energy resolution, it was necessary to calculate the coefficients of the polynomial equation that governs the variable line spacing of the grating, and input this into *SHADOW3*. The form of the equation is shown in Equation 4.4, below – this and the below equations are taken directly from reference (*147*), which describes the variable line spacing conditions of the Hitachi gratings. The parameter σ describes the spacing between lines at a given position ω on the grating surface, along the direction normal to the grooves.

$$\sigma = \sigma_0 \left(1 + \frac{2b_2}{R}\omega + \frac{3b_3}{R^2}\omega^2 + \frac{4b_4}{R^3}\omega^3\right)^{-1}, \qquad \text{Equation 4.4}$$

The conditions on these coefficients can be derived by the application of Fermat's Principle to the light path function. Fermat's principle says that light will take the path between two points that takes the least amount of time to traverse, or that the light path function should be minimized. The light path function for reflection from a grating is given by

$$F = < APB > = < AO > + < OB > + \frac{\omega m\lambda}{\sigma}, \qquad \text{Equation 4.5}$$

Here the ray <*AO*> is the path from source point *A* to a reference point *O* on the grating surface (typically defined to be the grating center), <*OB*> is the ray from the point on the grating surface to the desired focal point, and <*APB*> is the minimum distance reflection path. The term $\omega m\lambda/\sigma$ is derived from the condition that for rays originating from two adjacent grooves ($\omega = \sigma$) the path difference is $m\lambda$, resulting in constructive interference at point *B*. For the grating selected, <*AO*> is equal to *r,* and ω describes the displacement of the diffraction origin point *P* from point *O*, along the grooved direction. The geometry is illustrated in Figure 4.15.

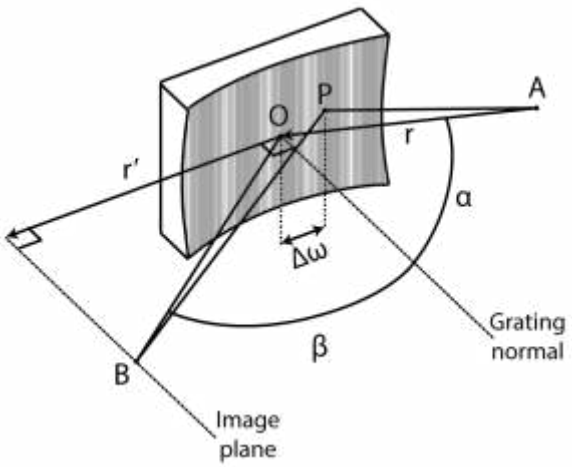

Figure 4.15. Concave variable line spacing reflective diffraction grating geometry. Point *O* is defined as the grating center. Adapted from reference (*146*).

In order to find a minimum in the light path function *F,* the condition can be set that $\delta F/\delta\omega = 0$ and (*149*, *150*). Ideally also the condition would be met that $\delta F/\delta l = 0$, where *l* is distance on the grating surface parallel to the grooves (perpendicular to ω), however these conditions are difficult to obtain simultaneously. The condition $\delta F/\delta\omega = 0$ was prioritized to obtain the best spectral resolution, where the beam will not be perfectly focused in the transverse (spatial) direction. By expanding *F* in a power series of ω and substituting in the known angles and distances, the coefficients in Equation 4.4 can be solved for, such that the point *B* for each wavelength falls as close as possible in the same flat-field plane. The resulting parameters for the grating selected are *b2* = -8.9, *b3* = 86.3, and *b4* = -1349. By comparing with Equation 4.4 the coefficients can be converted to the polynomial format used in *SHADOW3* that is given in Equation 4.6.

$$\sigma = \sigma_0(1 + a\omega + b\omega^2 + c\omega^3)^{-1}, \qquad \text{Equation 4.6}$$

The coefficients are calculated to be $a = 378\ \text{cm}^{-1}$, $b = 9.74\ \text{cm}^{-2}$, $c = 0.359\ \text{cm}^{-3}$. The sign difference in the odd powers comes from *SHADOW3* using the European convention of *m* = -1 for first order diffraction to the inside.

The ray tracing calculation was performed for the focal plane of the grating with the above parameters, and the spectral resolution was estimated. A representative spectrum is shown in Figure 4.16A, displaying the dispersion of the discrete energy lines at 36.8, 40.0, 43.2, 46.4, 49.6, and 52.8 eV (23^{rd}, 25^{th}, 27^{th}, 29^{th}, 31^{st}, and 33^{rd} harmonics, respectively) that were used as inputs. The focusing in the spectral dimension is quite sharp, with feature linewidths on the order of 8.5-9 μm FWHM. The focusing in the spatial direction (perpendicular dimension to the spectrum on the imaging plane) is not as sharp, as the variable line spacing algorithm was not optimized to meet this condition, and the FWHM of the beam is ~3 mm in the this direction. This may actually be advantageous however, because while the XUV pump pulse will typically be blocked before the spectrometer, there may be some possibility to observe both the pump and the probe beam on the camera, which would allow for constant monitoring of the static pump beam spectrum and possibly spectral interferometry between the two pulses. To understand the necessity of the variable line spacing, the same ray tracing calculation was performed with constant line spacing on the grating

(σ_0 = 1200 lines/mm). The result is displayed in panel B, showing FWHM linewidths on the order of several millimeters, certainly not sufficient to meet the desired $\Delta E/E < 0.001$ energy resolution condition.

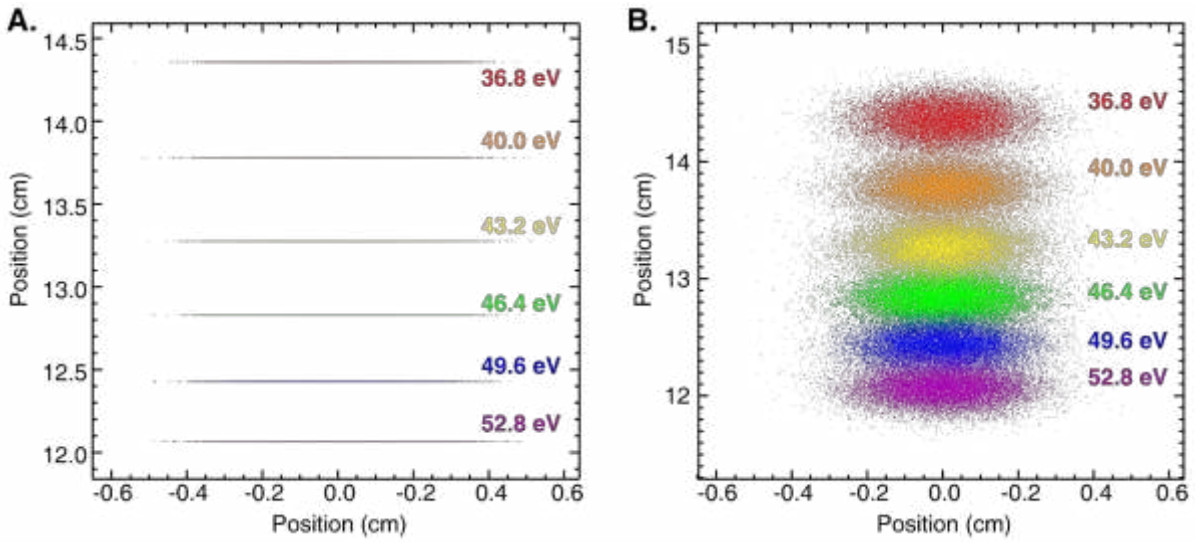

Figure 4.16. Simulated spectrum via ray tracing for (**A**) Hitachi concave variable line spacing reflection grating #001-0640, and (**B**) a grating of the same concave geometry but with constant line spacing, showing significantly worsened resolution.

For the variable line spacing case, the energy was calibrated and fit as a function of position on the imaging plane with a second order polynomial, and is shown in Figure 4.17A. To estimate the resolution at each energy, the FWHM of each line in the ray tracing simulations was characterized. The energy resolution was then approximated as the separation for which two adjacent and overlapping features would have a 2:1 peak to valley ratio, which corresponds to the full-width at quarter-maximum. For a Gaussian feature, which describes the line broadening due to the diffraction grating, it can be easily shown that the width at quarter maximum is equal to the FWHM multiplied by $\sqrt{\ln(4)/\ln(2)}$. The resulting energy resolution as a function of energy is plotted in Figure 4.17B. The lens-limited energy resolution due to the grating (assuming perfect alignment and the source conditions described) is quite good, and it easily meets the $\Delta E/E < 0.001$ condition. In this scenario the energy resolution would actually be limited by the 20 µm pixel size on the XUV CCD detector, which is significantly larger than the ~8.5-9 µm FWHM line width values obtained via ray tracing. The resulting pixel limited energy resolution from this camera as a function of energy is thus plotted in Figure 4.17 for comparison. The condition $\Delta E/E < 0.001$ is still easily met in the pixel-limited regime.

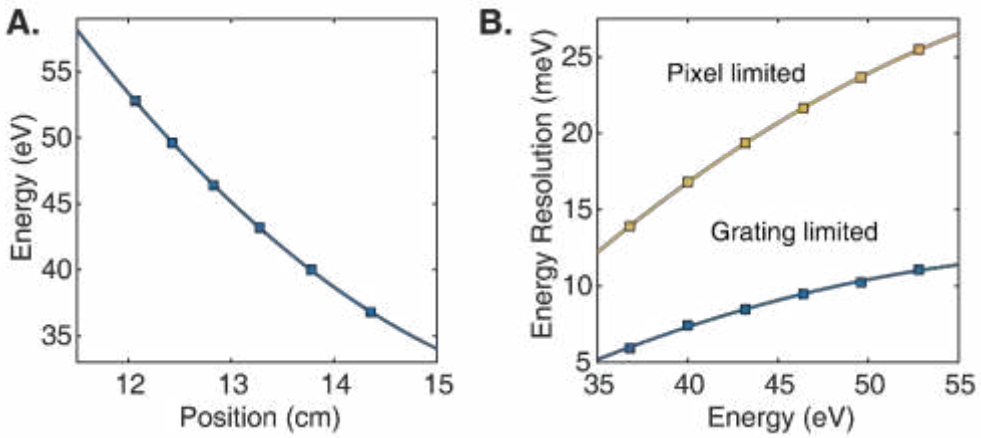

Figure 4.17. (**A**) Energy as a function of position in the imaging plane of the diffraction grating, where the points correspond to the 23rd – 33rd odd harmonics and the line is a second order polynomial fit. (**B**) Grating limited and pixel limited energy resolution as a function of energy based on line widths obtained in the ray tracing calculations. The points correspond to the same odd harmonic energies and the line fits are also second order polynomials.

Chapter 5.

Endstation Vacuum System Design, Assembly, and Testing for Attosecond-Pump Attosecond-Probe Experiments

In Chapter 4, the plans to build an experimental endstation for attosecond-pump attosecond-probe measurements were introduced, the intensity requirements were determined, and the decided-upon optical layout was described. This chapter covers the design and construction of a vacuum endstation to house these optics and accommodate various diagnostics such as spatial beam profiling and temporal pulse characterization. The final sections of this chapter describe the testing that has been performed to date, some of which was established at UC Berkeley and some of which was carried out at University of Central Florida (UCF), following the disassembly, shipping, and reassembly of the apparatus at its final location. Next steps, remaining tasks to be done, and plans for the first experiments to be performed are outlined at the end of this chapter. Similar to Chapter 4, the content described herein is intended to serve as a resource for current and future students and postdoctoral scholars on the project, and some time is spent on possible complications and future improvements, which is not meant to take away from the benefits and achievements of the current design.

5.1 Vacuum System Design and Construction

Following the high harmonic generation (HHG) process that produces the extreme ultraviolet (XUV) source, the residual near-infrared (NIR) light from the HHG process is removed using either two silicon wafers at Brewster's angle or two dielectric mirrors that are reflective to XUV radiation and transparent to NIR. The optical mounts for these mirrors (which will also be used for beam steering into the endstation) and the vacuum chamber to house them have been designed and constructed by the group of Zenghu Chang at UCF, where the apparatus is being housed. At the far end of their chamber, an XUV beam with only minimal residual co-propagating NIR is exiting at a 30 degree downward angle. The exit of this chamber marks the starting point of the UC Berkeley endstation, which must be coupled to the downward-angled exit port and beam. The endstation optics have been partitioned into three chambers to house the optics described in Chapter 4: a split-mirror chamber, a target chamber containing both ellipsoidal mirrors, and a spectrometer chamber housing the diffraction grating. These chambers will be described one-by-one in the following sections, with a focus on the main housing and optics mounts. Descriptions of additional diagnostics will be provided in Section 5.2. An overview of the entire vacuum system is shown in Figure 5.1.

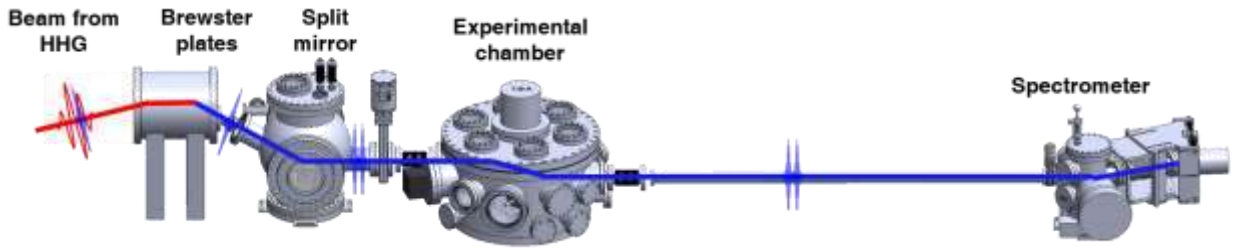

Figure 5.1. Overview of the vacuum chamber layout of the attosecond-pump attosecond-probe endstation. An XUV pulse (blue) with residual NIR light (red) enters the Brewster plate / dielectric reflector chamber where the NIR is removed. The XUV light is then coupled into the UC Berkeley endstation where it is time-delayed to produce a pump and probe pulse in the split mirror chamber, focused through the target region in the experimental chamber, and refocused into the spectrometer chamber.

5.1.1 Split Mirror Chamber

To house the split mirror (the first optic in the endstation layout) a chamber with a 30 degrees downward angled entrance port and horizontal exit port was designed. A 9" beam height was chosen as a convenient working height above the table throughout the endstation. The beam coming from the high harmonic source is at a height of 19.5" above the table, and thus with the 30 degree incidence angle to achieve the desired beam height, the second Brewster plate and the split mirror must have an 18.2" separation. Between this and every other pair of vacuum chambers, a flexible bellows was installed to aid in vibration damping. To allow for this the split mirror had to be mounted slightly off center in the chamber, closer to the entrance, to keep the separation and subsequent beam heights correct. The chamber design and final construction is illustrated in Figure 5.2. The back side (not visible) includes ports for a 300 L/s turbo-molecular vacuum pump, a gas inlet and chamber venting valve, and electrical feedthroughs to control the five-axis alignment stages and delay stage on which the split mirrors are mounted. The front side has only a viewport, and the chamber lid has a viewport to look down on the two split mirrors, a port for an ion gauge to measure the chamber pressure, and two linear motion feedthroughs that allow different filters to be inserted. Additional ports could be made available through the use of tees or crosses, if needed.

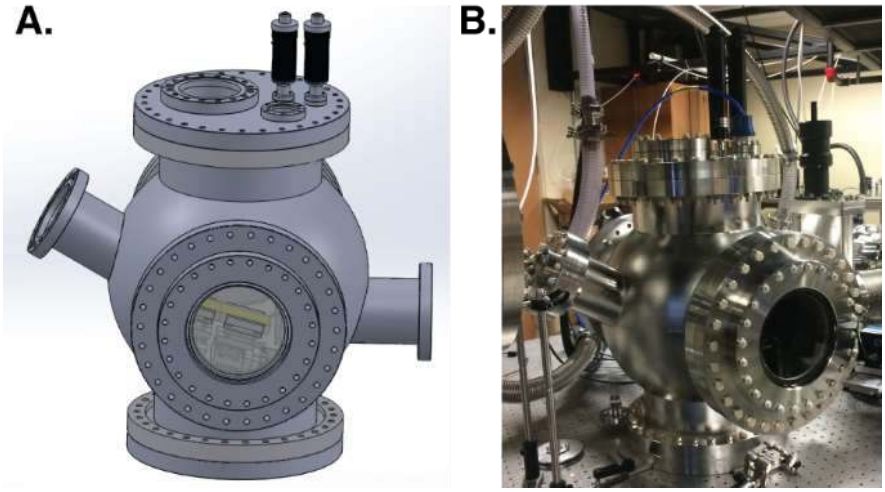

Figure 5.2. Split mirror chamber CAD design (**A**) and final construction (**B**). The XUV beam enters from the top left at a 30 degree downward angle and exits the chamber horizontally to the right, following reflection on the split mirror.

For these experiments, metal filters will be critical to attenuating both the pump and probe beams. In particular, being able to attenuate the probe beam independently of the pump beam will be key to making sure that it is significantly weaker and will not be inducing dynamics. The off-center positioning of the split mirror is actually convenient in this regard, as there is space for two different rails of filters to be installed just past it, which can be inserted into the beam path in different combinations. The filter holder design is shown in Figure 5.3. Each filter rail has four clear apertures that can be accessed and can hold up to eight filters (four on the front side, four on the back side). The front side is designed to hold standard circular filters, through which the pump and probe beams will both transmit and be attenuated. The back side of the filter rail has a square inset that prevents filter rotation, and it is intended to hold custom half-circular or other alignment-sensitive filters, which could attenuate or spectrally filter one of the beams selectively. The rotation sensitive filters should be mounted on a square mount or have a straight edge machined onto the filter ring, as shown in Figure 5.3B, which prevents rotation. The filter rail will also be able to hold custom aperture masks (see Chapter 4) once the desired conditions for the pump and probe beam size and shape have been decided.

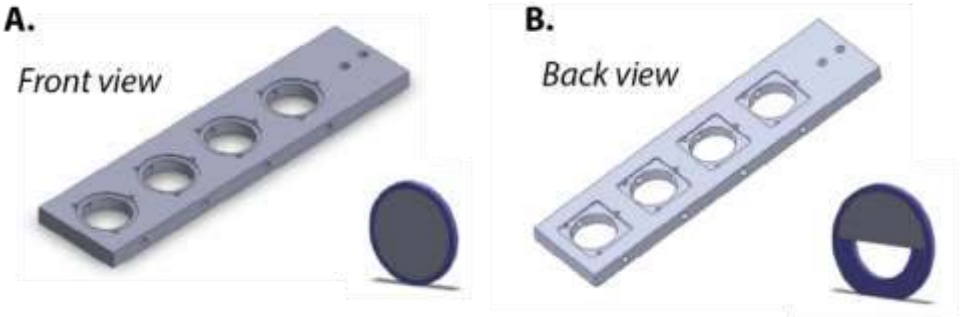

Figure 5.3. Filter holder design for post-split-mirror attenuation or aperturing of the pump and probe beams. The front side (**A**) is designed to hold standard circular filters that are not sensitive to rotation, as shown in the inset. The back side (**B**) is designed to hold custom filters that need to be kept straight, for instance the half-circular filter shown in the inset. These filters should be

manufactured with either a square mounting substrate, or a straight edge on the ring holder, and installed in the filter holder such that this edge is kept flush with the square engraving.

Following the filter holders, some additional room in the chamber was initially used for an alignment iris. Depending on the amount of NIR light remaining in the beam, it may be possible to use this iris for regular alignment, by raising any metal filters out of the beam path (making sure the gate valve between this chamber and the next is closed), and using the visible beam to align on. If the NIR light is not bright enough the iris may need to be replaced with a scintillation detector for the XUV, one version of which is described in more detail in section 5.2.1. Alternatively, if the NIR light is too intense it is possible some thicker filters or a microchannel plate (*151*) will need to be installed before the split mirror to remove this residual NIR and avoid damaging the mirror's gold coating. A close up of the inside of the chamber in its current configuration at UCF is shown in Figure 5.4, showing the split mirrors mounted on stages followed by filter rails and an alignment iris.

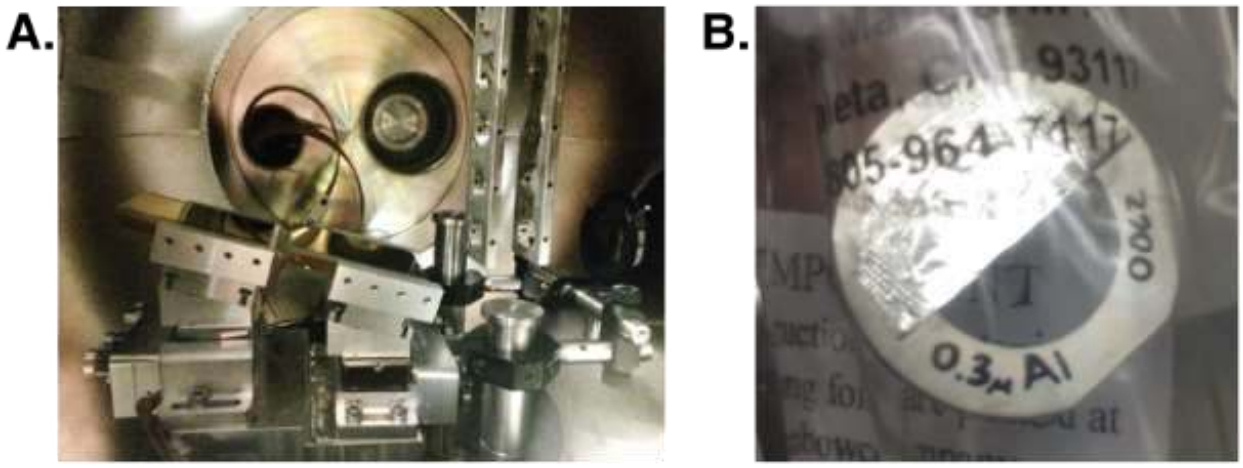

Figure 5.4. (**A**) Inside of the split mirror chamber showing all hardware. Split mirrors are mounted on (from bottom to top) an aluminum base block which is taller on the upper mirror side, a five-axis alignment stage, an angled adapter piece, and a delay stage (spacer piece) for the lower (upper) mirror. The mirrors are mounted off center in their brackets in this picture such that the full beam is captured on the lower mirror. (**B**) A close up of one of the half circular filters that could be installed in the filter rail and used for attenuation of the probe beam.

Regarding future modifications, as described in Chapter 4, if spatial walk off of the pump and probe beams as a function of time delay becomes significant, the five-axis stages may eventually need to be replaced with a closed loop angular alignment stage. This may be desired in any case, for ease of use – in the current five-axis scheme the in-plane rotation and horizontal beam steering degrees of freedom are coupled, meaning that the mirror top edge can deviate from horizontal if significant horizontal beam steering correction is ever required. The system can certainly be used for experiments in its current form, but remedying this issue would represent a significant improvement to the apparatus. One other option (similar to what will be described for the ellipsoidal mirror mounting) is to simply add a horizontal tilt stage into the design, which will add independent horizontal rotation to the XYZ translation, vertical rotation, and in-plane rotation that are possible with the current stages.

5.1.2 Target Chamber

Following the split mirror chamber the XUV beam must be focused through the target region, for which a 20 degree grazing incidence ellipsoidal mirror will be used. A one meter distance between the center of the split mirror and ellipsoidal mirror was fixed, which allows plenty of distance for flexible coupling and a gate valve between the two chambers. Since the ellipsoidal mirror must be 9 m from the HHG source this determined the final positioning of the endstation in the room. The ellipsoidal mirror focuses the XUV light with a 15 cm focal length (900 cm to 15 cm, or 60:1 projection) into the target region, where solid state samples and other various diagnostics can be placed. At 15 cm past the target region is a second ellipsoidal mirror, which re-focuses the XUV light with a 250 cm focal length (15 cm to 250 cm, or ~1:17 projection). Because the two ellipsoidal mirrors and target region diagnostics are all closely packed together, all of these components must be housed in the same vacuum chamber. A variety of chamber shapes and sized were considered, but ultimately a cylindrical (tub-shaped) chamber was chosen to house these optics, as it has the most flexibility to alternative beam paths and having various diagnostics enter from all sides.

One serious consideration for the future is if and how to incorporate the 500 eV soft x-ray (SXR) attosecond pulses that will be produced by a frequency domain optical parametric amplifier (FOPA), which is to be provided by the research groups of Paul Corkum and François Légaré at the University of Ottawa and INRS, respectively. These pulses could potentially be combined in the endstation to perform groundbreaking attosecond XUV-pump SXR-probe experiments. Ideally for an attosecond experiment the XUV pulses and soft x-ray pulses should propagate co-linearly, or very nearly co-linear, because a relative angle can broaden the temporal instrument response function quite significantly, as described in Chapter 1. This becomes geometrically challenging for this experiment because the ellipsoidal mirror needed to focus the XUV to high intensity cannot be used to focus the SXR pulses, which require very grazing incidence angles. Strong ellipsoidal focusing geometries cannot be manufactured at such grazing angles (see Chapter 4), and there are generally not multilayer coatings or zone plate geometries available that have sufficient broadband reflectivity in both the XUV and SXR.

The current plan to couple in the SXR light is to use an annular mirror geometry, where the x-ray probe pulse is coupled in through the back of a small hole in the optic just before the focus, as is often done for NIR-pump XUV-probe experiments. In the current optical layout this would be through the ellipsoidal mirror, and a spare of this optic was ordered potentially for this purpose. Alternatively a grazing incidence plane mirror could be installed just past the ellipsoidal mirror, with a hole through which the x-ray beam is coupled in. With a 15 cm focal length this becomes very crowded in the target area, and more XUV flux will be lost from the additional reflection in addition to the hole in the mirror, but it is theoretically possible and would not risk damaging the ellipsoidal mirror surface. Some alternative possible beam paths through the target area incorporating the SXR are illustrated in Figure 5.5. Many of the ports were made quite large in diameter to allow for a variety of incidence angles, and as many ports as reasonably possible were designed into the chamber body. Alternatively femtosecond XUV-pump SXR-probe experiments would be much easier to achieve, and there are many more possibilities where a small relative angle between the beams can be tolerated. In any case, a focusing optic for the 500 eV light will need to be obtained, and a small chamber to house this will have to be designed and attached to the main target chamber. The spectrometer will have to be moved to the exit of the 500 eV beam

and a new refocusing mirror and diffraction grating appropriate for the SXR wavelengths will need to be selected.

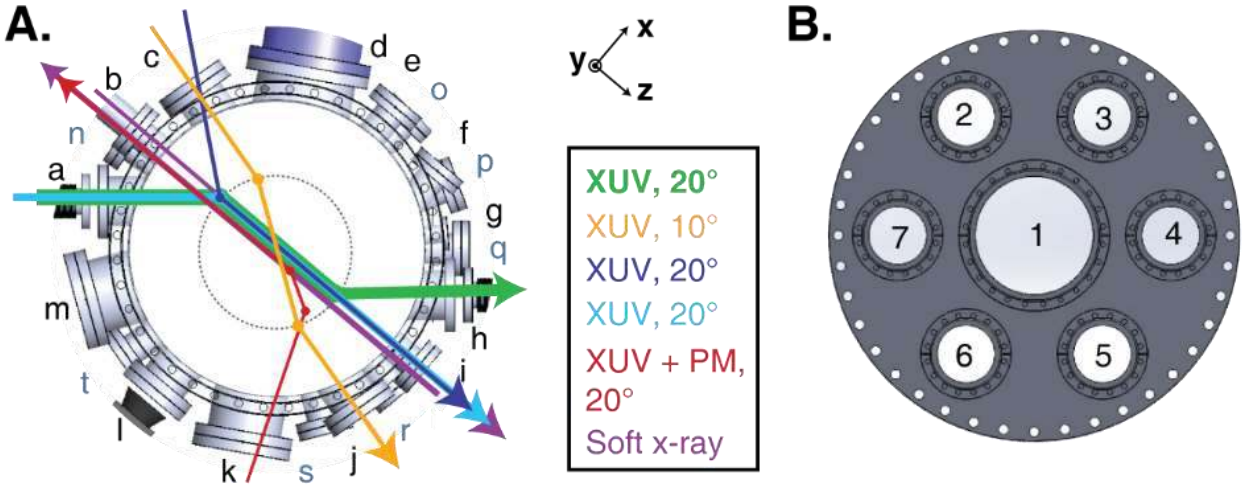

Figure 5.5. (**A**) Top-down view of the target chamber geometry. Alternative beam paths for the XUV are highlighted in green (the current geometry), orange, navy, cyan, and red. Possible beam paths for the SXR light are shown in violet, which is coupled in either through the back of the first ellipsoidal mirror a plane mirror (PM). The circle inside the chamber is of 15 cm radius, corresponding to the focal distance of the ellipsoidal mirrors. Many more alternative beam paths are possible that do not focus perfectly to the chamber center (all that are illustrated do) or have different focal lengths. Black-lettered ports are positioned either on the center or upper half of the chamber and grey-lettered ports are positioned on the bottom half of the chamber. (**B**) Chamber lid geometry, with six six-inch diameter ports and one ten-inch diameter port.

The chamber is sealed with a 27-1/8" wire seal flange at the lid, which is illustrated in Figure 5.5B. Removing the lid requires the use of a gantry crane or other hoist, as the weight is too heavy to be raised manually. Attachment hooks are installed on the lid for this purpose, and rigging was obtained that is rated to lift the lid and even the entire chamber, if needed. The lid incorporates several large-diameter ports such that much of the assembly and alignment inside the chamber can be done through these access points without having to go through this process.

For the initial installation, the most convenient beam path for XUV-pump XUV-probe experiments was selected, illustrated by the green beam path in Figure 5.5A. Given this optical layout, the various diagnostics and electrical feedthroughs required to run an experiment can be assigned to the most convenient port. For the chosen beam path the assigned purpose of each port is described in Table 5.1. Each ellipsoidal mirror is mounted on a 5-axis alignment stage and an additional vertical tilt stage. In the target region, sample translation in X, Y, and Z is desired, where the assignment of these axes can be seen in Figure 5.5A. Five-centimeter travel range stages were selected for the X and Y directions to move between different targets (multiple solid state samples, a gas cell, an imaging screen, etc.) and for raster scanning capability. A one-inch travel range was selected for the Z direction, to ensure the target is positioned at the focus and possibly perform some characterization such as an M^2 scan. The breadboard in the chamber bottom was aligned to X and Z, and the ellipsoidal mirrors were mounted on custom posts adapted to this angle. A photograph of the chamber as assembled at UCF is shown in Figure 5.6, below. The geometry at

the target region will be covered in more detail in Section 5.2 where various other diagnostics are described.

Table 5.1. Description of each port on the chamber body and lid, and its intended use.

Port	**Size (inches)**	**Assigned use**
a	6	XUV beam entrance
b	4.5	Spare
c	6	Spare
d	10	1000 L/s turbo pump
e	4.5	15-pin sub-D connector feedthrough (*2 x picomotor tilt stages*)
f	4.5	Spare
g	2.75	Ion gauge
h	6	XUV beam exit
i	4.5	Viewport
j	6	Gas inlet for target gas cell / nozzle
k	8	Viewport
l	6	Imaging the focus
m	8	Viewport
n	4.5	15-pin sub-D connector feedthrough (*Ellipsoidal #1, 5-axis stage*)
o	4.5	2 x 15-pin sub-D connector feedthrough (*VT-80 stage, XY translation*)
p	4.5	15-pin sub-D connector feedthrough (*picomotor stage, Z translation*)
q	4.5	Spare
r	4.5	15-pin sub-D connector feedthrough (*Ellipsoidal #2, 5-axis stage*)
s	4.5	Spare
t	4.5	Spare
1	10	Time-of-flight spectrometer
2	6	Gas purge inlet
3	6	Viewport
4	6	Spare (/reaching into chamber)
5	6	Chamber venting valve
6	6	Viewport
7	6	Spare (/reaching into chamber)

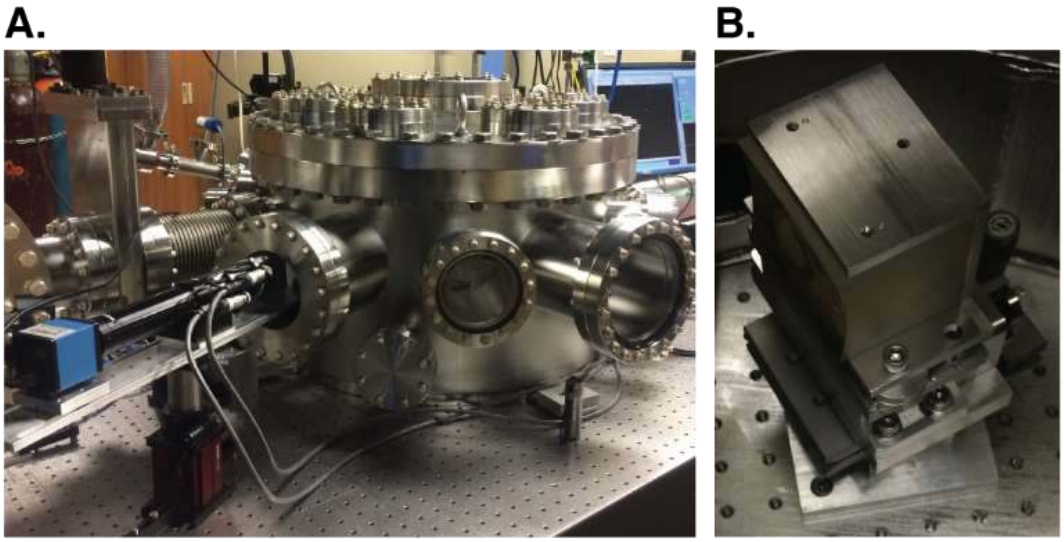

Figure 5.6. (**A**) Target chamber as assembled at UCF, where the beam enters through port (a) in the top left. Ports (m), (l), and (k), and (t) are also visible. (**B**) A close up of one of the ellipsoidal mirrors as mounted in the chamber. The mirror sits on a pedestal, followed by a vertical tilt stage (the micrometer screw visible in the photograph has since been replaced with a picomotor), a five-axis stage, and a mounting bracket.

5.1.3 Spectrometer Chamber

Following the target region, the XUV beam is refocused into a spectrometer, which enables absorption measurements and spectral characterization to be performed. The distance between the ellipsoidal re-focusing mirror and the diffraction grating is set by the image and source distances of each of these optics (250 cm and 35 cm, respectively), and adds up to a total separation of 285 cm. A long tube was used to cover most of this distance, encompassing the second ellipsoidal mirror focus along the way. Potentially in the future the tube could be shortened and a small additional vacuum chamber could be placed around this point, allowing for lower-intensity XUV measurements. Currently however, the beam couples through a gate valve directly into the spectrometer chamber, which is illustrated in Figure 5.7. Per the grating specifications, the energies from 11-62 nm (112-20 eV) are focused on a flat-field plane normal to the grating surface, and cover a distance of just over 11 cm. The chamber has been designed such that the XUV CCD camera can translate on a rail along this plane. The camera is connected to the chamber by a custom flexible membrane bellows and structural supports. The clear aperture through the bellows allows the full CCD camera chip (1-inch width) to be illuminated at each position along the rail, giving access to the full spectral range of the grating without breaking vacuum. Additionally, a small amount of rotation of the camera in the plane is possible, to make a correction if the CCD chip is mounted with a slight tilt, and the rail mounting can be adjusted to move the imaging plane closer or further from the chamber, if the grating is for any reason not centered.

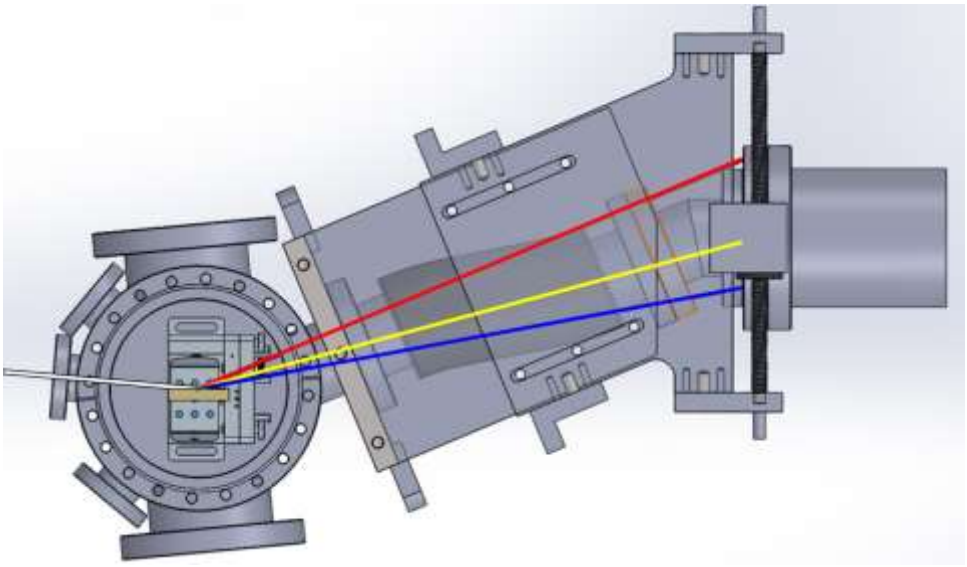

Figure 5.7. Spectrometer chamber design, showing incident beam coming in from the left, and diffracted XUV energies in red, yellow, and blue (low to high energy) propagating to the right and focused onto the same flat-field plane, along which the XUV CCD camera can translate. This design has been modified from a similar spectrometer design by the Max-Planck Institute for Nuclear Physics machine shop in Heidelberg, Germany, in collaboration with Christian Ott.

In the chamber lid (not visible in Figure 5.7) a small flange is positioned directly between the grating and the beam entrance, which could allow an entrance slit or pump beam block to be inserted on a linear motion feedthrough. Additional flanges on the spectrometer chamber are intended for a 300 L/s turbo pump, an ion gauge to measure the chamber pressure, a gas purge valve, a chamber venting valve, and a 15-pin sub-D connector electrical feedthrough for the five-axis positioner on which the grating is mounted. Similar to the split mirror mounting, this stage setup could be improved in the future by adding an additional tilt stage – currently the in-plane rotation of the grating surface is not an accessible dimension with the stage, and steel shims were used to ensure the grating grooves were aligned perfectly vertical (see section 5.2.3 for actual testing of the grating resolution and alignment details). This would be equally necessary with a mirror mount geometry, which also only has two rotation axes and is missing the in-plane rotation. The spectrometer chamber as assembled at UCF is shown in Figure 5.8.

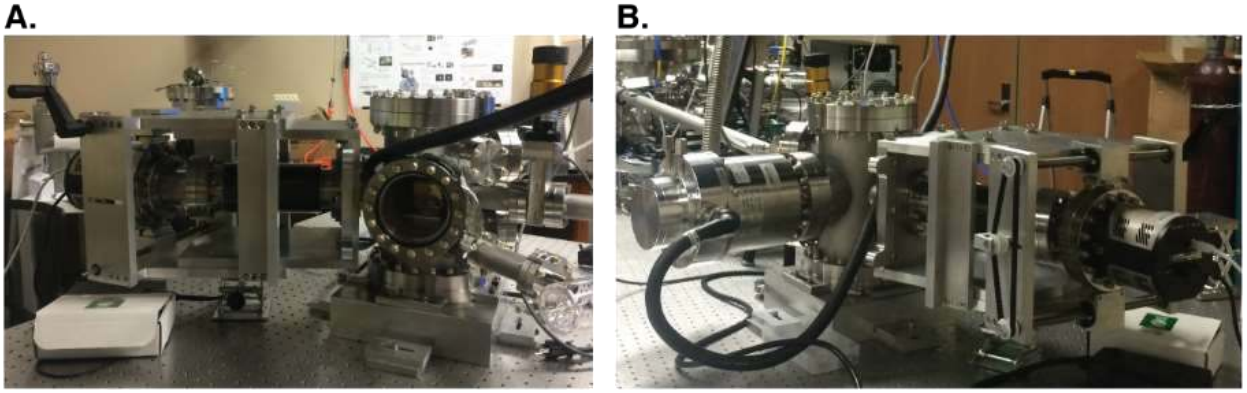

Figure 5.8. Spectrometer chamber as assembled at UCF. (**A**) Front view, where the grating is visible through a viewport in the chamber. Here the beam enters the chamber from the left hand side. (**B**) Back view of the spectrometer chamber, where the CCD camera mounted on a rail is visible. The beam enters through the narrow tube coming from the upper left of the photograph.

While this chamber could potentially be used as a spectrometer for the 500 eV SXR pulses by switching out the diffraction grating, it will probably be desirable to design a separate SXR spectrometer that can be placed at the alternative beam exit for XUV-pump SXR-probe experiments. The entire coupled system as assembled at UCF is shown in Figure 5.9, below.

Figure 5.9. Attosecond-pump attosecond-probe endstation as installed at UCF.

5.2 Diagnostics and Preliminary Testing

As touched on in Section 5.1.2, many of the ports in the target chamber are designated specifically for critical diagnostics. In addition to the time-delay and focusing that are done by the main beam-path optics, it will be critical to check beam overlap of the pump and probe, measure the beam profile, calibrate the intensity, determine the temporal instrument response function, and calibrate the XUV spectrometer. In the following sub-sections the diagnostics that were designed for this purpose will be described, and preliminary testing that has been done will be presented. In addition to the individual measurements described herein, the entire vacuum system has also been tested chamber-by-chamber, and was able to be pumped down to ~ 10^{-7} Torr pressure at UCF. The turbo pumps are backed by dry roughing pumps (7.5, 21.2, and 7.5 ft^3/min. for the split mirror chamber,

target chamber, and spectrometer chamber, respectively) to avoid potential oil contamination that might nucleate damage to the optics.

5.2.1 Beam Profiling, Spatial Overlap, and Intensity Measurements

One of the most critical diagnostics to performing experiments with this endstation is ensuring that the pump and probe beams are spatially overlapped. In the visible and NIR this can be done very easily by sending the light onto a beam profiler. However, in the XUV the beam cannot propagate outside of vacuum, and with the short focal lengths at the target region it is not possible to fit an XUV CCD camera in this region. Thus it is necessary to convert the XUV light to visible prior to imaging, which can be done via scintillation.

A scintillator is simply a material that emits luminescence following the absorption or scattering of incident ionizing radiation in the medium. Many phosphors are commonly used for this purpose when imaging electron beams or x-ray radiation. In the XUV the light is often first converted into electrons using a microchannel plate (MCP). The electrons are then imaged using a phosphor screen, and the higher particle count from electron multiplication in the MCP increases the brightness of the resulting image. However, because of the size of the channels, achieving few- or sub-micrometer resolution with an MCP is not possible. Thus a scintillator must be found that will luminesce directly from XUV light, brightness and scattering in the medium must be considered, and microscope optics must be selected.

As a medium, a cerium doped yttrium aluminum garnet (Ce:YAG) crystal was selected, which has been demonstrated to work quite well with XUV light in several previous applications (*152*, *153*). The XUV penetration depth in Ce:YAG is only ~10 nm (*154*) which is easily sufficient to avoid any blurring effects due to scattering in the medium. The crystalline structure also prevents spatial resolution losses due to scattering at grain boundaries in the material. There are two different ways that a scintillator material can be used for XUV imaging. The first is to use a thin screen of the material and collect all of the visible light transmitted through the back side with a microscope objective. This visible light can then be relayed out of the vacuum chamber and magnified onto a CCD camera. However, in this case it is difficult then to increase the field of view of the image, because the lens behind the scintillator is fixed in vacuum. A more desirable option would be to be able to zoom in and out, depending on how far apart the pump and probe beam spots are. This can be done using a long-range microscope outside of vacuum, e.g. at a 45° angle to the scintillator surface. The disadvantage is that significantly less light is collected, and the magnification capability is not as strong. However, if sufficient resolution and sensitivity can be achieved in this way this would be the optimal solution. The magnification capability will depend on how close the objective lens can be brought to the scintillator, while still remaining outside of vacuum. Because of the large diameter of the target vacuum chamber, it is necessary for the imaging system to protrude into the chamber, as illustrated in Figure 5.10. It was determined that a >10 cm working distance would be required for the imaging system to not get in the way of the target area, which includes a time-of-flight spectrometer that comes down from the chamber lid (see Section 5.2.2, not pictured in Figure 5.10).

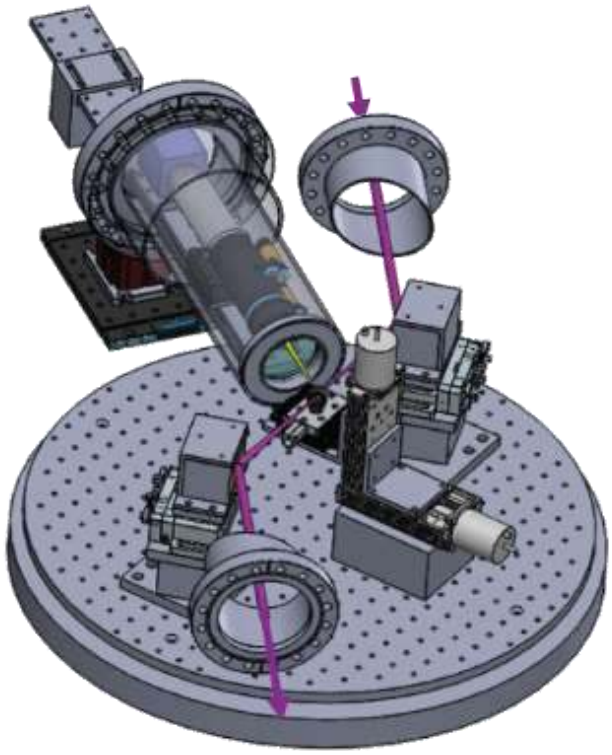

Figure 5.10. Scintillator imaging geometry in the target chamber. The XUV beam (purple) enters from the top and is focused onto the scintillation screen. Yellow light (550 nm) is emitted from the medium, and captured by a long range microscope that protrudes into the vacuum chamber. The cone of light collected is shown in yellow.

An adjustable long-range microscope with a working distance of 10.8 cm and motorized focus and zoom was selected. The specified numerical aperture at maximum magnification for this system is $NA = 0.076$. While the ultimate resolution and NA will depend on the properties of the full optical system, including the vacuum viewport, this value was used to perform some basic estimates. From the relationship $NA = n \sin(\theta)$ and assuming an index of refraction is 1.00 for air/vacuum, the half-angle of the cone of light collected is equal to $\theta = 4.3°$. This corresponds to a solid angle of $\Omega = 2\pi*(1-\cos(\theta)) = 0.018$ sr. Dividing by 4π, the fraction of light collected is ~0.14%. With regard to the efficiency of the scintillation process, Ce:YAG has an emission maximum of 550 nm and a yield on the order of 24,000 visible photons per MeV of incident energy, which does not depend strongly on the irradiating photon / particle energy (*155*, *156*). Thus for a central photon energy of 50 eV we can expect ~1.2 visible photons per XUV photon. For 660 nW pump beam (66 nJ/pulse at 10 Hz, see Chapter 4) this corresponds to 25 nW of visible light emission. If the pump beam spot size is 5 µm, this is equal to a radiant intensity of 1,300 W/m^2, which at the scintillator emission wavelength of 550 nm is equal to 870,000 lux (lx). Based on the fraction collected and with 1:1 magnification this would be equal to 1200 lx on the detector. A CCD camera with 0.15 lx sensitivity and 4.65 µm pixel size was selected, which will easily be sufficient to detect this light even at 5X or greater magnification, where the illuminance would be reduced to ~50 lx.

As mentioned, the decreased spatial resolution that comes with the longer working distances is the largest drawback of this method. Based on the microscope specifications the lens-limited

resolution is 4.4 µm for this system, although centroids can be determined with greater accuracy. To get a more realistic estimate with the vacuum viewport included, a demonstration was scheduled and the system was characterized using a resolution test target (1951 USAF target, non-emitting source).

The results are shown in Figure 5.11, and a spatial resolution of 2.8 ± 0.1 µm was obtained. This was determined to be acceptable. While in the optimal case the probe beam could be focused as small as 1.1 µm (see Chapter 4), it will still be possible to align the centroid with that of the pump beam. As the pump beam will be larger than the probe beam, this resolution should be sufficient for determining the pump beam size for intensity calibration. In the worst case scenario, it will still be possible to mount a fixed objective and relay mirror behind the scintillator for increased resolution imaging, and with illumination the motorized system can be used for *in situ* sample characterization and checking for damage.

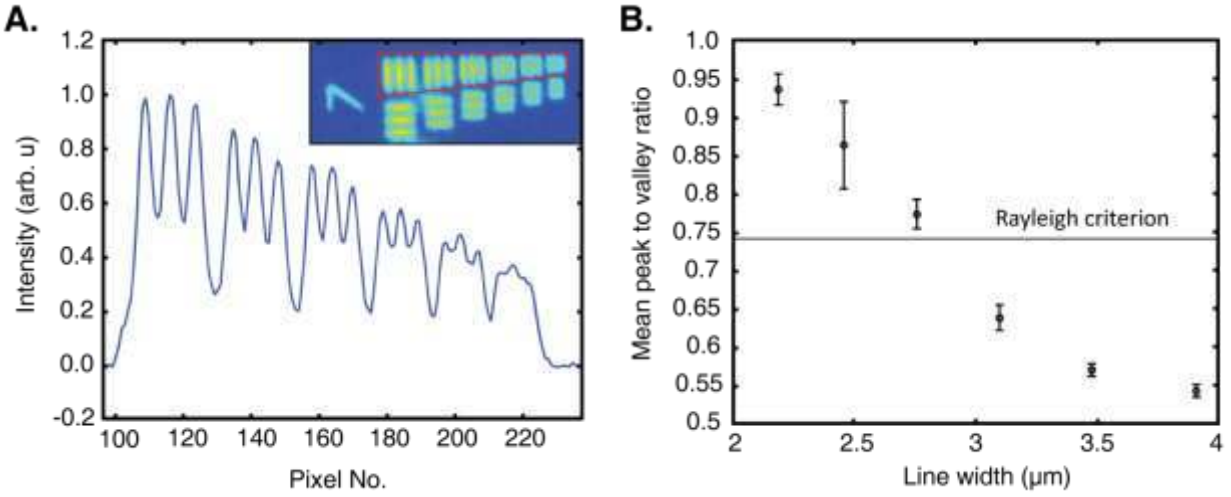

Figure 5.11. Resolution measurements for the long-range optical microscope system used to image the scintillator, performed with visible light. (**A**) Integrated image over the resolution target at maximum magnification, through the vacuum viewport. Inset shows the 2D image, where the vertically integrated and normalized amplitude in the red boxed region is plotted in the main graph. (**B**) The mean peak-to-valley ratio for each set of lines in (**A**), where the linewidths are taken from the resolution test target data.

In addition to the size of the pump beam, it will be necessary to measure the pulse energy in order to determine absolute intensities in the XUV. To this end, an XUV sensitive photodiode was ordered, which can be placed in the target area to perform this measurement. The diode should be installed near the scintillator, and it can be moved into the beam path using the XY translation stages in the sample area. These stages allow access to a 5 x 5 cm square area in which the scintillator (installed in a half-inch mirror ring mount), the XUV photodiode, several solid-state samples, and a gas cell or nozzle could theoretically all be installed and moved in-between. The exact mounting details and adapters remain to be designed and determined.

While XUV pulses were not yet available at the time that the endstation was installed, some preliminary alignment of the ellipsoidal mirrors was done using a helium neon laser (HeNe) and a

visible beam profiler. A telescope was used to match the HeNe focus position and divergence to the estimated XUV beam conditions described in Chapter 4, with the focus a distance of 9 m from the first ellipsoidal mirror and a beam size of 9 mm full-width at half-maximum (FWHM) after 9 m propagation distance. The beam profiler was set up in the target region on a rail, to move along the beam path. It was confirmed that the beam focused where expected, in the center of the chamber at a 15 cm distance from the first ellipsoidal mirror. An alignment procedure was then tested to optimize the beam profile, similar to what is typically done for toroidal mirrors. The procedure is illustrated in Figure 5.12, and more description can be found in reference (*157*).

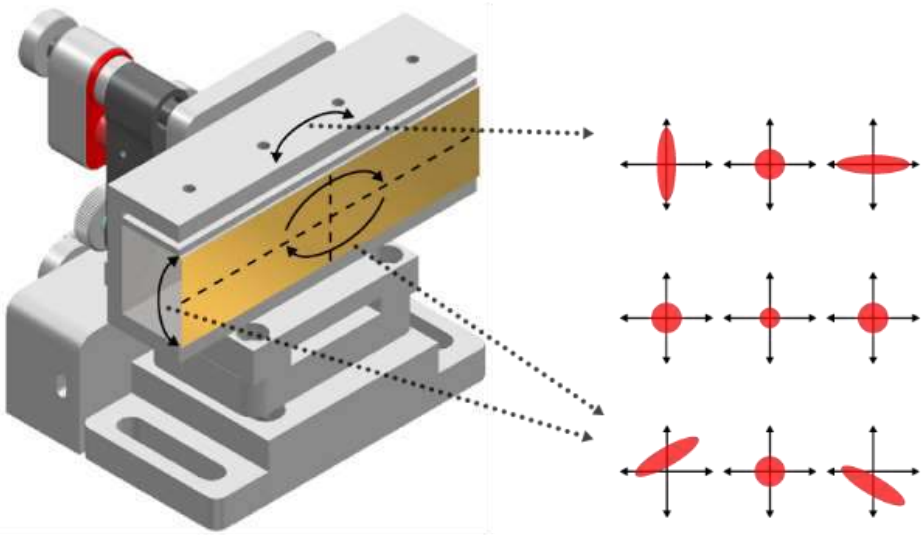

Figure 5.12. Ellipsoidal mirror alignment procedure: the in-plane rotation is used to compensate any rotation of the beam profile and the vertical rotation is then used to ensure the beam remains at the correct height, iterating between these two degrees of freedom as needed. The horizontal tilt is used to compensate astigmatism and ensure the beam profile is symmetric. Figure obtained from reference (*157*), used with permission.

The HeNe beam profile obtained using this procedure for the first ellipsoidal mirror is shown in Figure 5.13, below, and it had a FWHM of 25-30 µm, nearly limited by the 20 µm pixel size of the detector. For an XUV beam of the same divergence, according to Gaussian beam optics, the beam waist and FWHM at the focus should be reduced by the ratio of the HeNe wavelength to the XUV wavelength, or 633:25 nm, which gives a FWHM value of 1.0 µm, quite similar to what was predicted by the ray tracing calculations in Chapter 4. Depending on the Gaussian beam quality (M^2 value) and aperturing the actual XUV beam diameter may be larger; however, if the HeNe testing is any indication, the alignment procedure and optimization should be relatively straightforward. For the XUV case, beam profile measurements will be made using the scintillation detector as opposed to the beam profiler. The second ellipsoidal mirror was pre-aligned with the HeNe beam in the same way as the first. If an additional chamber is eventually installed just before the spectrometer chamber, it may be desirable to place a scintillation screen at that position as well, for characterization of the second focus.

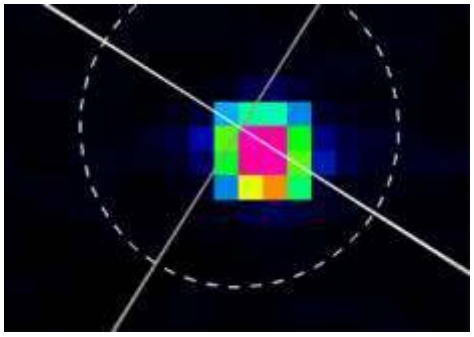

Figure 5.13. Beam profile at the focus of the first ellipsoidal mirror using a HeNe laser for alignment. The pixel size of the beam profiler is 20 μm.

5.2.2 Temporal Pulse Characterization – Time of Flight Spectrometer

In addition to achieving spatial overlap of the XUV pump and probe beams, it is also critical to find temporal overlap of the pulses (time zero) and characterize the pulse duration. Because no electronics are fast enough to gate measurements on the atto-to-femtosecond timescale, each pulse must be characterized using the other, in a cross-correlation or autocorrelation type measurement. The goal is to find a physical process that depends on the XUV intensity in a nonlinear way[5] and has a response time significantly shorter than the pulse duration, such that Equation 5.1 holds true, where $I_1(t)$ is the intensity profile of the first pulse, $I_2(t)$ is the intensity profile of the second pulse, τ is the time delay between the two pulses, and $I_{CC}(\tau)$ is the cross correlation signal, which might traditionally be something like a second harmonic generation signal.

$$I_{CC}(\tau) \propto \int_{-\infty}^{\infty} I_1(t) I_2(t-\tau)\, dt \qquad \text{Equation 5.1}$$

When the spectrum of the cross correlation signal is also measured, and if the nonlinearity of the medium is known, the pulse intensity and spectral phase as a function of time can both be determined in a technique known as frequency-resolved optical gating (FROG). As a first method of pulse characterization however, an intensity autocorrelation will be sufficient to measure the pulse duration. An additional advantage of this type of feedback is that at a fixed time delay it can also be used to optimize spatial overlap.

Experiments to date attempting to characterize XUV pulses in this fashion have used two-photon absorption / ionization as the nonlinear signal and detected the ion products using either a time-of-flight spectrometer (*153*, *158–161*) or reaction microscope (*141*), which detects electrons and ions in coincidence. A time-of-flight detector (TOF) was designed as the simpler and more versatile option, and it was installed at the target region. More details on planned autocorrelation experiments and considerations are given in Section 5.3, and the remainder of this section will describe the experimental design of the detector.

[5]With femtosecond pulses in the NIR linear interference can be used to find temporal overlap, however this will likely not be possible in the XUV because the period of 50 eV light is only 83 as and the timing jitter of the measurement may be on the same order.

For the TOF design, the two major driving goals were to (1) make the detector as modular and versatile as possible, and (2) be able to switch between TOF and absorption measurements without having to change the apparatus hardware significantly, ideally without even having to break vacuum. Regarding the former, a system was designed that could alternatively be used as an ion TOF spectrometer, an electron TOF spectrometer, and a velocity map imaging spectrometer. Regarding the latter, the system was designed such that it could be lowered into the focal region using a z-axis manipulator without colliding with any of the other diagnostics (e.g. the scintillator viewport). The resulting design is illustrated in Figure 5.14.

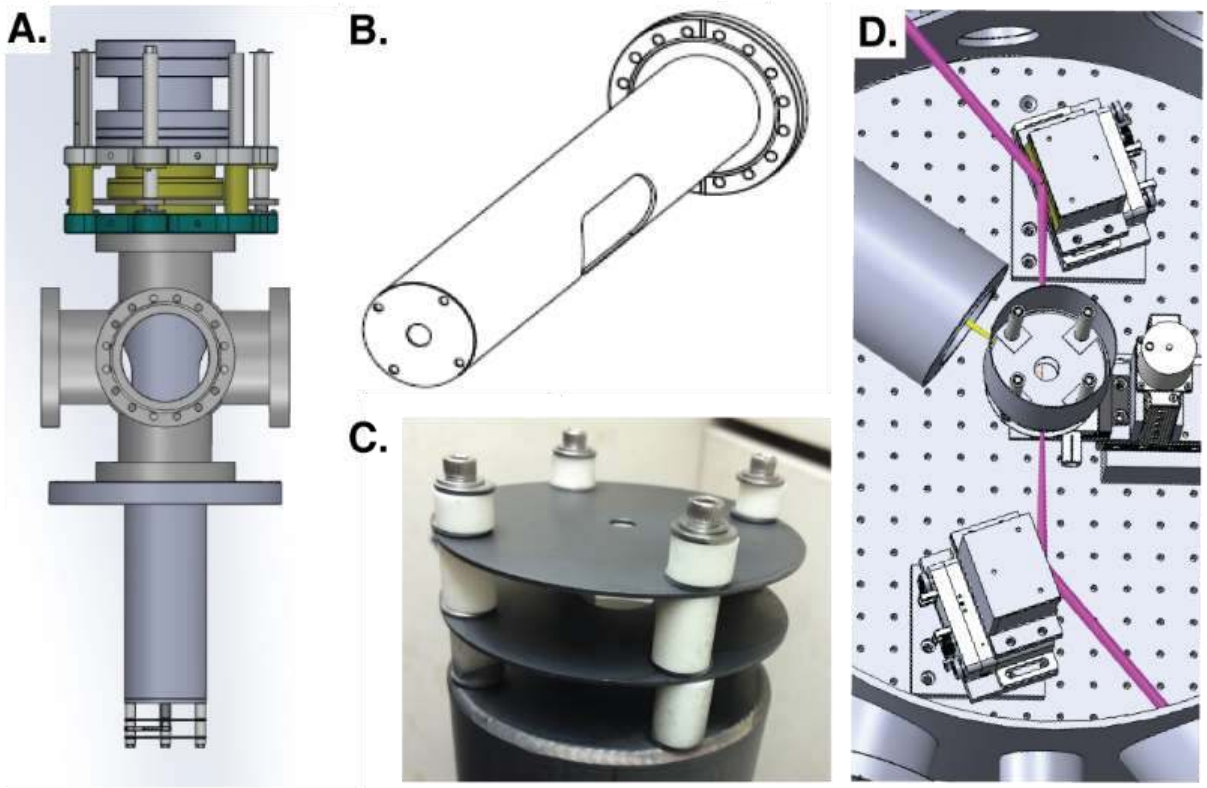

Figure 5.14. Time-of-flight spectrometer design. (**A**) Overview of the design as a whole. Inner portion, from bottom to top: plates to apply voltages around the interaction region, flight tube with mu metal sheath inside, which passes through 6-way cross and bellows to MCP detector mounted at the top. Outer portion, from bottom to top: 10" flange to connect to target chamber, 6-way cross for mounting electrical feedthroughs, a vacuum gauge, and turbo pump (flight tube has a cutout facing turbo pump for more efficient pumping), z-axis manipulator that allows the inner part to be raised and lowered, and MCP detector housing. (**B**) The inner part of the flight tube, showing cutouts for pumping efficiency. The top is a double-sided bored flange that attaches to the top of the axis z-manipulator. (**C**) Close up of the inner part of the TOF showing the modular three plate geometry with spacers. The plates and flight tube are coated with a graphite spray to increase the work function and reduce the generation of secondary electrons. (**D**) Top-down view of the target chamber with beam entering from top left, showing how the TOF can fit into the focal region without colliding with the scintillator viewport or stages.

As illustrated in the figure, the flight tube (with attached plates) can be raised and lowered into the sample area. The travel range of the z-axis manipulator is 4 inches, meaning that the TOF can be

moved well out of the way of the target area when not in use. A variety of plates were manufactured with different inner diameter holes, and an appropriate bottom plate will need to be selected that allows a gas nozzle mounted on the target stage to be inserted through the hole. The position of the gas nozzle can then be optimized in the X, Y, and Z directions.

Each plate is attached to the flight tube using long set screws and spacers. The bolts are screwed into four tapped holes in the top plate, which is welded onto the flight tube. Ceramic sheathes are used along the full length of the bolts, going through each plate, to electrically isolate each plate from the others. Washers and ceramic spacers are then used to set the distances, as can be seen in Figure 5.14C. For the most basic electron time-of-flight experiments the entire apparatus is kept field free, and a skimmer can be added if desired to improve the electron kinetic energy resolution. For use as an ion time-of-flight mass spectrometer on the other hand, it is necessary to accelerate the ions to the detector. In the simplest case a constant positive voltage is applied to the first plate (known as the source backing plate) and the ions are accelerated into the flight tube under a constant electric field, separating according to their mass to charge ratio (m/z). In this simple configuration the m/z resolution is limited by the initial kinetic energies of the ions (energy resolution) and their spatial spread (space resolution). However, both of these factors can be significantly improved by using a Wiley-McLaren design (*162*). In this scenario the drift tube is kept field free and an additional grid is installed between the flight tube and the ion source. The source backing plate and this grid are initially kept at the same positive voltage, so that no electric field is present at the ion position. A positive voltage pulse is then applied to the source backing plate, accelerating the ions through the grid and into the drift tube. The amplitude of the positive pulse can be used to improve spatial resolution and its delay with respect to the ionization event can be used to improve energy resolution. The principle is that ions generated closer to the source plate (or with velocity toward it) spend more time in the first acceleration region and catch up to the ions with opposite initial positions (or velocities).

How critical this will be will depend on the source beam size at the focus and the expected ion kinetic energies of the experiment. For simply distinguishing between e.g. Xe^+ and Xe^{2+} it will likely not be necessary. A basic calculation was performed in *Simion* to test this theory, using fixed voltages and cylindrical plates. The plates each had a 10 cm diameter and 2 cm diameter hole through the center, and were spaced 2 cm apart. The total distance from the first plate to the detector was set to 50 cm. This matches the current configuration of the TOF, but the plates could easily be replaced by grids, in the future. For the simulation, the first plate was set to +2.0 kV and the third (final) plate and flight tube to ground (field-free). The voltage of the second plate was varied between 0 and 2 kV to optimize the energy resolution on the detector. A mass spectrum for a Xe^+ and Xe^{2+} ion source was simulated, also including a dummy ion with one additional mass unit in each case, to see if these could theoretically be distinguished. The particle kinetic energies were uniformly distributed between 0.0 and 0.1 eV with isotropically distributed velocity directions, and the source position was set to a 3D Gaussian distribution with a standard deviation of 100 µm, significantly larger than the size of the ionization region actually expected. An optimum was found with the second plate voltage at +1.8 keV, and the resulting mass spectrum is shown in Figure 5.15, below.

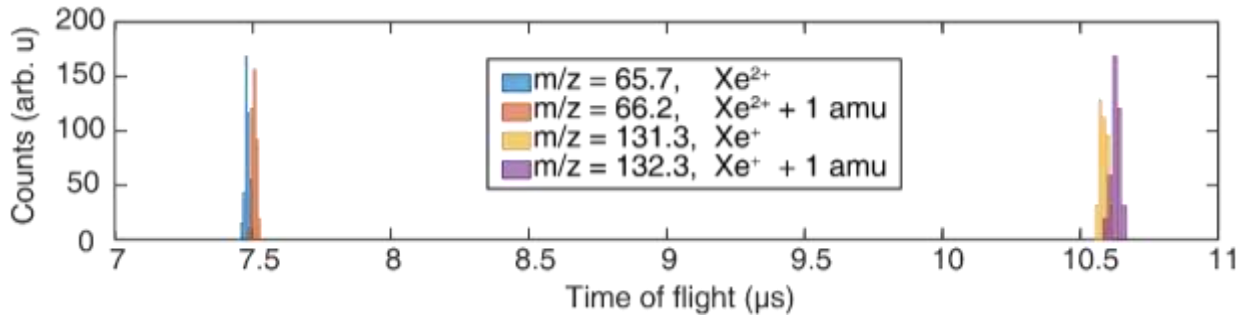

Figure 5.15. Simulated mass spectrum for the TOF configuration described in the text, where the ions had initial kinetic energy between 0 and 0.1 eV and a Gaussian spatial distribution with 100 μm standard deviation.

While the final geometry and voltages used may be changed, this highlights that the current design should easily be able to achieve good separation of singly and doubly ionized noble gas products for the most basic autocorrelation experiments (see section 5.2.1). As of the present, voltage supplies still need to be obtained for the TOF spectrometer and wired to the plates. An MCP detector and electronics have been obtained and are available. For future experiments, if kinetic energy resolution is desired, the TOF apparatus could easily be configured in a velocity map imaging design, and this could be tested in *Simion* as well.

5.2.3 Spectrum Measurement and Calibration

Once spatial and temporal overlap have been achieved, the main purpose of this apparatus is to perform transient absorption experiments. To this end it is important to ensure the XUV spectrometer is well aligned and characterized. The preliminary alignment and testing was performed at UC Berkeley, by coupling the spectrometer chamber to an existing XUV beamline. The distance from the XUV focus to the grating center was set to 35 cm to match the diffraction grating specifications. Pre-alignment was performed with a HeNe laser, using the zeroth, first, and second order diffraction. The zeroth order (reflection from the grating surface) was used to set the incidence angle to the specified 4.7° grazing incidence. The first and second order diffraction were then used to ensure the grating grooves were aligned vertically and that the grating surface was not vertically tilted. The vertical angle was used to correct the height of the first order diffraction, and the in-plane rotation of the grooves was used to correct the height of the second order diffraction, where these two degrees of freedom where iterated between until the alignment converged. The zeroth order diffraction was only used for the horizontal angle and not the vertical because it hits the vacuum chamber wall and cannot be measured at as far of a distance, leading to less precise alignment.

Once this pre-alignment was complete the system was pumped down to vacuum and an XUV source was introduced. Absorption spectra were measured for both neon and xenon gas, and are shown in Figure 5.16, with assignments.

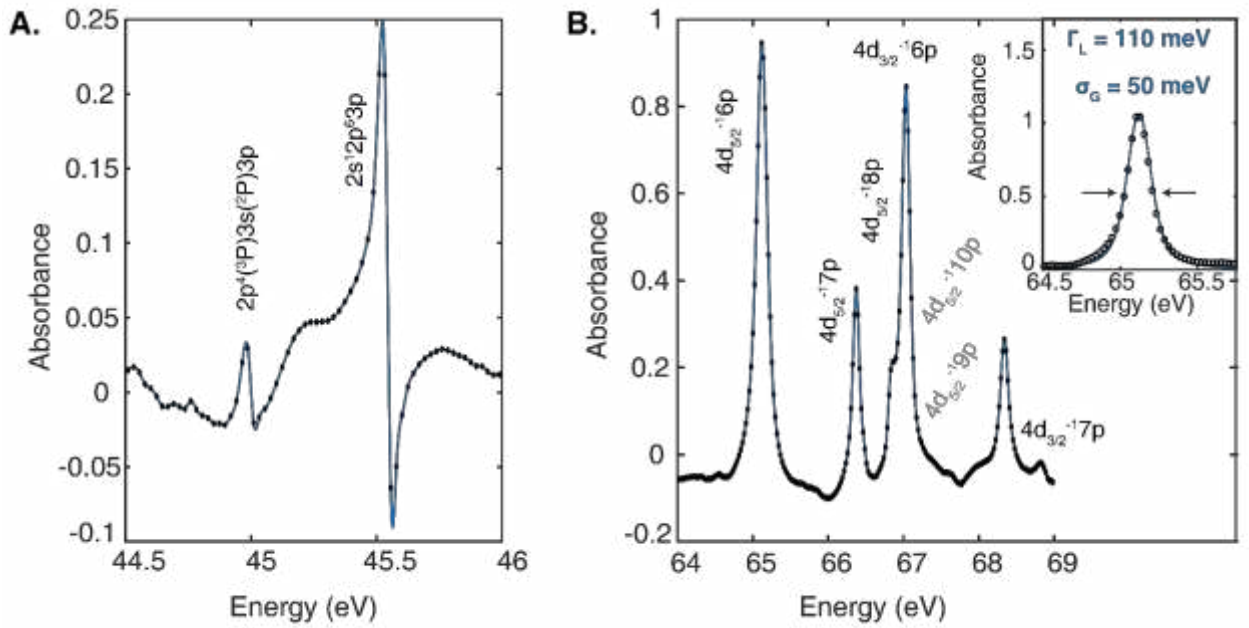

Figure 5.16. XUV absorption spectra of (**A**) neon and (**B**) xenon gas measured at UC Berkeley with the new spectrometer chamber coupled to an existing beamline. The black dots correspond to the measured data and the blue line is a smoothing spline shown as a guide to the eye. Assignments are taken from references (*105*) and (*163*), respectively. The inset in panel (**B**) shows a Voigt profile fit to the $4d_{5/2}^{-1}6p$ line in xenon to determine the experimental resolution. A Gaussian standard deviation of $\sigma = 50$ meV at 65 eV was obtained, using the natural Lorenzian linewidth of 110 meV of this absorption feature from the literature (*163*).

In each case the width of the absorption lineshape observed was dominated by the natural linewidth (lifetime broadening) of the feature. In order to determine the experimental energy resolution, an absorption line with a Lorenzian profile was selected that did not contain any overlapping features, for reliability of fitting. The xenon $4d_{5/2}^{-1}6p$ line was selected, and it was fit with a Voigt profile, which is a convolution of the natural Lorentzian linewidth $\Gamma_L = 110$ meV FWHM (*163*) and the Gaussian experimental energy resolution. The lineshape was best fit with a Gaussian experimental energy resolution with standard deviation $\sigma = 50$ meV. This value meets the desired $\Delta E/E < 0.001$ condition, and it was obtained immediately after pre-alignment of the grating with the HeNe laser, with no additional optimization needed. Even better resolution may be possible with the endstation focusing conditions of the apparatus at UCF, as described in Chapter 4.

As of this time the energy resolution has not been directly estimated at UCF. XUV light has however been coupled into the endstation, and the spatial and energy structure of the high harmonics has been measured with the spectrometer to help optimize the HHG process. The measured spectrum of an attosecond pulse train at UCF is shown in Figure 5.17, below.

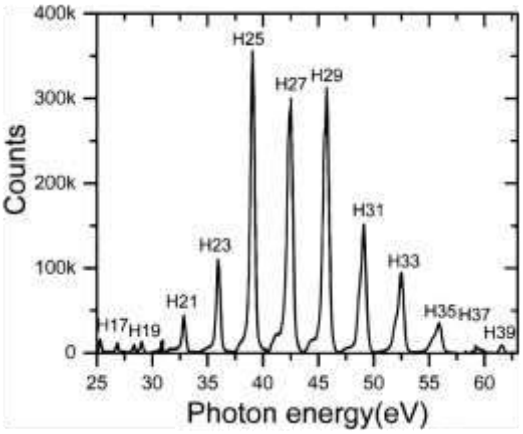

Figure 5.17. Measured high harmonic spectrum at UCF using the UC Berkeley endstation and spectrometer.

5.3 Experimental Plans and Outlook

For next steps on the apparatus, there are still several tasks to be done. Data acquisition programs must be written, or modified from existing programs at UC Berkeley. The sample platform for the experimental target area, which will hold the solid state samples, gas cell, scintillation screen, and gas cell / nozzle must be designed. The time-of-flight spectrometer must be installed and calibrated. An interferometric measurement of the timing stability should be performed and the timing jitter estimated at the target focus. The scintillator imaging system should be tested with an XUV source, and illumination needs to be installed such that it can be used for general sample imaging as well. The split mirror alignment stages may need to be replaced and new mounts designed if they prove too difficult to use or if spatial beam walk-off is an issue. The spectrometer alignment should be re-optimized using the XUV source at UCF, and inevitable problems and complications that will arise along the way must be dealt with. Once these final tasks have been accomplished, the pulses can be characterized and the first true measurements with the apparatus can be performed. A brief summary of the general plans in this regard are outlined in the below sections.

5.3.1 Pulse Characterization

Before timescales of physical processes can begin to be measured, it is important to know the temporal instrument response function of the measurement. Thus the first experiment to be performed on the apparatus should ideally be an autocorrelation measurement of the pulse duration. As described in Section 5.2.2, to perform such a measurement it is necessary to find a physical process that (a) depends nonlinearly on the XUV intensity and (b) has a response time shorter than the pulse duration. Multi-photon ionization has been demonstrated previously to work well for XUV autocorrelations at free-electron lasers (FELs) (*141*, *164*), and it is well known to depend non-linearly on the pulse duration. However, FEL pulses are typically tens of femtoseconds or longer in duration. Only a few autocorrelation measurements to date have been in the XUV using high harmonic sources, attempting to trace features with ~1 fs duration. In the two major

examples to date, separate XUV bursts in an attosecond pulse train were resolved using two-photon single ionization in helium (*160*), and an isolated attosecond pulse was characterized using two-photon direct double ionization in xenon (*158*). The latter was complicated however by overlapping Xe^{2+} signal due to sequential ionization (SI). While the SI signal displays interesting temporal evolution related to electron correlation in the system it is not well suited for an autocorrelation measurement because it persists well beyond the pulse duration.

In the ideal case there would only be one (non-linear) pathway to generation the ion of interest. E.g. if detecting a singly ionized product, the XUV photons should have an energy below the first ionization potential. If detecting a doubly ionized product, the XUV photon energy should be lower than the second ionization potential, such that sequential ionization cannot produce the same product. This idea can be extended to triply and higher ionized products as well, however the results become quite complicated and different SI and non-SI pathways have to be disentangled via intensity dependence (*165*, *166*). At the current time we suggest to use double ionization in helium for the first pulse characterization experiment. He^{2+} can be produced only via a direct double ionization process (no SI pathway) as long as the photon energy is below 54.4 eV, the second ionization energy of helium, and the intensity is not so high that three-photon absorption comes into play. Some of the energy levels and allowed XUV transitions in helium are shown in Figure 5.18, below. The schematic in this figure is not all inclusive, and other multiphoton absorption / ionization processes should be taken into account depending on the intensity of the experiment.

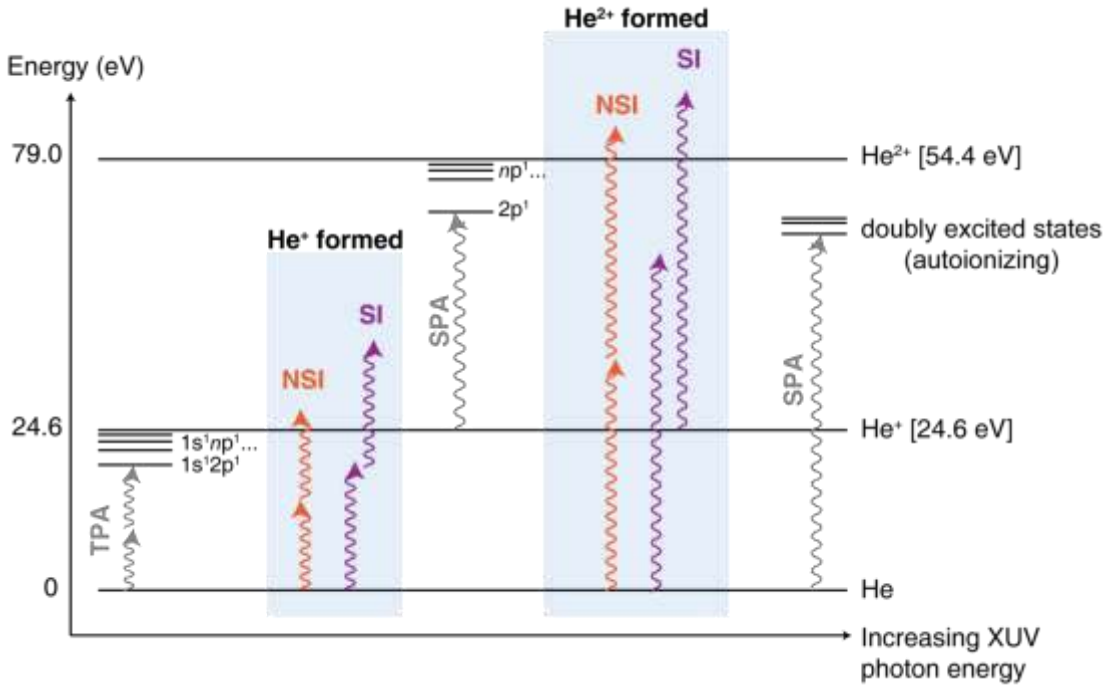

Figure 5.18. Some of the possible absorption and ionization processes that can occur with XUV radiation in helium. SPA = single-photon absorption, TPA = two-photon absorption, SI = sequential ionization, NSI = non-sequential ionization.

For more complex cases, where detecting the doubly-charged ion yield is insufficient to disentangle the different processes and obtain a clean autocorrelation signal, it may be possible to use characteristic photoemission or fluorescence energies. In krypton, for instance, two-photon absorption can be used to access the inner-shell excited $3d_{5/2}^{-1}ns^1$ Rydberg states around 90 eV (*167*). The core-hole excitations can then decay via either Auger decay or fluorescence, the former of which could certainly be detected using the TOF spectrometer and the latter or which may be detectable depending on how intense and directional the resulting fluorescence is – any light that is captured by the second ellipsoidal mirror will be sent to the XUV spectrometer. The resulting discrete energy signals could ideally then be separated from any continuous background due to above threshold ionization (in the case of electrons) or the static XUV spectrum (in the case of fluorescence).

5.3.2 Next Proposed Measurements and Future Directions

Once the XUV pulses have been characterized and their duration determined, a whole host of attosecond-pump attosecond-probe measurements will be possible, revealing the ultrafast response of atoms to XUV radiation. Fundamental processes in the gas phase, such as Auger decay of core-excited states and XUV multiphoton ionization mechanisms can be studied. Dynamics due to electron correlation can be followed immediately after photoexcitation, without the complicating overlap of a strong NIR field. The ultimate goal of the project and collaboration is to then bring the attosecond-pump attosecond-probe technique to the solid state, to understand how fast correlation-driven phenomena can be manipulated for device applications. Preliminary experiments could focus on processes that bridge the gap between correlation phenomena in atoms and solids, such as interatomic Coulomb decay in molecules, and allow some fundamental understanding built up. Eventually, the hope is to transition the technology and understanding developed to strongly correlated phenomena in materials, such as insulator-to-metal transitions, superconductivity, and colossal magnetoresistance.

References

1. T. M. Nordlund, in *Topics in Fluorescence Spectroscopy, Volume 1*, J. R. Lakowicz, Ed. (Plenum Press, New York, 2002), pp. 183–260.
2. P. M. Paul *et al.*, Observation of a Train of Attosecond Pulses from High Harmonic Generation. *Science*. **292**, 1689–1692 (2001).
3. M. Hentschel *et al.*, Attosecond metrology. *Nature*. **414**, 509–513 (2001).
4. J. Li *et al.*, 53-attosecond X-ray pulses reach the carbon K-edge. *Nat. Commun.* **8**, 186 (2017).
5. G. D. Dickenson *et al.*, Fundamental vibration of molecular hydrogen. *Phys. Rev. Lett.* **110**, 193601 (2013).
6. K. C. Kulander, K. J. Schafer, J. L. Krause, in *Super-Intense Laser-Atom Physics*, K. L'Huillier, A., Piraux, Bernard, Rzazewski, Ed. (1993), vol. 316, p. 95.
7. P. Corkum, Plasma perspective on strong field multiphoton ionization. *Phys. Rev. Lett.* **71**, 1994–1997 (1993).
8. M. Lewenstein, P. Balcou, M. Y. Ivanov, A. L'Huillier, P. B. Corkum, Theory of high-harmonic generation by low-frequency laser fields. *Phys. Rev. A*. **49**, 2117–2132 (1994).
9. T. Popmintchev *et al.*, Phase matching of high harmonic generation in the soft and hard X-ray regions of the spectrum. *Proc. Natl. Acad. Sci. U. S. A.* **106**, 10516–10521 (2009).
10. I. P. Christov, M. M. Murnane, H. C. Kapteyn, High-Harmonic Generation of Attosecond Pulses in the "Single-Cycle" Regime. *Phys. Rev. Lett.* **78**, 1251–1254 (1997).
11. M. J. Abel *et al.*, Isolated attosecond pulses from ionization gating of high-harmonic emission. *Chem. Phys.* **366**, 9–14 (2009).
12. P. B. Corkum, N. H. Burnett, M. Y. Ivanov, Subfemtosecond pulses. *Opt. Lett.* **19**, 1870–1872 (1994).
13. O. Tcherbakoff, E. Mével, D. Descamps, J. Plumridge, E. Constant, Time-gated high-order harmonic generation. *Phys. Rev. A*. **68**, 43804 (2003).
14. G. Sansone *et al.*, Isolated Single-Cycle Attosecond Pulses. *Science*. **314**, 443–446 (2006).
15. T. Pfeifer, L. Gallmann, M. J. Abel, D. M. Neumark, S. R. Leone, Single attosecond pulse generation in the multicycle-driver regime by adding a weak second-harmonic field. *Opt. Lett.* **31**, 975–977 (2006).
16. H. Mashiko *et al.*, Double Optical Gating of High-Order Harmonic Generation with Carrier-Envelope Phase Stabilized Lasers. *Phys. Rev. Lett.* **100**, 103906 (2008).
17. H. Vincenti, F. Quéré, Attosecond lighthouses: How to use spatiotemporally coupled light fields to generate isolated attosecond pulses. *Phys. Rev. Lett.* **108**, 113904 (2012).
18. T. J. Hammond, G. G. Brown, K. T. Kim, D. M. Villeneuve, P. B. Corkum, Attosecond pulses measured from the attosecond lighthouse. *Nat. Photonics*. **10**, 171–176 (2016).
19. E. Goulielmakis *et al.*, Real-time observation of valence electron motion. *Nature*. **466**, 739–743 (2010).
20. M. Schultze *et al.*, Attosecond band-gap dynamics in silicon. *Science*. **346**, 1348–1352 (2014).
21. M. Schultze *et al.*, Delay in photoemission. *Science*. **328**, 1658–1662 (2010).
22. P. M. Kraus *et al.*, Measurement and laser control of attosecond charge migration in ionized iodoacetylene. *Science*. **350**, 1525–1529 (2015).
23. J. Itatani *et al.*, Tomographic imaging of molecular orbitals. *Nature*. **432**, 867–871 (2004).

24. T. Ding *et al.*, Time-resolved four-wave-mixing spectroscopy for inner-valence transitions. *Opt. Lett.* **41**, 709–712 (2016).
25. W. Cao, E. R. Warrick, A. Fidler, S. R. Leone, D. M. Neumark, Near-resonant four-wave mixing of attosecond extreme-ultraviolet pulses with near-infrared pulses in neon: Detection of electronic coherences. *Phys. Rev. A*. **94**, 21802 (2016).
26. P. Eckle *et al.*, Attosecond Ionization and Tunneling Delay Time Measurements in Helium. *Science*. **322**, 1525–1529 (2008).
27. R. Hoffmann, *Solids and surfaces: a chemist's view of bonding in extended structures* (VCH Publishers, New York, 1988).
28. F. Bloch, Über die Quantenmechanik der Elektronen in Kristallgittern. *Zeitschrift für Phys.* **52**, 555–600 (1929).
29. C. Kittel, *Introduction to Solid State Physics* (Wiley, New York, ed. 5th, 1988).
30. F. de Groot, A. Kotani, *Core level spectroscopy of solids* (CRC Press, New York, 2008).
31. U. Fano, Effects of Configuration Interaction on Intensities and Phase Shifts. *Phys. Rev.* **124**, 1866–1878 (1961).
32. L. C. Davis, L. A. Feldkamp, Interaction of many discrete states with many continua. *Phys. Rev. B*. **15**, 2961–2969 (1977).
33. R. Huber *et al.*, How many-particle interactions develop after ultrafast excitation of an electron-hole plasma. *Nature*. **414**, 286–289 (2001).
34. S. K. Sundaram, E. Mazur, Inducing and probing non-thermal transitions in semiconductors using femtosecond laser pulses. *Nat. Mater.* **1**, 217–224 (2002).
35. Z. Yang, C. Ko, S. Ramanathan, Oxide Electronics Utilizing Ultrafast Metal-Insulator Transitions. *Annu. Rev. Mater. Res.* **41**, 337–367 (2011).
36. N. Mott, M. Imada, A. Fujimori, Y. Tokura, Metal-insulator transitions. *Rev. Mod. Phys.* **70** (1998), pp. 1039–1263.
37. A. Cavalleri, T. Dekorsy, H. H. W. Chong, J. C. Kieffer, R. W. Schoenlein, Evidence for a structurally-driven insulator-to-metal transition in VO_2: A view from the ultrafast timescale. *Phys. Rev. B*. **70**, 161102 (2004).
38. D. Wegkamp *et al.*, Instantaneous band gap collapse in photoexcited monoclinic VO_2 due to photocarrier doping. *Phys. Rev. Lett.* **113**, 216401 (2014).
39. B. T. O'Callahan *et al.*, Inhomogeneity of the ultrafast insulator-to-metal transition dynamics of VO_2. *Nat. Commun.* **6**, 6849 (2015).
40. D. Wegkamp, J. Stähler, Ultrafast dynamics during the photoinduced phase transition in VO_2. *Prog. Surf. Sci.* **90**, 464–502 (2015).
41. R. E. Peierls, *More surprises in theoretical physics* (Princeton University Press, 1991).
42. A. Mansingh, R. Singh, M. Sayer, Dielectric behaviour of vanadium dioxide. *Phys. Status Solidi*. **49**, 773–779 (1978).
43. C. N. Berglund, H. J. Guggenheim, Electronic properties of VO_2 near the semiconductor-metal transition. *Phys. Rev.* **185**, 1022–1033 (1969).
44. A. Pergament, Metal-insulator transition: the Mott criterion and coherence length. *J. Phys. Condens. Matter*. **15**, 3217–3223 (2003).
45. K. Nasu, *Photoinduced Phase Transitions* (World Scientific Publishing Co. Pte. Ltd., New York, 2004).
46. D. N. Basov, R. D. Averitt, D. van der Marel, M. Dressel, K. Haule, Electrodynamics of correlated electron materials. *Rev. Mod. Phys.* **83**, 471 (2011).
47. Y. Tokura, N. Nagaosa, Orbital Physics in Transition-Metal Oxides. *Science*. **288**, 462–

468 (2000).
48. A. J. Millis, B. I. Shraiman, R. Mueller, Dynamic Jahn-Teller Effect and Colossal Magnetoresistance in $La_{1-x}Sr_xMnO_3$. *Phys. Rev. Lett.* **77**, 175–178 (1996).
49. J. G. Bednorz, K. A. Müller, Possible high Tc superconductivity in the Ba−La−Cu−O system. *Zeit. Fur. Phys.* **64**, 189–193 (1986).
50. F. J. Morin, Oxides which show a metal-to-insulator transition at the neel temperature. *Phys. Rev. Lett.* **3**, 34–36 (1959).
51. M. Imada, A. Fujimori, Y. Tokura, Metal-insulator transitions. *Rev. Mod. Phys.* **70**, 1039–1263 (1998).
52. H. T. Kim *et al.*, Mechanism and observation of Mott transition in VO2-based two- and three-terminal devices. *New J. Phys.* **6** (2004), doi:10.1088/1367-2630/6/1/052.
53. T. Driscoll, H. T. Kim, B. G. Chae, M. Di Ventra, D. N. Basov, Phase-transition driven memristive system. *Appl. Phys. Lett.* **95**, 1–3 (2009).
54. K. Ramasesha, S. R. Leone, D. M. Neumark, Real-time probing of electron dynamics using attosecond time-resolved spectroscopy. *Annu. Rev. Phys. Chem.* **67**, 41–63 (2016).
55. G. Farkas, C. Tóth, Proposal for attosecond light pulse generation using laser induced multiple-harmonic conversion processes in rare gases. *Phys. Lett. A*. **168**, 447–450 (1992).
56. M. Ferray *et al.*, Multiple-harmonic conversion of 1064 nm radiation in rare gases. *J. Phys. B*. **21**, L31–L35 (1988).
57. F. Krausz, M. Ivanov, Attosecond physics. *Rev. Mod. Phys.* **81**, 163–234 (2009).
58. O. Smirnova *et al.*, High harmonic interferometry of multi-electron dynamics in molecules. *Nature*. **460**, 972–977 (2009).
59. W. Li *et al.*, Time-Resolved Dynamics in N_2O_4 Probed Using High Harmonic Generation. *Science*. **322**, 1207–1211 (2008).
60. L. Nugent-Glandorf, M. Scheer, D. A. Samuels, V. M. Bierbaum, S. R. Leone, Ultrafast photodissociation of Br_2: Laser-generated high-harmonic soft x-ray probing of the transient photoelectron spectra and ionization cross sections. *J. Chem. Phys.* **117**, 6108 (2002).
61. M. F. Jager *et al.*, *Proc. Natl. Acad. Sci. U. S. A.*, in press.
62. M. Miranda *et al.*, Characterization of broadband few-cycle laser pulses with the d-scan technique. *Opt. Express*. **20**, 18732 (2012).
63. J. Nag, The solid-solid phase transition in vanadium dioxide thin films: synthesis, physics and applications (Ph.D. dissertation, Vanderbilt University, 2011) (available at http://etd.library.vanderbilt.edu/available/etd-04202011-182358/).
64. A. Walsh, J. L. F. Da Silva, S. H. Wei, Origins of band-gap renormalization in degenerately doped semiconductors. *Phys. Rev. B*. **78**, 1–5 (2008).
65. M. Chini *et al.*, Delay control in attosecond pump-probe experiments. *Opt. Express*. **17**, 21459 (2009).
66. M. Sabbar *et al.*, Combining attosecond XUV pulses with coincidence spectroscopy. *Rev. Sci. Instrum.* **85** (2014), doi:10.1063/1.4898017.
67. A. Blättermann *et al.*, In situ characterization of few-cycle laser pulses in transient absorption spectroscopy. *Opt. Lett.* **40**, 3464 (2015).
68. J. Nag, R. F. Haglund Jr, Synthesis of vanadium dioxide thin films and nanoparticles. *J. Phys. Condens. Matter*. **20**, 264016 (2008).
69. M. Zürch *et al.*, *ArXiv*, in press (available at http://arxiv.org/abs/1702.03822).
70. J. C. Rakotoniaina *et al.*, The Thermochromic Vanadium Dioxide: I. Role of Stresses and

Substitution on Switching Properties. *J. Solid State Chem.* **103**, 81–94 (1993).
71. G. V. Chandrashekhar, H. L. C. Barros, J. M. Honig, Heat capacity of VO_2 single crystals. *Mater. Res. Bull.* **8**, 369–374 (1973).
72. G. Ziegler, J. Heinrich, G. Wötting, Relationships between processing, microstructure and properties of dense and reaction-bonded silicon nitride. *J. Mater. Sci.* **22**, 3041–3086 (1987).
73. D. R. Lide, in *CRC Handbook of Chemistry and Physics* (CRC Press, Boca Raton, Florida, ed. 84, 2003).
74. X. Zhang, C. P. Grigoropoulos, Thermal conductivity and diffusivity of free-standing silicon nitride thin films. *Rev. Sci. Instrum.* **66**, 1115–1120 (1995).
75. C. J. Glassbrenner, G. A. Slack, Thermal Conductivity of Silicon and Germanium from 3°K to the Melting Point. *Phys. Rev.* **134**, A1058–A1069 (1964).
76. F. Guinneton, L. Sauques, J.-C. Valmalette, F. Cros, J.-R. Gavarri, Optimized infrared switching properties in thermochromic vanadium dioxide thin films: role of deposition process and microstructure. *Thin Solid Films*. **446**, 287–295 (2004).
77. P. J. Van Zwol *et al.*, *ArXiv*, in press.
78. P. J. Timans, Emissivity of silicon at elevated temperatures. *J. Appl. Phys.* **74**, 6353–6364 (1993).
79. A. Cavalleri *et al.*, Picosecond soft x-ray absorption measurement of the photoinduced insulator-to-metal transition in VO_2. *Phys. Rev. B*. **69**, 153106 (2004).
80. H. Wen *et al.*, Structural and electronic recovery pathways of a photoexcited ultrathin VO_2 film. *Phys. Rev. B*. **88**, 165424 (2013).
81. Z. Yang, C. Ko, S. Ramanathan, Oxide electronics utilizing ultrafast metal-insulator transitions. *Annu. Rev. Mater. Res.* **41**, 337–367 (2011).
82. F. Krausz, M. I. Stockman, Attosecond metrology: from electron capture to future signal processing. *Nat. Photonics*. **8**, 205–213 (2014).
83. M. Lorenz *et al.*, The 2016 oxide electronic materials and oxide interfaces roadmap. *J. Phys. D. Appl. Phys.* **49**, 433001 (2016).
84. A. L. Cavalieri *et al.*, Attosecond spectroscopy in condensed matter. *Nature*. **449**, 1029–1032 (2007).
85. M. Schultze *et al.*, Controlling dielectrics with the electric field of light. *Nature*. **493**, 75–78 (2013).
86. G. Vampa *et al.*, Linking high harmonics from gases and solids. *Nature*. **522**, 462–464 (2015).
87. H. Mashiko, K. Oguri, T. Yamaguchi, A. Suda, H. Gotoh, Petahertz optical drive with wide-bandgap semiconductor. *Nat. Phys.* **12**, 741–745 (2016).
88. Z. Tao *et al.*, Direct time-domain observation of attosecond final-state lifetimes in photoemission from solids. *Science*. **353**, 62–67 (2016).
89. M. Lucchini *et al.*, Attosecond dynamical Franz-Keldysh effect in polycrystalline diamond. *Science*. **353**, 916–919 (2016).
90. R. M. Wentzcovitch, W. W. Schulz, P. B. Allen, VO_2: Peierls or Mott-Hubbard? A view from band theory. *Phys. Rev. Lett.* **72**, 3389–3392 (1994).
91. C. Weber *et al.*, Vanadium dioxide: A Peierls-Mott insulator stable against disorder. *Phys. Rev. Lett.* **108**, 256402 (2012).
92. S. Biermann, A. Poteryaev, A. I. Lichtenstein, A. Georges, Dynamical singlets and correlation-assisted Peierls transition in VO_2. *Phys. Rev. Lett.* **94**, 26404 (2005).

93. T. J. Huffman *et al.*, Insulating phases of vanadium dioxide are Mott-Hubbard insulators. *Phys. Rev. B*. **95**, 75125 (2017).
94. J. D. Budai *et al.*, Metallization of vanadium dioxide driven by large phonon entropy. *Nature*. **515**, 535–539 (2014).
95. A. X. Gray *et al.*, Correlation-driven insulator-metal transition in near-ideal vanadium dioxide films. *Phys. Rev. Lett.* **116**, 116403 (2016).
96. N. B. Aetukuri *et al.*, Control of the metal-insulator transition in vanadium dioxide by modifying orbital occupancy. *Nat Phys*. **9**, 661–666 (2013).
97. M. F. Becker *et al.*, Femtosecond laser excitation of the semiconductor-metal phase transition in VO_2. *Appl. Phys. Lett.* **65**, 1507–1509 (1994).
98. A. Cavalleri *et al.*, Femtosecond Structural Dynamics in VO_2 during an Ultrafast Solid-Solid Phase Transition. *Phys. Rev. Lett.* **87**, 237401 (2001).
99. A. Cavalleri *et al.*, Band-selective measurements of electron dynamics in VO_2 using femtosecond near-edge X-ray absorption. *Phys. Rev. Lett.* **95**, 67405 (2005).
100. S. Wall *et al.*, Ultrafast changes in lattice symmetry probed by coherent phonons in VO_2. *Nat. Commun.* **3**, 721 (2010).
101. P. Baum, D.-S. Yang, A. H. Zewail, 4D visualization of transitional structures in phase transformations by electron diffraction. *Science (80-.).* **318**, 788–792 (2007).
102. V. R. Morrison *et al.*, A photoinduced metal-like phase of monoclinic VO_2 revealed by ultrafast electron diffraction. *Science*. **346**, 445–8 (2014).
103. C. Kübler *et al.*, Coherent structural dynamics and electronic correlations during an ultrafast insulator-to-metal phase transition in VO_2. *Phys. Rev. Lett.* **99**, 116401 (2007).
104. S. Suga *et al.*, ~8 keV photoemission of the metal-insulator transition system VO_2. *New J. Phys.* **11**, 103015 (2009).
105. K. Schulz *et al.*, High-resolution experimental and theoretical study of singly and doubly excited resonances in ground-state photoionization of neon. *Phys. Rev. A*. **54**, 3095–3112 (1996).
106. S. Shin *et al.*, Vacuum-ultraviolet reflectance and photoemission study of the metal-insulator phase transitions in VO_2, V_6O_{13}, and V_2O_3. *Phys. Rev. B*. **41**, 4993–5009 (1990).
107. B. L. Henke, E. M. Gullikson, J. C. Davis, X-Ray interactions: photoabsorption, scattering, transmission, and reflection at E = 50-30,000 eV, Z = 1-92. *At. Data Nucl. Data Tables*. **54**, 181 (1993).
108. F. De Groot, Multiplet effects in X-ray spectroscopy. *Coord. Chem. Rev.* **249**, 31–63 (2005).
109. E. Stavitski, F. M. F. de Groot, The CTM4XAS program for EELS and XAS spectral shape analysis of transition metal L edges. *Micron*. **41**, 687–694 (2010).
110. T. Kaurila, J. Väyrynen, M. Isokallio, Experimental study of resonant photoemission in the metals V, Cr, Mn and Co. *J. Phys. Condens. Matter*. **9**, 6533–6542 (1999).
111. M. Taguchi, T. Uozumi, A. Kotani, Theory of X-ray photoemission and X-ray emission spectra in Mn compounds. *J. Phys. Soc. Japan*. **66**, 247–256 (1997).
112. R. Zimmermann, R. Claessen, F. Reinert, P. Steiner, S. Hüfner, Strong hybridization in vanadium oxides: evidence from photoemission and absorption spectroscopy. *J. Phys. Condens. Matter*. **10**, 5697–5716 (1999).
113. M. W. Haverkort *et al.*, Orbital-assisted metal-insulator transition in VO_2. *Phys. Rev. Lett.* **95**, 196404 (2005).
114. R. Zimmermann *et al.*, Electronic structure of 3d-transition-metal oxides: on-site Coulomb

repulsion versus covalency. *J. Phys. Condens. Matter*. **11**, 1657–1682 (1999).
115. S. D. Bader *et al.*, Autoionization in bulk, multilayer, and monolayer Cr. *Phys. Rev. B*. **33**, 3636–3643 (1986).
116. L. C. Davis, L. A. Feldkamp, $M_{2,3}$ Spectrum of Atomic Mn. *Phys. Rev. A*. **17**, 2012–2022 (2012).
117. G. Van Der Laan, $M_{2,3}$ absorption spectroscopy of 3d transition-metal compounds. *J. Phys. Condens. Matter*. **3**, 7443–7454 (1991).
118. S. Sayyad, M. Eckstein, Slowdown of the Electronic Relaxation Close to the Mott Transition. *Phys. Rev. Lett.* **117**, 96403 (2016).
119. N. F. Mott, On the transition to metallic conduction in semiconductors. *Can. J. Phys.* **34**, 1356–1368 (1956).
120. Y. Li, X. Luo, H. Kröger, Bound states and critical behavior of the Yukawa potential. *Sci. China, Ser. G Phys. Astron.* **49**, 60–71 (2006).
121. X. Yuan, W. Zhang, P. Zhang, Hole-lattice coupling and photoinduced insulator-metal transition in VO_2. *Phys. Rev. B*. **88**, 35119 (2013).
122. X. Wu *et al.*, Influence of infrared optical properties by transformation of the crystal structure in Al-doped vanadium dioxide films. *Opt. Mater. Express*. **6**, 3500–3506 (2016).
123. H. J. Zeiger *et al.*, Theory for displacive excitation of coherent phonons. *Phys. Rev. B*. **45**, 768–778 (1992).
124. G. Lantz *et al.*, Ultrafast evolution and transient phases of the prototype out-of-equilibrium Mott-Hubbard material V_2O_3. *Nat. Commun.* **8**, 13917 (2016).
125. S. A. Dönges *et al.*, Ultrafast nanoimaging of the photoinduced phase transition dynamics in VO_2. *Nano Lett.* **16**, 3029–3035 (2016).
126. P. Schilbe, Raman scattering in VO_2. *Phys. B*. **316–317**, 600–602 (2002).
127. X. Wu *et al.*, THz transmittance and electrical properties tuning across IMT in vanadium dioxide films by Al doping. *ACS Appl. Mater. Interfaces*. **8**, 11842–11850 (2016).
128. M. Gurvitch *et al.*, VO_2 films with strong semiconductor to metal phase transition prepared by the precursor oxidation process. *J. Appl. Phys.* **102**, 33504 (2007).
129. J. Y. Suh, R. Lopez, L. C. Feldman, R. F. Haglund, Semiconductor to metal phase transition in the nucleation and growth of VO_2 nanoparticles and thin films. *J. Appl. Phys.* **96**, 1209–1213 (2004).
130. K. Appavoo *et al.*, Role of Defects in the Phase Transition of VO_2 Nanoparticles Probed by Plasmon Resonance Spectroscopy. *Nano Lett.* **12**, 780–786 (2012).
131. D. Brassard, S. Fourmaux, M. Jean-Jacques, J. C. Kieffer, M. A. El Khakani, Grain size effect on the semiconductor-metal phase transition characteristics of magnetron-sputtered VO_2 thin films. *Appl. Phys. Lett.* **87**, 51910 (2005).
132. C. Ott *et al.*, Lorentz meets Fano in spectral line shapes: a universal phase and its laser control. *Science*. **340**, 716–720 (2013).
133. S. Wall *et al.*, Tracking the evolution of electronic and structural properties of VO_2 during the ultrafast photoinduced insulator-metal transition. *Phys. Rev. B*. **87**, 115126 (2013).
134. F. Ferrari *et al.*, High-energy isolated attosecond pulses generated by above-saturation few-cycle fields. *Nat. Photonics*. **4**, 875–879 (2010).
135. E. Goulielmakis *et al.*, Single-cycle nonlinear optics. *Science*. **320**, 1614–7 (2008).
136. X. Feng *et al.*, Generation of isolated attosecond pulses with 20 to 28 femtosecond lasers. *Phys. Rev. Lett.* **103**, 183901 (2009).
137. Y. Wu *et al.*, Generation of high-flux attosecond extreme ultraviolet continuum with a 10

TW laser. *Appl. Phys. Lett.* **102**, 201104 (2013).
138. B. E. Schmidt *et al.*, Frequency domain optical parametric amplification. *Nat. Commun.* **5**, 3643 (2014).
139. M. Sanchez del Rio, N. Canestrari, F. Jiang, F. Cerrina, *SHADOW3* : a new version of the synchrotron X-ray optics modelling package. *J. Synchrotron Radiat.* **18**, 708–716 (2011).
140. F. Cerrina, M. Sanchez del Rio, in *Handbook of Optics (volume V)*, M. Bass, Ed. (McGraw-Hill, New York, ed. 3, 2009).
141. Y. H. Jiang *et al.*, Temporal coherence effects in multiple ionization of N_2 via XUV pump-probe autocorrelation. *Phys. Rev. A*. **82**, 41403 (2010).
142. Y. H. Jiang *et al.*, *Phys. Rev. A*, in press, doi:10.1103/PhysRevA.81.051402.
143. C. Ott *et al.*, Reconstruction and control of a time-dependent two-electron wave packet. *Nature*. **516**, 374–378 (2014).
144. A. M. Heins, C. Guo, Spatial mode cleaning in radically asymmetric strongly focused laser beams. *Appl. Phys. B*, 317–325 (2013).
145. F. Barkusky, A. Bayer, S. Döring, P. Grossmann, K. Mann, Damage threshold measurements on EUV optics using focused radiation from a table-top laser produced plasma source. *Opt. Express*. **18**, 4346–4355 (2010).
146. T. Harada, K. Takahashi, H. Sakuma, A. Osyczka, Optimum design of a grazing-incidence flat-field spectrograph with a spherical varied-line-space grating. *Appl. Opt.* **38**, 2743–2748 (1999).
147. T. Kita, T. Harada, N. Nakano, H. Kuroda, Mechanically ruled aberration-corrected concave gratings for a flat-field grazing-incidence spectrograph. *Appl. Opt.* **22**, 512–513 (1983).
148. N. Nakano, H. Kuroda, T. Kita, T. Harada, Development of a flat-field grazing-incidence XUV spectrometer and its application in picosecond XUV spectroscopy. *Appl. Opt.* **23**, 2386–2392 (1984).
149. T. Namioka, Theory of the Concave Grating. I. *J. Opt. Soc. Am.* **49**, 446–460 (1959).
150. T. Namioka, Theory of the Concave Grating. III. Seya-Namioka Monochromator. *J. Opt. Soc. Am.* **49**, 951–961 (1959).
151. Q. Zhang *et al.*, Suppression of driving laser in high harmonic generation with a microchannel plate. *Opt. Lett.* **39**, 3670–3673 (2014).
152. H. Mashiko, A. Suda, K. Midorikawa, Focusing coherent soft-x-ray radiation to a micrometer spot size with an intensity of 10^{14} W/cm^2. *Opt. Lett.* **29**, 1927–1929 (2004).
153. B. Manschwetus *et al.*, Two-photon double ionization of neon using an intense attosecond pulse train. *Phys. Rev. A*. **93**, 61402 (2016).
154. C. Valentin *et al.*, Imaging and quality assessment of high-harmonic focal spots. *Opt. Lett.* **28**, 1049–1051 (2003).
155. M. Moszyński, T. Ludziejewski, D. Wolski, W. Klamra, L. O. Norlin, Properties of the YAG:Ce scintillator. *Nucl. Instruments Methods Phys. Res. Sect. A Accel. Spectrometers, Detect. Assoc. Equip.* **345**, 461–467 (1994).
156. M. Nikl, Scintillation detectors for x-rays. *Meas. Sci. Technol.* **17**, R37–R54 (2006).
157. C. R. Ott, thesis, University of Heidelberg (2012).
158. P. Tzallas, E. Skantzakis, L. A. A. Nikolopoulos, G. D. Tsakiris, D. Charalambidis, Extreme-ultraviolet pump-probe studies of one femtosecond scale electron dynamics. *Nat. Phys.* **7**, 781–784 (2011).
159. P. Tzallas, E. Skantzakis, D. Charalambidis, Direct two-XUV-photon double ionization in

xenon. *J. Phys. B*. **45**, 74007 (2012).
160. P. Tzallas, D. Charalambidis, N. a Papadogiannis, K. Witte, G. D. Tsakiris, Direct observation of attosecond light bunching. *Nature*. **426**, 267–271 (2003).
161. E. J. Takahashi, P. Lan, O. D. Mücke, Y. Nabekawa, K. Midorikawa, Attosecond nonlinear optics using gigawatt-scale isolated attosecond pulses. *Nat. Commun.* **4**, 3691 (2013).
162. W. C. Wiley, I. H. McLaren, Time-of-Flight Mass Spectrometer with Improved Resolution. *Rev. Sci. Instrum.* **26**, 1150–1157 (1955).
163. O.-P. Sairanen, a. Kivimäki, E. Nõmmiste, H. Aksela, S. Aksela, High-resolution pre-edge structure in the inner-shell ionization threshold region of rare gases Xe, Kr, and Ar. *Phys. Rev. A*. **54**, 2834–2839 (1996).
164. R. Mitzner *et al.*, Direct autocorrelation of soft-x-ray free-electron-laser pulses by time-resolved two-photon double ionization of He. *Phys. Rev. A*. **80**, 25402 (2009).
165. Y. H. Jiang *et al.*, EUV-photon-induced multiple ionization and fragmentation dynamics: from atoms to molecules. *J. Phys. B At. Mol. Opt. Phys.* **42**, 134012 (2009).
166. R. Moshammer *et al.*, Few-Photon Multiple Ionization of Ne and Ar by Strong Free-Electron-Laser Pulses. *Phys. Rev. Lett.* **98**, 203001 (2007).
167. Z.-S. Yuan *et al.*, Inner-shell excitations of krypton 3d investigated by electron impact with high resolution. *Phys. Rev. A*. **71**, 64701 (2005).